Title
Ray-based Finite Element Method for High-frequency Helmholtz Equations

Author
Fang, Jun

Publication Date
2017

UNIVERSITY OF CALIFORNIA,
IRVINE

Ray-based Finite Element Method for High-frequency Helmholtz Equations

DISSERTATION

submitted in partial satisfaction of the requirements
for the degree of

DOCTOR OF PHILOSOPHY

in Mathematics

by

Jun Fang

Dissertation Committee:
Professor Hongkai Zhao, Chair
Professor Long Chen
Professor Jack Xin

2017

TABLE OF CONTENTS

LIST OF FIGURES

LIST OF TABLES

LIST OF ALGORITHMS

ACKNOWLEDGMENTS

I would like to thank my advisor, Professor Hongkai Zhao, for his advice, support, patience and giving me extensive freedom to explore every interesting things, including both academic research and life beyond school.

I would like to extend my sincere thanks and appreciation to Professor Long Chen for his enlightening advice on my research and courses, and Dr. Leonardo Zepeda-Núñez for his inspirational suggestions on my research projects.

I would like to acknowledge the rest of my thesis and advancement committee, Professor Jack Xin, Professor Yifeng Yu and Professor Babak Shahbaba. I really appreciate their time, insight and expertise.

Thanks to my family and my friends. Without your support, I would not be able to complete my PhD study. I love you.

CURRICULUM VITAE

Jun Fang

EDUCATION

Doctor of Philosophy in Mathematics **2017**
University of California, Irvine *Irvine, California*

Bachelor of Science in Mathematics **2012**
Zhejiang University *Hangzhou, Zhejiang*

ABSTRACT OF THE DISSERTATION

Ray-based Finite Element Method for High-frequency Helmholtz Equations

By

Jun Fang

Doctor of Philosophy in Mathematics

University of California, Irvine, 2017

Professor Hongkai Zhao, Chair

In this dissertation we propose a ray-based finite element method (ray-FEM) for the high-frequency Helmholtz equation in smooth media, whose basis are learned adaptively from the medium and source. The method requires a fixed number of grid points per wavelength to represent the wave field; moreover, it achieves an asymptotic convergence rate of $\mathcal{O}(\omega^{-\frac{1}{2}})$, where ω is the frequency parameter in the Helmholtz equation.

The local basis are motivated by the geometric optics ansatz and are composed of polynomials modulated by plane waves propagating in a few dominant ray directions. The ray directions are learned by processing a low-frequency wave field that probes the medium with the same source. Once the local ray directions are extracted, they are incorporated into the local basis to solve the high-frequency Helmholtz equation. This process can be continued to further improve the approximations for both local ray directions and high-frequency wave fields iteratively.

In addition, a fast sweeping-type preconditioner is used to solve the resulting linear system. We present numerical examples in 2D to show both efficiency and convergence of our method as the frequency becomes larger and larger. In particular, we show empirically that the overall complexity is $\mathcal{O}(\omega^2)$ up to a poly-logarithmic factor.

Chapter 1

Introduction

1.1 The Helmholtz equation

The numerical solution of time-harmonic wave propagation in heterogeneous media is of paramount importance in a variety of applications such as medical imaging, oil exploration, nondestructive testing, noise reduction, radar and sonar technology.

In the constant density acoustic approximation the time harmonic wave propagation is modeled by the Helmholtz equation, which is given by

$$\mathcal{H}u := -\Delta u(\mathbf{x}) - \frac{\omega^2}{c^2(\mathbf{x})} u(\mathbf{x}) = f(\mathbf{x}), \quad \mathbf{x} \in \Omega \subseteq \mathbb{R}^d, \tag{1.1}$$

plus absorbing or radiation boundary conditions, where, d is the dimension, ω is the frequency, $c(\mathbf{x}) > 0$ is the wave speed, $m(\mathbf{x}) = 1/c^2(\mathbf{x})$ is the squared slowness, and $f(\mathbf{x})$ is the source term, which we suppose to be compactly supported. The main intentions of this thesis are the study and development of efficient numerical methods to compute the unknown wave field u.

1.2 Computational challenges

The numerical solution of the Helmholtz equation (1.1) in the high-frequency regime, i.e., $\omega \gg 1$, is notoriously hard to compute. Following the Nyquist-Shannon sampling criterion [108], it is sufficient to represent a wave field oscillating at frequency ω using $\mathcal{O}(\omega^d)$ degrees of freedom (DOFs) with a mesh size $h = \mathcal{O}(\omega^{-1})$. Recent work [34] showed that these degrees of freedom are also intrinsic for the solution of the Helmholtz equation in general. Hence it implies that the optimal complexity to solve (1.1) is $\mathcal{O}(\omega^d)$, up to possible poly-log factors. In general, an overall complexity of optimal order is difficult to achieve due to two typical challenges:

- how to design a discretization that can achieve both accuracy and stability without oversampling; and
- how to solve the resulting linear system in linear complexity, up to poly-log factors, as the frequency becomes large.

Methods used to discretize the Helmholtz equation can be broadly categorized depending on the level of adaptivity that they exploit. We refer to adaptive discretizations as discretizations that depend on the medium and the source.

Examples of non-adaptive discretization are: standard finite differences [73, 92], standard continuous or discontinuous finite elements [41, 60, 61, 98, 116], and spectral methods [94, 118, 119], among many others. They are very general in the sense that they can be used for a variety of different problems. However, in the case of the Helmholtz equation they yield either pollution-error[1], inducing oversampled sparse discretizations [6, 8] whose associated linear systems can be solved in optimal complexity [32, 33, 109, 123, 129], or quasi-optimal

---

[1] The ratio between numerical error and best approximation error from a discrete finite element space is ω dependent.

sparse discretizations whose associated linear systems are prohibitively expensive to solve [52, 119] in the high-frequency regime[2].

Adaptive methods, on the other hand, aim to leverage *à priori* knowledge of the solution of the Helmholtz equation, such as its known oscillatory behavior. In practice, adaptive methods have mostly focused on adaptivity to the medium, such as polynomial Galerkin methods with *hp* refinement [5, 85, 88, 114, 126, 132], specially optimized finite differences [26, 53, 110, 111, 120] and finite elements [6, 117], enriched finite elements [37, 38, 39, 40], plane wave methods [7, 23, 50, 51, 54, 84, 89], generalized plane wave methods [62, 63], locally corrected finite elements [19, 46, 97], and discretizations with specially chosen basis functions [9, 10, 91], among many others. They have been especially successful on reducing the pollution effect by accurately capturing the dispersion relation. However, in the high-frequency regime, they are either not asymptotically quasi-optimal for heterogeneous media or they yield linear systems that cannot be solved in quasi-linear time with current algorithms[3].

New advances on adaptive discretizations [16, 49, 57, 93] seem to indicate that quasi-optimality of the discretization, while still yielding linear systems amenable to fast solvers, can be achieved if the discretization depends on the *medium* and the *source* simultaneously. These fully adaptive discretizations aim to leverage analytical knowledge about the solution, such as asymptotic expansions, which in the case of the solution of the Helmholtz equation can take the form of the geometric optics ansatz:

$$u(\mathbf{x}) \approx \text{superposition of } \{A_n(\mathbf{x}) e^{i\omega\phi_n(\mathbf{x})}\}_{n=1}^{N}, \tag{1.2}$$

---

[2] Recent advances such as [94, 118], have lowered the complexity of global spectral methods; however, they still have a super-linear cost.

[3] Some of the discretizations mentioned above, in particular plane wave type Trefftz methods with wave directions in equi-spaced distribution [55], usually yield extremely ill-conditioned systems due to loss of numerical orthogonality in the basis. In general, the resulting linear system need to be solved using pivoted QR factorization in super-linear time.

in which the phases $\phi_n(\mathbf{x})$ and amplitudes $A_n(\mathbf{x})$ depend on the medium, domain boundary, and source, but they are independent of the frequency.

Indeed, phased-based methods [49, 57, 93] are instances of fully adaptive discretizations. These methods use (1.2) to build an approximation space by modulating a polynomial basis with an oscillatory component using the phase functions, which need to be computed beforehand.

However, computing the appropriate global phase functions $\phi_n(\mathbf{x})$ in the whole domain is a challenging task for a general medium with varying speed; different phase functions may be defined in different regions, whose boundaries are difficult to determine *à priori*; the error on the solution is proportional to the approximation error of the phase function times ω^4, implying that the phase functions need to be computed extremely accurately, thus, making the computation of the phase functions the bottleneck in such approaches.

In the present thesis, we propose a ray-based finite element method (ray-FEM) based on the geometric optics ansatz, in which the phase functions are not explicitly computed, thus bypassing the bottleneck. The method relies on a linear approximation of the phase functions in the form

$$\phi_n(\mathbf{x}) \approx \phi_n(\mathbf{x}_0) + \nabla\phi_n(\mathbf{x}_0)\cdot(\mathbf{x}-\mathbf{x}_0) = \phi_n(\mathbf{x}_0) + |\nabla\phi_n(\mathbf{x}_0)|\widehat{\mathbf{d}}_n(\mathbf{x}_0)\cdot(\mathbf{x}-\mathbf{x}_0); \tag{1.3}$$

where $\widehat{\mathbf{d}}_n(\mathbf{x}_0) := \frac{\nabla\phi_n(\mathbf{x})}{|\nabla\phi_n(\mathbf{x})|}$ are called the ray directions [14] or the dominant wave directions [16]. The dominant wave directions are extracted from a low-frequency probing wave field, namely, a solution to a low frequency problem, i.e., the Helmholtz equation with the same medium and source, but at a much lower frequency $\widetilde{\omega} = \mathcal{O}(\omega^{1/2})$.

The underpinning property used in this approach is that the phase functions are indepen-

---

[4] If we suppose that the approximation error of computing ϕ_n is $\delta\phi_n$, then the approximation error of the solution is given by $|e^{i\omega\phi_n} - e^{i\omega(\phi_n+\delta\phi_n)}| \sim \omega\delta\phi_n$, which is ω dependent.

dent of the frequency, and the extraction of their gradient is a stable operation using signal processing algorithms, such as Numerical Micro Local Analysis (NMLA) [12, 13, 14]. The resulting linear system is sparse and it can be solved efficiently using state of the art preconditioners such as [32, 33, 109, 123, 129].

The ray-FEM can efficiently compute wave fields when the source is far away, even in the presence of caustics. However, it cannot handle the singularities at point sources for two reasons:

- the traditional geometrical-optics amplitude at the source is singular, which indicates that the geometric optics ansatz breaks down at the source points and it is difficult to handle for a finite element based method;
- the phase is also singular, i.e., the curvature of the circular wave front goes to infinity at the source point, which makes the ray direction extraction, such as NMLA, infeasible.

One often used approach is to mollify the Dirac delta using a Gaussian, and then use a graded mesh; however, this would make the linear system source dependent requiring extensive remeshing, which can be prohibitively expensive.

On the other hand, the Babich's expansion [3], which is a Hankel-based asymptotic expansion, can capture source singularity and overcome the above difficulties near the source in heterogeneous media. The ingredients of the expansion can be numerically computed by high-order Eulerian asymptotic methods [103] to yield accurate solutions in the neighborhood of the point source.

1.3 Results

The main result of this paper is a method to solve the Helmholtz equation in the high-frequency regime with an optimal asymptotic cost $\mathcal{O}(\omega^d)$, up to poly-log factors, with respect to the number of intrinsic degrees of freedom.

The performance of the algorithms owes to the following two ideas:

- we build a fully adaptive discretization based on the geometric optics ansatz and local linear approximation of the phase functions whose gradients are learned from a low-frequency problem solved using standard finite elements; the resulting discretization is stable and asymptotically accurate, in particualr, the error converges to zero as $\mathcal{O}(\omega^{-\frac{1}{2}})$, as the frequency increases;
- we solve the resulting linear system using state of the art preconditioners with linear complexity, up to poly-logarithmic factors;

The adaptive discretization is built by learning the dominant wave directions specific to the medium and source distribution. In particular, we probe the same medium using the same source, i.e., solving a low-frequency Helmholtz equation

$$-\Delta\widetilde{u}(\mathbf{x}) - \frac{\widetilde{\omega}^2}{c^2(\mathbf{x})}\widetilde{u}(\mathbf{x}) = f(\mathbf{x}), \quad \mathbf{x} \in \Omega \subseteq \mathbb{R}^d, \tag{1.4}$$

plus suitable boundary (or radiation) conditions with the same $c(\mathbf{x})$, $f(\mathbf{x})$ and a relative low frequency $\widetilde{\omega}$. The computed wave field is post-processed by NMLA or other signal processing tools to locally estimate the dominant wave directions; both the number of dominant wave directions and the directions can vary from point to point, thus, providing the flexibility to deal with general media. The estimated wave directions are then used to enrich a finite element space, which is used to discretize the original high-frequency Helmholtz equation.

In particular, we develop a simple ray-based finite element (ray-FEM) method in 2D for smooth media as a proof of concept study of our proposed approach. We start with a finite element mesh with mesh-size h satisfying $wh = \mathcal{O}(1)$, i.e., a few points per wavelength. First, the low frequency is chosen by $\widetilde{\omega} \sim \sqrt{\omega}$ such that the equation (1.4) is solved quasi-optimality on such mesh since $\widetilde{\omega}^2 h = \mathcal{O}(1)$ [86]. Then NMLA [12, 13, 14] (see chapter 3) is applied to the computed low-frequency wave field to estimate the local dominant wave directions.

The estimated dominant wave directions are then used to enrich the local finite element basis following (1.2) in order to discretize the high-frequency Helmholtz equation on the same mesh.

For the cases with source singularities, we develop a simple and natural hybrid approach to combine the asymptotic method and the ray-FEM to take advantage of the strengths of both methods for the high frequency Helmholtz equation. In particular, we utilize the Babich's expansion and high-order numerical methods to compute the wave field near the source, and couple with the ray-FEM to compute the far field waves in smooth media.

In addition, we develop an efficient preconditioner to solve the resulting linear system iteratively using GMRES [106]. The preconditioner is based on the method of polarized traces [129]. Numerical experiments show that it is possible to solve the linear system in $\mathcal{O}(N)$ complexity with a possible poly-logarithmic factor for a smooth medium, where N is the total number of unknowns.

Moreover, once a more accurate wave field is computed, it can be used to get a better estimation of the dominant wave directions, which can be used to improve the high-frequency wave field iteratively. If necessary, the solution for the high-frequency Helmholtz equation can also be processed by NMLA to improve the estimation of local dominant wave directions which can be used to further improve the high-frequency solution.

1.4 Related work

In this section we briefly review related approaches to solve the Helmholtz equation, and we compare some of them with the approach proposed in this thesis.

As stated in the prequel, it is difficult to design a sparse discretization that can achieve both accuracy and stability under the condition $\omega h = \mathcal{O}(1)$ as ω becomes large. This is mainly due to the pollution effect in error estimates for finite element methods [6, 8], i.e., the ratio between numerical error and best approximation error from a discrete finite element space is ω dependent.

From a physical point of view, the wave-field governed by the Helmholtz equation contains waves propagating in all directions and satisfying a specific dispersion relation. As a consequence, numerical errors due to dispersion or interpolation for these propagating modes will propagate as physical waves to pollute the whole computed wave field. In particular, a compact stencil on a mesh that is comparable to the wavelength cannot approximate the dispersion relations for propagating waves in all direction uniformly well as $\omega \to \infty$ [8].

In order to minimize (or eliminate, if possible) the pollution effect, various approaches have been proposed lately in the literature. Approaches based on polynomial basis coupled with non-standard variational formulations (such as [90]) have been proposed in order to approximate the Helmholtz operator so that the resulting discrete problems have better stability properties. For example, with an appropriate choice of coefficients, low-order compact finite-difference discretizations can effectively reduce the dispersion error [42, 67, 95]. Another instances of such approaches are the generalized finite-element method (GFEM) [6] and continuous interior penalty finite element method (CIP-FEM) [126, 132], the interpolated optimized finite difference method (IOFD) [111, 112], Galerkin methods with *hp* refinement [85, 87, 88], among many others. These methods successfully reduce the pollution error; however, they require either a more restrictive condition on the mesh size or the degree of the polynomial approximation to be ω dependent, resulting on a large increase in the size and interconnectivity of the associated linear systems as the frequency increases.

On the other hand, many approaches rely on specially designed basis in order to accurately represent the solution. One of such approaches is the multiscale Petrov-Galerkin method [19, 46, 97]; the method relies on local corrections, which are numerically computed in a fine mesh, to the basis functions. This method is stable and quasi-optimal under the minimal resolution condition $\omega H = \mathcal{O}(1)$ and $m = \mathcal{O}(\log \omega)$ for the coarse mesh H and an oversampling parameter m. However, the condition on the fine mesh size, h, to solve the local subscale correction is the same as the standard FEM. It requires $\omega^{3/2} h = \mathcal{O}(1)$ for stability [126] and $\omega^2 h = \mathcal{O}(1)$ for quasi-optimality [86].

Other instances of such approaches are methods that incorporate appropriate oscillatory behavior into the basis of Galerkin methods. The key issue for this strategy is how to design the oscillatory basis. Since the Helmholtz solutions locally behave like plane waves, one approach is to incorporate plane waves with a predetermined equi-spaced distribution in directions into the basis. For example, products of plane waves with local finite elements basis are used in the generalized finite element methods (GFEM) [86], partition of unity finite element methods (PUFEM) [7], virtual element methods (VEM) [96], discontinuous Galerkin methods (DG) [44, 50, 54] and ultra weak variational formulation (UWVF) [20, 22, 23]. Trefftz-type methods [55] use local solutions of the Helmholtz equation as the basis functions, which in the case of piece-wise constant media are plane waves.

It is well known that these plane wave based methods need fewer DOFs to achieve better accuracy than the conventional finite-element methods [55, 74]. A comparison of these methods can be found in [45, 47, 59, 74]. However, these methods have two caveats: they normally perform poorly when the source is not zero, and it is not clear how to choose the number of plane wave directions *à priori*. In order to achieve a good accuracy, a fine, ω dependent [55], resolution in the angle space is required. This refinement in the angle space will not only increase the DOFs significantly but also make the resulting linear system extremely ill-conditioned due to the numerical coherence of the elements of the basis.

Other basis functions can be utilized, such as Bessel functions [57, 81, 82] to improve the adaptivity to the curvature of the solution's wavefront and also reduce the linear dependence of the basis. Moreover, generalized plane waves [62, 63, 64] in the form $e^{P(\mathbf{x})}$ with an appropriate complex polynomial $P(\mathbf{x})$ are developed to achieve high-order convergence for smooth heterogeneous media. Another instance of methods using other basis functions is the discontinuous enrichment method (DEM) [38, 39, 40, 115], which combines Lagrange multipliers on the mesh interfaces to enforce continuity of the solution with approximation spaces composed by sums of continuous polynomials and discontinuous plane waves, leading to a reduction of the number of DOFs.

A more adaptive approach to solve the high-frequency Helmholtz equation is based on the geometric optics ansatz of the wave field (1.2). In the ansatz, phases and amplitudes are independent of frequency and hence are non-oscillatory and smooth except at a measure zero set, e.g., focus points, caustics, corners in a smooth medium. Once the phase functions of the wave fronts are available, the oscillatory pattern of the wave field is known, phase-based numerical methods [16, 49, 57, 93] explicitly incorporate these known phases into the basis functions to significantly improve both stability and accuracy.

As discussed in the prequel, computing the global phase functions for general media is a challenging task. Meanwhile, a phase function can be locally approximated by a linear function with a leading term $\widehat{\mathbf{d}}_n(\mathbf{x}_0)\cdot\mathbf{x}$, where $\widehat{\mathbf{d}}_n(\mathbf{x}_0)$ is the local dominant wave direction and can be extracted stably by signal processing algorithms. With pre-computed dominant wave directions by ray tracing [17, 18, 24, 57], the dominant plane wave method [16] incorporates them into the local basis to combine the advantages of phase-based methods and plane wave methods. Since only the dominant directions of wave fronts relevant to the problem are involved in this approach, the number of degrees of freedom can be kept minimal, and ill-conditioning of the resulting linear system due to redundancy can be reduced.

Finally, under the stronger assumption that the medium can be written as a homogeneous background plus a compactly supported perturbation, the Helmholtz equation can be converted to a second-kind integral equation by introducing the Green's function corresponding to the background, resulting in the so-called Lippmann-Schwinger equation. Recent advances have shown that it is possible to solve the Lippmann-Schwinger equation, and hence the Helmholtz equation, in optimal time [130]. In this thesis, however, we treat a more general case.

Chapter 2

The Ray-FEM Method

We describe the ray-FEM method for the Helmholtz equation and its rationale in this chapter. We explain briefly the geometric optic ansatz and how it is approximated locally via a superposition of plane waves propagating in a set of dominant directions. We then proceed to explain how these plane waves are incorporated into the finite element basis to improve both stability and accuracy of the numerical solution to the high-frequency Helmholtz equation.

In this chapter we suppose that the dominant directions are known exactly. In chapter 3 we will describe how to learn the dominant wave directions by probing the medium using low-frequency waves.

We use the following boundary value problem in 2D to illustrate our method,

$$\begin{cases} -\Delta u - k^2(\mathbf{x})u = f, \quad \text{in} \quad \Omega, \\ \frac{\partial u}{\partial n} + i\beta k(\mathbf{x})u = g, \quad \text{on} \quad \partial\Omega, \end{cases} \tag{2.1}$$

where Ω is an open bounded Lipschitz domain in $\mathbb{R}^2$, $k(\mathbf{x}) = \omega/c(\mathbf{x})$ is the inhomogeneous wave number, $f \in L^2(\Omega)$ is the source and $g \in L^2(\partial\Omega)$ is the boundary data. Moreover, we suppose that both source and boundary data are frequency independent. Equation (2.1) is usually refered to as the Helmholtz equation with impedance boundary conditions (IBC). This equation was chosen in order to easily impose other types of boundary conditions by modifying the coefficient β. Specifically, the Dirichlet boundary condition corresponds to $\beta = \infty$ and the first order absorbing boundary condition to $\beta = \pm 1$. Moreover, it is easy to extend (2.1) to incorporate absorbing boundary conditions implemented via PML [15], as it will be introduced in section 4.1 and performed in the numerical experiments in chapter 7.

2.1 Geometric optics ansatz

The standard derivation of the geometric optics ansatz uses WKJB approximation [65, 70, 105] (or the Lüneberg-Kline expansion [71]) for the solution to the Helmholtz equation (1.1):

$$u(\mathbf{x}) \sim e^{i\omega\phi(\mathbf{x})} \sum_{\ell=0}^{\infty} \frac{A_\ell(\mathbf{x})}{\omega^\ell}. \tag{2.2}$$

By taking $\omega \to \infty$ and considering only the first term one has

$$u(\mathbf{x}) = A(\mathbf{x}) e^{i\omega\phi(\mathbf{x})} + \mathcal{O}\left(\frac{1}{\omega}\right), \tag{2.3}$$

where A is usually called the amplitude and ϕ the phase. The key features of the geometric optics ansatz are:

- A and ϕ are *independent* of the frequency ω;
- A and ϕ *depend* on the medium, $c(\mathbf{x})$, and the source distribution, $f(\mathbf{x})$.

Moreover, except for a small set of points, e.g., source/focus points, caustics, and discontinuities of the medium, A and ϕ are smooth functions satisfying the following PDE system for $f = \mathcal{O}(\omega^0)$,

$$\text{(eikonal)} \quad |\nabla\phi| = \frac{1}{c}, \qquad \text{(transport)} \quad 2\nabla\phi\cdot\nabla A + A\Delta\phi = 0. \tag{2.4}$$

As long as the medium is smooth and no caustic occurs, the asymptotic expansion (2.2) holds in the sense that the difference between the exact solution of the Helmholtz equation and an N-term truncation of the expansion (2.2) can be made arbitrarily *smooth* for all $\mathbf{x}$ provided N is taken sufficiently large. This has been justified in [72] for oscillatory initial value problems of hyperbolic equations and further made rigorous in the theory of Fourier integral operators [56]. In practice, the one-term asymptotic expansion (2.3), namely, the so-called geometrical-optics term, usually yields sufficiently accurate asymptotic solutions [2, 4, 69, 75, 77, 100, 104].

The coefficients $\{A_l\}$ in the asymptotic expansion (2.2) satisfy a recursive system of transport equations [2, 4, 104] which are coupled with the eikonal equation. Under the assumption that the medium is smooth and no caustic occurs, one may solve the transport equations to estimate the coefficients $\{A_l\}$ in different formulations [2, 4, 75]. Since the geometrical-optics term is oscillatory when $\omega \neq 0$, it should be understood in the L^2 sense rather than the L^∞ sense.

Assuming that the medium is smooth and no caustic occurs, the asymptotic expansion (2.3) will not fail as long as the frequency parameter ω is not zero, but the resulting difference between the asymptotic expansion (2.3) and the exact solution may be large in the L^2 norm as the frequency approaches zero [104]. Given an inhomogeneous medium, however, it is hard to pin down how large ω should be so that the asymptotic expansion (2.3) is accurate up to a certain specified accuracy, as this is closely related to both fluctuations and correlation lengths of the normalized propagation speed of the medium [125] and the frequency parameter ω. We refer the reader to [31] for further details on the geometric optics ansatz.

2.2 Local plane wave approximation

In general, the phase function, ϕ, and the amplitude function, A, are multi-valued functions corresponding to multiple arrivals of wave fronts [11]. Hence one can further decompose the geometric optics ansatz into a superposition of several wave fronts in the form:

$$u(\mathbf{x}) = \text{superposition of } \{A_n(\mathbf{x})e^{i\omega\phi_n(\mathbf{x})}\}_{n=1}^{N(\mathbf{x})} + \mathcal{O}\left(\frac{1}{\omega}\right), \tag{2.5}$$

where $N(\mathbf{x})$ is the number of fronts/rays passing through $\mathbf{x}$, and the phases ϕ_n and amplitudes A_n are single valued functions satisfying the eikonal/transport equations (2.4), each defined in a suitable domain with suitable boundary conditions [11].

Based on the above geometric optics ansatz, one can derive a local plane wave approximation at any point where ϕ_n and A_n are smooth with variations on a $\mathcal{O}(1)$ scale. Indeed, using Taylor expansions on a small neighborhood around an observation point $\mathbf{x}_0$ for the n-th wave front, we have,

$$u(\mathbf{x}) = (A_n(\mathbf{x}_0)+\nabla A_n(\mathbf{x}_0)(\mathbf{x}-\mathbf{x}_0))\, e^{i\omega(\phi_n(\mathbf{x}_0)+\nabla\phi(\mathbf{x}_0)\cdot(\mathbf{x}-\mathbf{x}_0))}+\mathcal{O}\left(h^2+\omega h^2+\frac{1}{\omega}\right), \tag{2.6}$$

for $|\mathbf{x}-\mathbf{x}_0| < h \ll 1$.

Define

$$\widehat{\mathbf{d}}_n := \frac{\nabla\phi_n(\mathbf{x}_0)}{|\nabla\phi_n(\mathbf{x}_0)|} = c(\mathbf{x}_0)\nabla\phi_n(\mathbf{x}_0) \tag{2.7}$$

as the ray directions of the wave fronts at $\mathbf{x}_0$, $k(\mathbf{x}_0) = \omega/c(\mathbf{x}_0)$, and

$$B_n(\mathbf{x}) = (A_n(\mathbf{x}_0) + \nabla A_n(\mathbf{x}_0)(\mathbf{x} - \mathbf{x}_0))e^{i\omega(\phi_n(\mathbf{x}_0) - \nabla\phi(\mathbf{x}_0)\cdot\mathbf{x}_0)} \tag{2.8}$$

the affine complex amplitude. By replacing (2.7) and (2.8) in (2.6) we have

$$u(\mathbf{x}) = B_n(\mathbf{x})e^{ik(\mathbf{x}_0)\widehat{\mathbf{d}}_n\cdot\mathbf{x}} + \mathcal{O}\left(h^2 + \omega h^2 + \frac{1}{\omega}\right), \tag{2.9}$$

for $|\mathbf{x} - \mathbf{x}_0| < h \ll 1$.

From (2.5) and (2.9) we have that u can be approximated locally by a superposition of plane waves propagating in certain directions with affine complex amplitudes. Moreover, as $\omega \to \infty$, such that $\omega h = \mathcal{O}(1)$, the asymptotic error for the local plane wave approximation (2.9) is $\mathcal{O}(\omega^{-1})$, which is of the same order as the asymptotic error for the original geometric-optics ansatz (2.5). We use (2.9) as the motivation to construct local finite element basis with mesh size $h = \mathcal{O}(\omega^{-1})$, in which an affine function is multiplied by plane waves oscillating in those ray directions, resulting in local approximations similar to (2.9).

2.3 Ray-based FEM formulation

We use a finite element method to compute the solution to (2.1), whose standard weak formulation is given by

$$\text{Find } u \in H^1(\Omega), \text{ such that } \mathcal{B}(u,v) = \mathcal{F}(v), \quad \forall v \in H^1(\Omega), \tag{2.10}$$

where

$$\mathcal{B}(u,v) := \int_\Omega \nabla u \cdot \nabla \overline{v} dV - \int_\Omega k^2 u\overline{v} dV + i\beta \oint_{\partial\Omega} k u \overline{v} dS, \tag{2.11}$$

$$\mathcal{F}(v) := \int_{\Omega} f\overline{v}dV + \oint_{\partial\Omega} g\overline{v}dS. \tag{2.12}$$

The domain, Ω, is discretized with a standard regular triangulated mesh, with mesh-size h. The resulting mesh is denoted by $\mathcal{T}_h = \{K\}$, where K represents a triangle of the mesh. Using the aforementioned mesh we define two approximation spaces for the variational formulation (2.10):

- the standard FEM (S-FEM), where we use low-order $\mathbb{P}1$ finite elements, i.e., piece-wise bilinear functions;
- the ray-FEM, where we use $\mathbb{P}1$ finite elements multiplied by plane waves as in (2.9).

For a given element $K \in \mathcal{T}_h$, we denote by V_j and $\mathbf{x}_j, j = 1, 2, 3$, the vertices of K and their coordinates, respectively. Moreover, we denote by $\{\varphi_j(\mathbf{x})\}_{j=1}^3$ a partition of unity consisting of piecewise bilinear functions satisfying $\varphi_j(\mathbf{x}_i) = \delta_{ij}$, $i, j = 1, 2, 3$, where δ_{ij} is the Kronecker delta. The basis given by $\{\varphi_j(\mathbf{x})\}_{j=1}^3$ is usually called the nodal basis for Lagrange $\mathbb{P}1$ finite elements. The standard local approximation space is given by

$$V_S(K) = \text{span}\{\varphi_j(\mathbf{x}), j = 1, 2, 3\}, \tag{2.13}$$

and the global $\mathbb{P}1$ finite element space

$$V_S(\mathcal{T}_h) = \{v \in C^0(\overline{\Omega}) : v|_K \in V_S(K), \forall K \in \mathcal{T}_h\}. \tag{2.14}$$

To define the ray-FEM we enrich the $\mathbb{P}1$ finite elements by incorporating the ray information. Letting $\{\widehat{\mathbf{d}}_{j,l}\}_{l=1}^{n_j}$ be n_j ray directions at the vertex V_j, we define the ray-based local approximation space by

$$V_{Ray}(K) = \text{span}\{\varphi_j(\mathbf{x})e^{ik_j\widehat{\mathbf{d}}_{j,l}\cdot\mathbf{x}}, \quad k_j = k(\mathbf{x}_j), \quad j = 1,2,3, \quad l = 1,...,n_j\},$$

and the global ray-FEM space by

$$V_{Ray}(\mathcal{T}_h) = \{v \in C^0(\overline{\Omega}) : v|_K \in V_{Ray}(K), \forall K \in \mathcal{T}_h\}.$$

We can define the standard FEM method by

$$\text{Find } u \in V_S(\mathcal{T}_h), \text{ such that } \mathcal{B}(u,v) = \mathcal{F}(v), \quad \forall v \in V_S(\mathcal{T}_h). \tag{2.15}$$

Analogously, we define the ray-FEM method by

$$\text{Find } u \in V_{Ray}(\mathcal{T}_h), \text{ such that } \mathcal{B}(u,v) = \mathcal{F}(v), \quad \forall v \in V_{Ray}(\mathcal{T}_h). \tag{2.16}$$

2.4 Approximation property of ray-FEM with exact ray information

We provide a simple computation to estimate the approximation error of the ray-FEM space. In particular, we compute an asymptotic bound on $\inf_{u_h \in V_{Ray}(\mathcal{T}_h)} ||u - u_h||_{L^2(\Omega)}$, where u is the solution to the Helmholtz equation (1.1). We achieve the bound by estimating the interpolating error using $V_{Ray}(K)$ as a basis.

In the computation we assume that the ray direction, which is the gradient of the phase function ϕ, and the phase function itself, are exactly known. For simplicity, we assume $N = 1$ for the asymptotic formula in (2.5), i.e., only one ray crosses each point of the domain thus no caustic occur. Similar results can be derived for the multiple-ray crossing case: $N > 1$. In addition we suppose that f, the source, is zero inside the domain; otherwise, singularities in the amplitude may appear. Under those circumstances A and ϕ are smooth. From the geometric optics ansatz, we have

$$u(\mathbf{x}) = A(\mathbf{x}) e^{i\omega\phi(\mathbf{x})} + \mathcal{O}\left(\omega^{-1}\right). \tag{2.17}$$

We denote by N_h the total number of vertices on the mesh $\mathcal{T}_h$, by $\{\mathbf{x}_j\}_{j=1}^{N_h}$ the coordinates of all mesh nodes, and by $\{\varphi_j(\mathbf{x})\}_{j=1}^{N_h}$ their corresponding nodal basis functions for the standard $\mathbb{P}1$ element.

We note that $e^{i\omega[\phi(\mathbf{x}_j) - \nabla\phi(\mathbf{x}_j)\cdot\mathbf{x}_j]}$ is a constant for the nodal basis associated to $\mathbf{x}_j$ in an element K. From this observation we can easily deduce that the local ray-FEM space can be rewritten as

$$\begin{aligned} V_{Ray}(K) &= \mathrm{span}\{\varphi_j(\mathbf{x}) e^{ik_j\mathbf{d}_j\cdot\mathbf{x}}\} = \mathrm{span}\{\varphi_j(\mathbf{x}) e^{i\omega\nabla\phi(\mathbf{x}_j)\cdot\mathbf{x}}\}, \\ &= \mathrm{span}\{\varphi_j(\mathbf{x}) e^{i\omega\nabla\phi(\mathbf{x}_j)\cdot\mathbf{x}} e^{i\omega[\phi(\mathbf{x}_j) - \nabla\phi(\mathbf{x}_j)\cdot\mathbf{x}_j]}\}, \\ &= \mathrm{span}\{\varphi_j(\mathbf{x}) e^{i\omega[\phi(\mathbf{x}_j) + \nabla\phi(\mathbf{x}_j)\cdot(\mathbf{x}-\mathbf{x}_j)]}\}. \end{aligned}$$

Hence the nodal interpolation of the solution can be written as

$$u_I := \sum_{j=1}^{N_h} A(\mathbf{x}_j)\varphi_j(\mathbf{x}) e^{i\omega[\phi(\mathbf{x}_j) + \nabla\phi(\mathbf{x}_j)\cdot(\mathbf{x}-\mathbf{x}_j)]}, \tag{2.18}$$

which, by construction lies within the global ray-FEM space $V_{Ray}(\mathcal{T}_h)$.

Let S_j be the support of $\varphi_j(\mathbf{x})$, and $|S_j| \sim \mathcal{O}(h^2)$ be the area of S_j. Then using the triangular inequality and the smoothness assumptions we have

$$\begin{aligned}
\|u-u_I\|_{L^2(\Omega)} &\leq \|A(\mathbf{x})e^{i\omega\phi(\mathbf{x})}-\textstyle\sum_{j=1}^{N_h}A(\mathbf{x}_j)\varphi_j(\mathbf{x})e^{i\omega\phi(\mathbf{x})}\|_{L^2(\Omega)}\\
&\quad +\|\textstyle\sum_{j=1}^{N_h}A(\mathbf{x}_j)\varphi_j(\mathbf{x})\left(e^{i\omega\phi(\mathbf{x})}-e^{i\omega[\phi(\mathbf{x}_j)+\nabla\phi(\mathbf{x}_j)\cdot(\mathbf{x}-\mathbf{x}_j)]}\right)\|_{L^2(\Omega)}+\mathcal{O}(\omega^{-1})\\
&\leq \|A(\mathbf{x})-\textstyle\sum_{j=1}^{N_h}A(\mathbf{x}_j)\varphi_j(\mathbf{x})\|_{L^2(\Omega)}\\
&\quad +\textstyle\sum_{j=1}^{N_h}\|A\|_{L^\infty(\Omega)}\|e^{i\omega\phi(\mathbf{x})}-e^{i\omega[\phi(\mathbf{x}_j)+\nabla\phi(\mathbf{x}_j)\cdot(\mathbf{x}-\mathbf{x}_j)]}\|_{L^2(S_j)}+\mathcal{O}(\omega^{-1})\\
&\lesssim h^2|A|_{H^2(\Omega)}+\textstyle\sum_{j=1}^{N_h}\|A\|_{L^\infty(\Omega)}\omega h^2\|\nabla^2\phi\|_{L^\infty(\Omega)}|S_j|+\mathcal{O}(\omega^{-1})\\
&\lesssim h^2|A|_{H^2(\Omega)}+\omega h^2\|A\|_{L^\infty(\Omega)}\|\nabla^2\phi\|_{L^\infty(\Omega)}+\mathcal{O}(\omega^{-1}).
\end{aligned}$$

To be more precise, $h^2|A|_{H^2(\Omega)}$ comes from the interpolation error estimate [113], and $\omega h^2\|A\|_{L^\infty(\Omega)}\|\nabla^2\phi\|_{L^\infty(\Omega)}$ comes from the Taylor expansion of $\phi(\mathbf{x})$ near $\mathbf{x}_j$, where the constant for $\lesssim$ is a generic positive constant only depending on the domain Ω. This implies that

$$\inf_{u_h\in V_{Ray}(\mathcal{T}_h)}||u-u_h||_{L^2(\Omega)}\lesssim h^2|A|_{H^2(\Omega)}+\omega h^2\|A\|_{L^\infty(\Omega)}\|\nabla^2\phi\|_{L^\infty(\Omega)}+\mathcal{O}(\omega^{-1}). \tag{2.19}$$

Or, asymptotically,

$$\inf_{u_h\in V_{Ray}(\mathcal{T}_h)}||u-u_h||_{L^2(\Omega)}=\mathcal{O}(h^2+\omega h^2+\omega^{-1}). \tag{2.20}$$

Moreover, if the exact rays are known and the mesh size follows $h\sim\omega^{-1}$, then we have

$$\inf_{u_h\in V_{Ray}(\mathcal{T}_h)}||u-u_h||_{L^2(\Omega)}=\mathcal{O}(\omega^{-1}), \tag{2.21}$$

i.e. that the approximation error decays linearly with $\frac{1}{\omega}$, without oversampling.

Remark 1. *The ray information can be incorporated into other Galerkin basis in the same fashion. For example, in the hybrid numerical asymptotic method of [49], the basis functions* *are constructed by multiplying nodal piece-wise bilinear functions to oscillating functions with phase factors; the plane wave DG method of [16] employs the products of small degree polynomials and dominant plane waves as basis functions; the phase-based hybridizable DG method of [93] considers basis functions as products of polynomials and phase-based oscillating functions. Moreover, the phase or ray information in these methods is obtained from solving the eikonal equation with ray tracing and related techniques.*

Chapter 3

Learning Local Dominant Ray Directions

In chapter 2 we use geometric optics to provide the motivation for the ray-FEM by building an adaptive approximation space that incorporates ray information specific to the underlying Helmholtz equation. However, the ray directions, which depend on the medium and source distribution, are unknown quantities themselves, hence they need to be computed or estimated. One way is to compute the global phase function, by either ray tracing or solving the eikonal equation, and take its gradient. As discussed in the introduction, computing the global phase function in a general varying medium can be extremely difficult.

Here we propose a totally different approach. This novel approach is based on learning the dominant ray directions by probing the same medium with the same source but using a relative low-frequency wave. To be more specific, we first solve the Helmholtz equation (1.4) with the same speed function $c(\mathbf{x})$, right hand side $f(\mathbf{x})$ and boundary conditions but with a relative low-frequency $\widetilde{\omega} \sim \sqrt{\omega}$ on a mesh with size $h = \mathcal{O}(\widetilde{\omega}^{-2}) = \mathcal{O}(\omega^{-1})$ with a standard finite element method, which is quasi-optimal in that regime. Then the local dominant ray directions are estimated based on the computed low-frequency wave field. The key point is that the low-frequency wave has probed the medium specific to the problem globally while only local dominant ray directions need to be learned, which allows us to handle multiple arrivals of wave fronts locally. In particular, we use numerical micro-local analysis (NMLA), which is simple, stable and robust, to extract the dominant ray directions locally. However, this is a signal processing task that can be accomplished using other methods such as Prony's method [21], Pisarenko's method [99], MUSIC [107], matrix pencil [58], wavefront tracking methods [122], among many others. The main advantage of NMLA is that it was explicitly designed for capturing the dominant directions, in particular, NMLA was designed to be more robust to perturbations of the underlying model.

3.1 NMLA

Now we provide a brief introduction to NMLA developed in [13, 14]. If we suppose that a wave-field is locally a weighted superposition of plane waves having the same wave number and propagating in different directions. Then the aim of NMLA is to extract the directions and the weights by sampling and processing the wave field locally. In the sequel we use a 2D example to illustrate the method, which can be easily extended to 3D cases [14].

Suppose that a wave field, denoted by $u(\mathbf{x})$, is composed of N plane waves around an observation point $\mathbf{x}_0$,

$$u(\mathbf{x}) = \sum_{n=1}^{N} B_n e^{ik(\mathbf{x}-\mathbf{x}_0)\cdot\widehat{\mathbf{d}}_n}, \quad |\widehat{\mathbf{d}}_n| = 1. \tag{3.1}$$

We suppose that we can sample the wave field, $u(\mathbf{x})$, and its derivative on a circle $S_r(\mathbf{x}_0)$ centered at $\mathbf{x}_0$ with radius r. The wave field can be written under the model assumption in

(3.1) as

$$u(\mathbf{x}_0 + r\widehat{\mathbf{s}}) = \sum_{n=1}^{N} B_n e^{i\alpha\widehat{\mathbf{s}}\cdot\widehat{\mathbf{d}}_n}, \quad \alpha = kr,\ \widehat{\mathbf{s}} \in \mathbb{S}^1. \tag{3.2}$$

Furthermore, we define the angle variables $\theta = \theta(\widehat{\mathbf{s}})$ and $\theta_n = \theta(\widehat{\mathbf{d}}_n)$ such that $\widehat{s} = (\cos\theta, \sin\theta)$, $\widehat{\mathbf{d}}_n = (\cos\theta_n, \sin\theta_n)$, and $\mathbf{x}(\theta) = \mathbf{x}_0 + r\widehat{\mathbf{s}}(\theta)$. Using the angle based notation we sample the impedance quantity on the circle $S_r(\mathbf{x}_0)$,

$$U(\theta) := \frac{1}{ik}\partial_r u(\mathbf{x}(\theta)) + u(\mathbf{x}(\theta)), \tag{3.3}$$

which removes any possible ambiguity due to resonance [13] and improves the robustness to noise for solutions to the Helmholtz equation. Then we apply the filtering operator $\mathcal{B}$ to the impedance quantity

$$\mathcal{B}U(\theta) := \frac{1}{2L_\alpha + 1} \sum_{l=-L_\alpha}^{L_\alpha} \frac{(\mathcal{F}U)_l e^{il\theta}}{(-i)^l (J_l(\alpha) - iJ_l'(\alpha))}, \tag{3.4}$$

where $L_\alpha = \max(1, [\alpha], [\alpha + (\alpha)^{\frac{1}{3}} - 2.5])$, J_l is the Bessel function of order l, J_l' is its derivative and

$$(\mathcal{F}U)_l := \frac{1}{2\pi} \int_0^{2\pi} U(\theta) e^{-il\theta} d\theta \tag{3.5}$$

is the l-th Fourier coefficient of U. It is shown in [13] that

$$\mathcal{B}U(\theta) = \sum_{n=1}^{N} B_n S_{L_\alpha}(\theta - \theta_n), \tag{3.6}$$

where $S_L(\theta) = \frac{\sin([2L+1]\theta/2)}{[2L+1]\sin(\theta/2)}$. As a consequence, we have that if $\alpha = kr \to \infty$ then

$$\lim_{\alpha\to\infty} \mathcal{B}U(\theta) = \begin{cases} B_n, & \text{if } \theta = \theta_n \text{ (or } \widehat{\mathbf{s}} = \widehat{\mathbf{d}}_n \text{);} \\ 0, & \text{otherwise.} \end{cases} \tag{3.7}$$

Then it is possible to obtain the directions and the amplitudes by picking the peaks in the filtered data in (3.6); see details in Algorithm 1 and 2.

Algorithm 1 NMLA

```
function $\mathbf{d}_\omega = \text{NMLA}(\mathbf{x}_0, \mathcal{T}_h, \omega, h, c, \mathbf{u})$
    choose $r \sim \omega^{-\frac{1}{2}}$                                  ▷ Radius for the sampling circle
    choose $M \sim \omega r$                                         ▷ Number of sampling points
    $\Delta\theta = 2\pi/M$,                                          ▷ Angular discretization
    for $\theta = 0 : \Delta\theta : 2\pi$ do
        $\mathbf{x}(\theta) = \mathbf{x}_0 + r\widehat{\mathbf{s}}(\theta)$
        $U(\theta) = \frac{\omega}{ic(\mathbf{x}_0)}\partial_r u(\mathbf{x}(\theta)) + u(\mathbf{x}(\theta))$    ▷ Sample impedance data
        $F(\theta) = \mathcal{B}U(\theta)$                                   ▷ Apply the filter (3.4)
    end for
    $\boldsymbol{\theta} = [0 : \Delta\theta : 2\pi]$, $\boldsymbol{F} = F(\boldsymbol{\theta})$
    $\boldsymbol{\theta}_{est} = FindPeaks(\boldsymbol{\theta}, \boldsymbol{F})$
    $\mathbf{d}_\omega = \mathbf{d}(\boldsymbol{\theta}_{est})$
end function
```

Algorithm 2 FindPeaks

```
function $\boldsymbol{\theta}_{est} = \textsc{FindPeaks}(\boldsymbol{\theta}, \boldsymbol{F})$
    $\mathbf{dF} = \mathbf{F}[2 : \text{end}] - \mathbf{F}[1 : \text{end} - 1]$    ▷ Approximate the differentiation
    $\mathbf{s} = sign(\mathbf{dF})$    ▷ Take the sign
    $\mathbf{ds} = \mathbf{s}[2 : \text{end}] - \mathbf{s}[1 : \text{end} - 1]$
    $\mathbf{idx} = 1 + find(\mathbf{ds} < 0)$    ▷ Find the index of local maxima
    $\boldsymbol{\theta}_{est} = \boldsymbol{\theta}[\mathbf{idx}]$
end function
```

3.2 Stability and error analysis for NMLA

However, for applications, the measured data are never a perfect superposition of plane waves; therefore, we provide, for completeness, stability and error estimates for NMLA from [13] in this section. For simplicity we use the single wave case, i.e., $N = 1$. Moreover, we assume that the measured datum is a perturbation to the perfect plane wave datum of the form $U(\theta) = U^{plane}(\theta) + \delta U(\theta)$, where U^{plane} denotes a single plane wave datum in the form of (3.2). Let θ^* denote the angle for which $\theta \mapsto \mathcal{B}U(\theta)$ is maximum. Assuming that the noise level satisfies

$$||\delta U||_{L^\infty} < \frac{1}{4B^*}|B_1|, \tag{3.8}$$

where $B^* \leq 1$ is a pure constant independent of ω and B_1 is the complex amplitude of the plane wave. Then the error in the angle estimation is given by

$$|\theta_1 - \theta^*| \leq \frac{2\pi}{2L_\alpha + 1} \sim \mathcal{O}(\frac{1}{\alpha}), \quad \alpha = kr \sim \infty. \tag{3.9}$$

Similar results can be derived for multiple waves $N > 1$. We remark that $\frac{1}{4B^*} \geq 0.25$, which implies that for a single wave, as long as the perturbation is relatively small with respect to the true plane wave signal, say the relative noise level do not surpass 25%, the estimation error is $\mathcal{O}(\frac{1}{kr})$. In other words, the larger the radius of the circle compared to wavelength the more accurate the estimation is.

In Benamou's work [13], an analysis of a point source shows that $|\theta_1 - \theta^*|$ decreases like $\mathcal{O}(\omega^{-1/2})$ when the point $\mathbf{x}_0$ is far away from the source and the radius of the observation circle is chosen like $r \sim \omega^{-1/2}$ for large ω. We obtain similar accuracy order for general noisy plane waves under some smoothness conditions; see details in section 3.3.

3.3 Error analysis of wave field as a perturbed plane wave datum

As displayed above, provided that the perturbation of the signal is relatively small compared to the signal, the estimation of the plane wave directions converges and the error is $\mathcal{O}(\frac{1}{\omega r})$. In this thesis, we use NMLA to process a wave-field datum, which is the numerical solution to the Helmholtz equation, to extract the directions of dominant wave fronts based on the geometric optics ansatz (2.5) in the high-frequency regime. Hence it is important to study the wave field data as a perturbation of plane wave data locally and estimate the error in the ray directions obtained from NMLA. In particular, this analysis allows us to find the optimal choice of the radius of the sampling circle/sphere, in order to achieve the minimal asymptotic error for the ray direction estimation in terms of the frequency ω of the Helmholtz equation which generates the wave-field datum. The result is crucial for both error analysis and implementation of the ray-FEM. Since the wave field datum in our application is the numerical solution to the Helmholtz equation, its perturbation is composed of the sum of three components:

1. numerical errors in solving the Helmholtz equation and interpolation errors in obtaining data on the sampling circle/sphere for NMLA from the numerical solution on a fixed mesh;
2. asymptotic errors in the geometric optics ansatz;
3. local approximation errors of a smooth curved wave front by a planar wave front.

On a mesh with mesh size $h = \mathcal{O}(\omega^{-1})$, the last component, which we call the phase error, is the dominant factor among the three. We present below an analysis of the phase error, in which, for simplicity, we only consider one wave front.

Consider a single wave front, $u(\mathbf{x}) = A(\mathbf{x})e^{i\omega\phi(\mathbf{x})}$. Following the notation used throughout the paper, we assume the reference point to be $\mathbf{x}_0$, and the small sampling circle around $\mathbf{x}_0$ to be $\{\mathbf{x}|\mathbf{x}-\mathbf{x}_0 = r\widehat{\mathbf{s}}\}$, $\nabla\phi(\mathbf{x}_0) = \eta_0\widehat{\mathbf{d}}_0$, where $r \ll 1, |\widehat{\mathbf{s}}| = 1$, $\eta_0 = 1/c(\mathbf{x}_0)$, $|\widehat{\mathbf{d}}_0| = 1$. We have by the Taylor expansion,

$$\begin{aligned} A(\mathbf{x}) &= A(\mathbf{x}_0) + \nabla A(\mathbf{x}_0)\cdot(\mathbf{x}-\mathbf{x}_0) + \mathcal{O}\left((\mathbf{x}-\mathbf{x}_0)^2\right) = A(\mathbf{x}_0) + r\left(\nabla A(\mathbf{x}_0)\cdot\widehat{\mathbf{s}}\right) + \mathcal{O}\left(r^2\right), \\ \phi(\mathbf{x}) &= \phi(\mathbf{x}_0) + \nabla\phi(\mathbf{x}_0)\cdot(\mathbf{x}-\mathbf{x}_0) + \tfrac{1}{2}\left(\mathbf{x}-\mathbf{x}_0\right)^T\nabla^2\phi(\mathbf{x}_0)\left(\mathbf{x}-\mathbf{x}_0\right) + \mathcal{O}\left((\mathbf{x}-\mathbf{x}_0)^3\right) \\ &= \phi(\mathbf{x}_0) + r\eta_0\left(\widehat{\mathbf{d}}_0\cdot\widehat{\mathbf{s}}\right) + \tfrac{1}{2}r^2\left(\widehat{\mathbf{s}}^T\nabla^2\phi(\mathbf{x}_0)\widehat{\mathbf{s}}\right) + \mathcal{O}\left(r^3\right). \end{aligned}$$

Denoting $\phi_0(\mathbf{x}) = \phi(\mathbf{x}_0) + \nabla\phi(\mathbf{x}_0)\cdot(\mathbf{x}-\mathbf{x}_0)$, $u_0(\mathbf{x}) = A(\mathbf{x}_0)e^{i\omega\phi_0(\mathbf{x})}$, we have

$$\begin{aligned} \delta u(\mathbf{x}) &= u(\mathbf{x}) - u_0(\mathbf{x}) \\ &= A(\mathbf{x})e^{i\omega\phi(\mathbf{x})} - A(\mathbf{x}_0)e^{i\omega\phi_0(\mathbf{x})} \\ &= \left[A(\mathbf{x}_0)e^{i\omega\phi(\mathbf{x})} + r\left(\nabla A(\mathbf{x}_0)\cdot\widehat{\mathbf{s}}\right)e^{i\omega\phi(\mathbf{x})} + \mathcal{O}\left(r^2\right)\right] - A(\mathbf{x}_0)e^{i\omega\phi_0(\mathbf{x})} \\ &= A(\mathbf{x}_0)e^{i\omega\phi_0(\mathbf{x})}\left(e^{i\omega\left[\frac{1}{2}r^2\left(\widehat{\mathbf{s}}^T\nabla^2\phi(\mathbf{x}_0)\widehat{\mathbf{s}}\right)+\mathcal{O}\left(r^3\right)\right]} - 1\right) + r\left(\nabla A(\mathbf{x}_0)\cdot\widehat{\mathbf{s}}\right)e^{i\omega\phi(\mathbf{x})} + \mathcal{O}\left(r^2\right), \end{aligned}$$

$$
\begin{aligned}
\tfrac{\partial}{\partial r}\left(\delta u(\mathbf{x})\right) &= \tfrac{\partial}{\partial r}\left(A(\mathbf{x})e^{i\omega\phi(\mathbf{x})} - A(\mathbf{x}_0)e^{i\omega\phi_0(\mathbf{x})}\right) \\
&= \left(\nabla A(\mathbf{x}_0)\cdot\widehat{\mathbf{s}} + \mathcal{O}(r)\right)e^{i\omega\phi(\mathbf{x})} + A(\mathbf{x})e^{i\omega\phi(\mathbf{x})}i\omega\left[\eta_0(\widehat{\mathbf{d}}_0\cdot\widehat{\mathbf{s}}) + r\left(\widehat{\mathbf{s}}^T\nabla^2\phi(\mathbf{x}_0)\widehat{\mathbf{s}}\right) + \mathcal{O}(r^2)\right] \\
&\quad -A(\mathbf{x}_0)e^{i\omega\phi_0(\mathbf{x}_0)}i\omega\eta_0(\widehat{\mathbf{d}}_0\cdot\widehat{\mathbf{s}}) \\
&= \left(\nabla A(\mathbf{x}_0)\cdot\widehat{\mathbf{s}} + \mathcal{O}(r)\right)e^{i\omega\phi(\mathbf{x})} + A(\mathbf{x})e^{i\omega\phi(\mathbf{x})}i\omega\left[r\left(\widehat{\mathbf{s}}^T\nabla^2\phi(\mathbf{x}_0)\widehat{\mathbf{s}}\right) + \mathcal{O}(r^2)\right] \\
&\quad + \left(A(\mathbf{x})e^{i\omega\phi(\mathbf{x})} - A(\mathbf{x}_0)e^{i\omega\phi_0(\mathbf{x}_0)}\right)i\omega\eta_0(\widehat{\mathbf{d}}_0\cdot\widehat{\mathbf{s}}) \\
&= \left(\nabla A(\mathbf{x}_0)\cdot\widehat{\mathbf{s}} + \mathcal{O}(r)\right)e^{i\omega\phi(\mathbf{x})} + A(\mathbf{x})e^{i\omega\phi(\mathbf{x})}i\omega\left[r\left(\widehat{\mathbf{s}}^T\nabla^2\phi(\mathbf{x}_0)\widehat{\mathbf{s}}\right) + \mathcal{O}(r^2)\right] \\
&\quad +i\omega\eta_0(\widehat{\mathbf{d}}_0\cdot\widehat{\mathbf{s}})\delta u(\mathbf{x}).
\end{aligned}
$$

Then

$$
\begin{aligned}
\delta U(\mathbf{x}) &= \left(\tfrac{1}{i\omega\eta_0}\tfrac{\partial}{\partial r} + 1\right)\delta u(\mathbf{x}) \\
&= \tfrac{1}{i\omega\eta_0}\left(\nabla A(\mathbf{x}_0)\cdot\widehat{\mathbf{s}} + \mathcal{O}(r)\right)e^{i\omega\phi(\mathbf{x})} + \tfrac{1}{\eta_0}A(\mathbf{x})e^{i\omega\phi(\mathbf{x})}\left[r\left(\widehat{\mathbf{s}}^T\nabla^2\phi(\mathbf{x}_0)\widehat{\mathbf{s}}\right) + \mathcal{O}(r^2)\right] \\
&\quad +(\widehat{\mathbf{d}}_0\cdot\mathbf{s})\delta u(\mathbf{x}) + \delta u(\mathbf{x}) \\
&= \tfrac{1}{i\omega\eta_0}\left(\nabla A(\mathbf{x}_0)\cdot\widehat{\mathbf{s}} + \mathcal{O}(r)\right)e^{i\omega\phi(\mathbf{x})} + \tfrac{1}{\eta_0}A(\mathbf{x})e^{i\omega\phi(\mathbf{x})}\left[r\left(\widehat{\mathbf{s}}^T\nabla^2\phi(\mathbf{x}_0)\widehat{\mathbf{s}}\right) + \mathcal{O}(r^2)\right] \\
&\quad +(\widehat{\mathbf{d}}_0\cdot\widehat{\mathbf{s}} + 1)\left\{A(\mathbf{x}_0)e^{i\omega\phi_0(\mathbf{x})}\left(e^{i\omega\left[\frac{1}{2}r^2\left(\widehat{\mathbf{s}}^T\nabla^2\phi(\mathbf{x}_0)\widehat{\mathbf{s}}\right)+\mathcal{O}\left(r^3\right)\right]} - 1\right)\right. \\
&\quad \left. +r\left(\nabla A(\mathbf{x}_0)\cdot\widehat{\mathbf{s}}\right)e^{i\omega\phi(\mathbf{x})} + \mathcal{O}\left(r^2\right)\right\}.
\end{aligned}
$$

Hence

$$
\begin{aligned}
|\delta U(\mathbf{x})| &= \left|\left(\tfrac{1}{i\omega\eta_0}\tfrac{\partial}{\partial r} + 1\right)\delta u(\mathbf{x})\right| \\
&\le \tfrac{|\nabla A(\mathbf{x}_0)| + \mathcal{O}(r)}{\omega\eta_0} + \tfrac{|A(\mathbf{x})|}{\eta_0}\left(r\left|\widehat{\mathbf{s}}^T\nabla^2\phi(\mathbf{x}_0)\widehat{\mathbf{s}}\right| + \mathcal{O}(r^2)\right) \\
&\quad +2|A(\mathbf{x}_0)|\omega\left(\tfrac{1}{2}r^2\left|\widehat{\mathbf{s}}^T\nabla^2\phi(\mathbf{x}_0)\widehat{\mathbf{s}}\right| + \mathcal{O}(r^3)\right) + 2r|\nabla A(\mathbf{x}_0)| + \mathcal{O}(r^2) \qquad (3.10) \\
&= \left(\tfrac{1}{\omega\eta_0} + 2r\right)|\nabla A(\mathbf{x}_0)| + \left(\tfrac{|A(\mathbf{x})|r}{\eta_0} + |A(\mathbf{x}_0)|\omega r^2\right)\left|\widehat{\mathbf{s}}^T\nabla^2\phi(\mathbf{x}_0)\widehat{\mathbf{s}}\right| \\
&\quad +\tfrac{|A(\mathbf{x})|}{\eta_0}\mathcal{O}(r^2) + 2\omega|A(\mathbf{x}_0)|\mathcal{O}(r^3) + \mathcal{O}(r^2).
\end{aligned}
$$

As shown in section 3.2, on one hand δU has to be small compared to U. On the other hand, the error in direction estimate from NMLA is $\mathcal{O}(\frac{1}{wr})$. Assuming the smoothness of $A(\mathbf{x})$ and $\phi(\mathbf{x})$, i.e., boundedness of $\nabla A(\mathbf{x})$, $A(\mathbf{x})$ and $\nabla^2\phi(\mathbf{x})$, the leading term in δU is $\omega r^2 |A(\mathbf{x}_0)| \left|\widehat{\mathbf{s}}^T \nabla^2\phi(\mathbf{x}_0)\widehat{\mathbf{s}}\right|$ as $\omega \to \infty$, where $\widehat{\mathbf{s}}^T \nabla^2\phi(\mathbf{x}_0)\widehat{\mathbf{s}}$ is the curvature of the wave front. Hence the radius of the sampling circle can at most be chosen $r \sim \mathcal{O}(\frac{1}{\sqrt{\omega}})$ as $\omega \to \infty$. Let

$$r = \tfrac{C_\epsilon}{\sqrt{\omega}}, \qquad |\nabla A(\mathbf{x})| \le C_1, \qquad |A(\mathbf{x})| \le C_2, \qquad \left|\mathbf{s}^T \nabla^2\phi(\mathbf{x})\mathbf{s}\right| \le C_3, \tag{3.11}$$

Then

$$|\delta U(\mathbf{x})| \;\; \le 2C_\epsilon^2 C_3 \, |A(\mathbf{x}_0)| + \mathcal{O}\left(\tfrac{1}{\sqrt{\omega}}\right) \tag{3.12}$$

By choosing C_ϵ such that $2C_\epsilon^2 C_3 \le \frac{1}{4}$, the perturbation $\delta U(\mathbf{x})$ satisfies the condition 3.8 for ω large enough, which implies that the error in the ray direction estimate by NMLA is $\mathcal{O}(\omega^{-\frac{1}{2}})$.

Remark 2. *The above analysis also shows that NMLA can not be used to estimate ray directions within a few wavelengths away from the point source since the curvature of the wave front there is of order* $\mathcal{O}(w)$.

3.4 Second order curvature correction for a point source

Section 3.3 shows that the angle estimation property (3.9) does not yield the same accuracy order $\mathcal{O}(\omega^{-1})$ as the geometric optics ansatz for a general wave front such as waves near a point source. We also know that the curvature term after linearization is responsible for this loss of accuracy. Roughly speaking, the estimation is in $\mathcal{O}(\omega^{-1})$ for a plane wave and $\mathcal{O}(\omega^{-1/2})$ for a point-source wave. The second-order curvature correction in [13] shows that it is possible to identify the curvature to improve the angle estimation. A summary of the correction process is provided in this section.

We consider a normalized point-source solution in a homogeneous medium

$$u(\mathbf{x}) = \sqrt{k}\frac{i}{4}H_0^{(1)}(k|\mathbf{x}-\mathbf{x}_1|).$$

When the radius r of the sampling circle is smaller than the distance from the observation point $\mathbf{x}_0$ to the source point $\mathbf{x}_1$, that is, $r < |\mathbf{x}_1 - \mathbf{x}_0|$, we use the Graff Addition Theorem [27, page 66] on the sampling circle, then we have

$$u(\mathbf{x}_0 + r\widehat{s}) = \sqrt{k}\frac{i}{4}\sum_{l=-\infty}^{+\infty} H_l^{(1)}(kR_1)e^{il(\theta-\theta_1)}$$

where $R_1 := |\mathbf{x}_1 - \mathbf{x}_0|$ is the reciprocal of the curvature of the wave front at point $\mathbf{x}_0$, and θ and θ_1 are the angles such that $\widehat{s} = (\cos\theta, \sin\theta)$, $\frac{\mathbf{x}_1-\mathbf{x}_0}{|\mathbf{x}_1-\mathbf{x}_0|} = (\cos\theta_1, \sin\theta_1)$.

The impedance quantity is

$$\begin{aligned} U^{point}(\theta) &= (\tfrac{1}{ik}\partial_r + 1)u(\mathbf{x}_0 + r\widehat{s}) \\ &= \tfrac{e^{ikR_1}}{\sqrt{-i8\pi R_1}}\textstyle\sum_{l=-\infty}^{+\infty} C_l(kR_1)(-i)^l(J_l(kr) - iJ_l'(kr))e^{il(\theta-\theta_1)}, \end{aligned}$$

where

$$C_l(kR_1) = i^l\sqrt{\frac{ik\pi R_1}{2}}e^{-ikR_1}H_l^{(1)}(kR_1).$$

By applying the filter operator $\mathcal{B}$ defined in (3.4) we get

$$\mathcal{B}U^{point}(\theta) = \frac{b_1}{2L_{kr}+1}\sum_{-L_{kr}}^{L_{kr}} C_l(kR_1)e^{il(\theta-\theta_1)}, \text{ with } b_1 = \frac{e^{ikR_1}}{\sqrt{-i8\pi R_1}}. \tag{3.13}$$

Then we can get the first estimate of the true angle θ_1 by using Algorithm 2 on $\mathcal{B}U^{point}(\theta)$, which is denoted by θ_{est}. Meanwhile, we have an analytical formula for the Fourier coefficient $\widehat{\beta_l}$ of $\mathcal{B}U^{point}(\theta)$, which is

$$\widehat{\beta_l} = \frac{b_1}{2L_{kr}+1} C_l(kR_1) e^{-il\theta_1}. \tag{3.14}$$

We shift the phase,

$$\widehat{\beta_l} e^{il\theta_{est}} = \frac{b_1}{2L_{kr}+1} C_l(kR_1) e^{-il(\theta_{est}-\theta_1)} = \frac{b_1}{2L_{kr}+1} C_l(kR_1) e^{-il\delta\theta},$$

where $\delta\theta := \theta_{est} - \theta_1$ is the error that we make on the angle estimation.

It is important to notice that when kR_1 is large enough $C_l(kR_1)$ is a perturbation of 1 due to the asymptotic expansion [124, page 198],

$$C_l(kR_1) \sim 1 + \sum_{m=1}^{\infty} \frac{(l,m)}{(-2ikR_1)^m}, \text{ with}(l,m) = \frac{(4l^2-1^2)(4l^2-3^2)...(4l^2-(2m-1)^2)}{2^{2m}m!} \tag{3.15}$$

Now we use the first two terms of the expression

$$C_l(kR_1) = \frac{e^{i\frac{l^2-\frac{1}{4}}{2kR_1}}}{(1-\frac{l^2-\frac{1}{4}}{(kR_1)^2})^{\frac{1}{4}}} + \mathcal{O}(\frac{1}{(kR_1)^3}),$$

and obtain

$$\widehat{\beta_l} e^{il\theta_{est}} = \frac{b_1}{2L_{kr}+1} e^{i\frac{l^2-\frac{1}{4}}{2kR_1}} \frac{1}{(1-\frac{l^2-\frac{1}{4}}{(kR_1)^2})^{\frac{1}{4}}} + \mathcal{O}(\frac{1}{(kR_1)^3}).$$

We then consider

$$\psi_l := \mathcal{I}\left(\log(\widehat{\beta_l} e^{il\theta_{est}}) - \log(\widehat{\beta_0})\right) = l\delta\theta + \frac{l^2}{2kR_1} + \mathcal{O}(\frac{1}{(kR_1)^3}). \tag{3.16}$$

where $\mathcal{I}$ stands for the imaginary part.

We see that ψ_l is close to a parabolic function of the mode number l so that it can be fitted by a least-squares approximation. The estimated parabola coefficient $\delta\theta_{est}$ then provides a correction on the angle, which we call it the second order curvature correction. It improves the accuracy of angle estimation to a great extent. We remind that this process is only valid for a single point source in a smooth medium. Below is a summary of the NMLA curvature correction algorithm.

Algorithm 3 NMLA Curvature Correction

```
function $d_\omega$ = NMLA-CORRECTION($\mathbf{x}_0, \mathcal{T}_h, \omega, h, c, \mathbf{u}$)
    choose $r \sim \omega^{-\frac{1}{2}}$, $M \sim \omega r$, $\Delta\theta = 2\pi/M$
    $\alpha = \omega r / c(\mathbf{x}_0)$, $L = \max(1, [\alpha], [\alpha + (\alpha)^{\frac{1}{3}} - 2.5])$
    for $\theta = 0 : \Delta\theta : 2\pi$ do
        $\mathbf{x}(\theta) = \mathbf{x}_0 + r\widehat{\mathbf{s}}(\theta)$
        $U(\theta) = \frac{\omega}{ic(\mathbf{x}_0)} \partial_r u(\mathbf{x}(\theta)) + u(\mathbf{x}(\theta))$, $F(\theta) = \mathcal{B}U(\theta)$
    end for
    $\boldsymbol{\theta} = [0 : \Delta\theta : 2\pi]$, $\boldsymbol{F} = F(\boldsymbol{\theta})$
    $\theta_{est} = FindPeaks(\boldsymbol{\theta}, \boldsymbol{F})$        ▷ Get the first angle estimation
    for $l = -L : L$ do
        $\widehat{\beta}_l = (\mathcal{F}(\mathbf{F}))_l$        ▷ Compute the Fourier coefficients (3.14)
        $\psi_l = Imag(\log(\frac{\widehat{\beta}_l}{\widehat{\beta}_0} e^{il\theta_{est}}))$        ▷ Compute the imaginary part (3.16)
    end for
    $\delta\theta = LeastSquare([\psi_l]_{l=-L:L})$        ▷ Estimate the coefficient of linear term (3.16)
    $\theta_{cor} = \theta_{est} - \delta\theta$, $d_\omega = d(\theta_{cor})$        ▷ Correct the angle
end function
```

3.5 Approximation property of numerical ray-FEM

In this section we incorporate the errors from the estimation of the ray directions into the approximation error for the ray-FEM method, in which ray directions are first estimated by applying Algorithm 1 to the solution of the Helmholtz equation with a relatively low frequency. The estimated ray directions are then used to generate the approximation space. With the same assumptions as in section 2.4, we estimate an upper bound on

$$\inf_{u_h \in V_{Ray}^h(\mathcal{T}_h)} \|u - u_h\|_{L^2(\Omega)}, \tag{3.17}$$

when the ray-FEM space, $V_{Ray}^h(\mathcal{T}_h)$, is constructed using the estimated ray directions from high-frequency waves by NMLA.

From section 3.3, the error estimation of dominant ray directions is $\mathcal{O}(\omega^{-1/2})$. The numerical ray-FEM space $V_{Ray}^h(\mathcal{T}_h)$ is defined similar to $V_{Ray}(\mathcal{T}_h)$ with the exact ray directions $\{\widehat{\mathbf{d}}_j\}$ replaced by the ones $\{\widehat{\mathbf{d}}_j^h\}$ estimated by NMLA and $|\widehat{\mathbf{d}}_j - \widehat{\mathbf{d}}_j^h| \sim \mathcal{O}(\omega^{-1/2})$.

We denote by

$$u_I^h = \sum_{j=1}^{N_h} A(\mathbf{x}_j)\varphi_j(\mathbf{x}) e^{i\omega[\phi(\mathbf{x}_j) + 1/c(\mathbf{x}_j)\widehat{\mathbf{d}}_j^h \cdot (\mathbf{x} - \mathbf{x}_j)]} \tag{3.18}$$

the nodal interpolation of the solution in $V_{Ray}^h(\mathcal{T}_h)$ analogous to the definition of u_I in (2.18). Then we have

$$\begin{aligned}
\|u_I - u_I^h\|_{L^2(\Omega)} &= \|\textstyle\sum_{j=1}^{N_h} A(\mathbf{x}_j)\varphi_j(\mathbf{x}) e^{i\omega\phi(\mathbf{x}_j)}\big(e^{i\omega\nabla\phi(\mathbf{x}_j)\cdot(\mathbf{x}-\mathbf{x}_j)} - e^{i\omega/c(\mathbf{x}_j)\widehat{\mathbf{d}}_j^h\cdot(\mathbf{x}-\mathbf{x}_j)}\big)\|_{L^2(\Omega)} \\
&\leq \textstyle\sum_{j=1}^{N_h} \|A\|_{L^\infty(\Omega)} \|e^{i\omega/c(\mathbf{x}_j)\widehat{\mathbf{d}}_j\cdot(\mathbf{x}-\mathbf{x}_j)} - e^{i\omega/c(\mathbf{x}_j)\widehat{\mathbf{d}}_j^h\cdot(\mathbf{x}-\mathbf{x}_j)}\|_{L^2(S_j)} \\
&\lesssim \textstyle\sum_{j=1}^{N_h} \|A\|_{L^\infty(\Omega)} \omega h \|c^{-1}\|_{L^\infty(\Omega)} |\widehat{\mathbf{d}}_j - \widehat{\mathbf{d}}_j^h| |S_j| \\
&\lesssim \omega^{1/2} h \|A\|_{L^\infty(\Omega)} \|c^{-1}\|_{L^\infty(\Omega)}.
\end{aligned}$$

Hence,

$$
\begin{aligned}
\inf_{u_h \in V^h_{Ray}(\mathcal{T}_h)} \|u - u_h\|_{L^2(\Omega)} &\le \|u - u^h_I\|_{L^2(\Omega)} \le \|u - u_I\|_{L^2(\Omega)} + \|u_I - u^h_I\|_{L^2(\Omega)} \\
&\lesssim h^2 |A|_{H^2(\Omega)} + \omega h^2 \|A\|_{L^\infty(\Omega)} \|\nabla^2 \phi\|_{L^\infty(\Omega)} \qquad (3.19)\\
&\quad + \omega^{1/2} h \|A\|_{L^\infty(\Omega)} \|c^{-1}\|_{L^\infty(\Omega)} + \mathcal{O}(\omega^{-1}).
\end{aligned}
$$

Under the same smoothness assumption as in section 2.4, the constant for $\lesssim$ only depends on the domain, and more compactly, we have that

$$
\inf_{u_h \in V^h_{Ray}(\mathcal{T}_h)} \|u - u_h\|_{L^2(\Omega)} = \mathcal{O}(h^2 + \omega h^2 + \omega^{1/2} h + \omega^{-1}). \tag{3.20}
$$

Comparing with (2.20) and (3.20), the error in the estimation of dominant ray directions due to NMLA leads to the extra term $\omega^{1/2} h$, which is the leading order in the high-frequency regime. Specifically, if $\omega h = \mathcal{O}(1)$, then we have

$$
\inf_{u_h \in V^h_{Ray}(\mathcal{T}_h)} \|u - u_h\|_{L^2(\Omega)} = \mathcal{O}(\omega^{-1/2}). \tag{3.21}
$$

We point out that the desirable convergence rate in this case is $\mathcal{O}(\omega^{-1})$, which has the same order as the geometric optics ansatz. However, as analyzed in section 3.3, for a general wave field, the optimal achievable asymptotic error of the estimation of the dominant wave directions using NMLA is $\mathcal{O}(\omega^{-1/2})$. This is indeed the bottleneck to improve the convergence order. In particular, the leading term of the approximation error for the numerical ray-FEM comes from $\|u_I - u^h_I\|_{L^2(\Omega)}$, which is $\omega h |\widehat{\mathbf{d}}_j - \widehat{\mathbf{d}}^h_j| \sim |\widehat{\mathbf{d}}_j - \widehat{\mathbf{d}}^h_j| \sim \omega^{-1/2}$ if $\omega h = \mathcal{O}(1)$. Still, we can obtain a higher order approximation for some special cases. For example, we can use second order curvature correction version of NMLA for single point source in homogeneous media to improve the ray estimation to $\mathcal{O}(\omega^{-1})$, meaning that we can obtain the optimal convergence order in this special case.

Chapter 4

Singularity

By building local basis composed of polynomials modulated by plane waves propagating in a few dominant ray directions, the ray-FEM only requires a fixed number of grid points per wavelength to achieve both accuracy and stability without oversampling; moreover, a fast solver is developed in chapter 5 for solving the resulting linear system with linear complexity up to poly-log factors. As explained in the introduction, the ray-FEM can efficiently compute wave fields when the source is far away, but it cannot handle the singularities at point sources.

Here, we introduce the Babich's expansion [3], which is a Hankel-based asymptotic expansion, to capture source singularity and overcome the above difficulties near the source in heterogeneous media. The ingredients of the expansion can be numerically computed by high-order Eulerian asymptotic methods [103] to yield accurate solutions in the neighborhood of the point source. The reasons that we prefer to use the Babich's ansatz rather than the usual geometrical-optics ansatz are well illustrated in [103] and are briefly summarized here. If we apply the usual asymptotic expansion of the solution for the Helmholtz equation of a point source in an inhomogeneous medium, then we end up with the following systems:

$$u(\mathbf{r},\mathbf{r}_0) = e^{i\omega\tau} \sum_{s=0}^{\infty} A_s(\mathbf{r},\mathbf{r}_0) \frac{1}{(i\omega)^{s-\frac{(d-1)}{2}}}, \tag{4.1}$$

where $\tau = \tau(\mathbf{r},\mathbf{r}_0)$ is the phase satisfying the eikonal equation

$$\nabla\tau \cdot \nabla\tau = m^2(\mathbf{r}), \quad \tau(\mathbf{r}_0,\mathbf{r}_0) = 0, \tag{4.2}$$

and $A_s = A_s(\mathbf{r},\mathbf{r}_0)$ satisfy a recursive system of transport equations along rays,

$$2\nabla\tau \cdot \nabla A_s + A_s \Delta\tau = -\Delta A_{s-1}, \quad s = 0,\ 1,\ \cdots,\ \ A_{-1} \equiv 0. \tag{4.3}$$

However, a difficulty arises immediately: how to initialize A_s at the source point for this system of equations. Moreover, when d is even, the ray series (4.1) does not yield a uniform asymptotic form close to the source. When $d = 3$ Avila and Keller [2] were able to find the initial data for A_s by using the boundary layer method, but the case of $d = 2$ was left incomplete. In practice, such difficulties in initializing amplitudes were handled in ad hoc ways in the sense that the amplitudes were initialized a little bit away from the point source by using amplitudes for the medium with a constant refractive index corresponding to that of the source point [76, 79, 80, 102, 121]; consequently, the resulting numerical asymptotic solution is not uniform near the source. To overcome these initialization difficulties Babich [3] proposed to use an asymptotic series defined by the first Hankel function as an ansatz to expand the underlying highly-oscillatory wave field; the resulting eikonal equation is the same as the usual one, but the resulting transport equations are easily initialized. Moreover, Babich's expansion ensures that the Hankel-based ansatz yields a uniform asymptotic solution as $\omega \to \infty$ in the neighborhood of the point source and away from it. Although the Babich's ansatz as implemented in the current work in terms of solving eikonal and transport equations in physical space cannot deal with caustics directly, such an ansatz can be incorporated into the Huygens secondary-source principle to deal with caustics indirectly as shown in [75].

In this chapter we develop a simple and natural hybrid approach [35] to combine the asymptotic method and the ray-FEM to take advantage of the strengths of both methods for the high frequency Helmholtz equation with source singularity. In particular, we utilize the Babich's expansion and high-order numerical methods to compute the wave field near the source, and couple with the ray-FEM to compute the far field waves in smooth media.

4.1 The hybrid approach

We decompose u, the solution to (1.1) with point source term $f(\mathbf{x}) = \delta(\mathbf{x} - \mathbf{x}_0)$, into two components

$$u(\mathbf{x}) = u_{near}(\mathbf{x}) + u_{far}(\mathbf{x}), \tag{4.4}$$

where u_{near} is the near field solution which captures the source singularity, and u_{far} is the far field solution. We insert (4.4) into (1.1) and we have that

$$-\left(\Delta + \omega^2 m\right) u_{far} = \delta(\mathbf{x} - \mathbf{x}_0) + \left(\Delta + \omega^2 m\right) u_{near}. \tag{4.5}$$

Moreover, we suppose that u_{near} has the form

$$u_{near}(\mathbf{x}) = u_b(\mathbf{x})\chi_\epsilon(\mathbf{x}), \tag{4.6}$$

where u_b is the approximation given by the Babich's expansion and χ_ϵ is a smooth cut-off function satisfying,

$$\chi_\epsilon(\mathbf{x}) = \begin{cases} 1, & \text{if } |\mathbf{x} - \mathbf{x}_0| < \epsilon, \\ 0, & \text{if } |\mathbf{x} - \mathbf{x}_0| > 2\epsilon, \end{cases} \tag{4.7}$$

where ϵ is a fixed small number such that there are no caustics or ray crossing in $|\mathbf{x}-\mathbf{x}_0| < 2\epsilon$. Following a standard computation we have that

$$\left(\Delta + \omega^2 m\right) u_{near} = \left(\Delta u_b + \omega^2 m u_b\right) \chi_\epsilon + 2\nabla u_b \cdot \nabla \chi_\epsilon + u_b \Delta \chi_\epsilon, \tag{4.8}$$

furthermore, given that $\Delta u_b + \omega^2 m u_b = -\delta(\mathbf{x} - \mathbf{x}_0)$ and plugging into (4.5), we have that

$$-\left(\Delta + \omega^2 m\right) u_{far} = 2\nabla u_b \cdot \nabla \chi_\epsilon + u_b \Delta \chi_\epsilon, \tag{4.9}$$

whose right-hand side is smooth. Moreover, it can be easily computed accurately: χ_ϵ and its derivatives are known analytically, and it is possible to compute u_b accurately and efficiently in the support of χ_ϵ using the method developed in [103], as will be reviewed briefly in the sequel.

Given that $u_{far} = u - u_{near} \simeq (1 - \chi_\epsilon)u$, i.e., u_{far} is the far field solution of the Helmholtz equation, it satisfies absorbing or radiation conditions. Then we can solve the equation (4.9) in smooth media using the techniques developed in chapter 2 and [36] for high frequency Helmholtz equation (2.1) but with PML boundary conditions [15]. For simplicity, we consider the rectangular domain $\Omega = (-L_x, L_x) \times (-L_y, L_y)$ in 2D. We introduce

$$\delta_x(x) = \begin{cases} \frac{C}{\delta_{pml}} \left(\frac{x+L_x-\delta_{pml}}{\delta_{pml}}\right)^2, & \text{if } x \in (-L_x, -L_x + \delta_{pml}), \\ 0, & \text{if } x \in (-L_x + \delta_{pml}, L_x - \delta_{pml}), \\ \frac{C}{\delta_{pml}} \left(\frac{x-L_x+\delta_{pml}}{\delta_{pml}}\right)^2, & \text{if } x \in (L_x - \delta_{pml}, L_x), \end{cases} \tag{4.10}$$

and similarly for $\delta_y(y)$. Here δ_{pml} is typically around a couple of wavelengths, and C is an appropriate positive absorption constant independent of ω.

Then the equation (1.1) can be re-written [33] as

$$-\nabla \cdot (\mathbf{D}\nabla u) - \omega^2 m s_x s_y u = s_x s_y f \text{ in } \Omega, \qquad u = 0 \text{ on } \partial\Omega \tag{4.11}$$

where $\mathbf{D} = \begin{bmatrix} s_y/s_x & 0 \\ 0 & s_x/s_y \end{bmatrix}$, $s_x = 1 + i\sigma_x(x)/\omega$ and $s_y = 1 + i\sigma_y(y)/\omega$ with quadratic coefficient functions $\sigma_x(x)$ and $\sigma_y(y)$. The standard weak formulation is given by

$$\text{Find } u \in H_0^1(\Omega), \text{ such that } \mathcal{B}(u,v) = \mathcal{F}(v), \quad \forall v \in H_0^1(\Omega), \tag{4.12}$$

where

$$\mathcal{B}(u,v) := \int_\Omega (\mathbf{D}\nabla u) \cdot \nabla \overline{v} dV - \omega^2 \int_\Omega m s_x s_y u \overline{v} dV \tag{4.13}$$

$$\mathcal{F}(v) := \int_\Omega s_x s_y f \overline{v} dV, \quad f = 2\nabla u_b \cdot \nabla \chi_\epsilon + u_b \Delta \chi_\epsilon. \tag{4.14}$$

Finally, the proposed algorithm to compute the solution to (1.1) with a point source can be distilled to the following steps:

- compute the asymptotic solution u_b given by the Babich's expansion in a neighborhood of the source point,
- build the right-hand side in (4.9),
- solve (4.9), using the ray-FEM method with the adaptive learning basis approach

proposed in chapter 2,

- add the near field part u_{near} and the far field part u_{far}.

We explain each of the steps in detail below.

4.2 Babich's expansion

The reduction of (4.4) to (4.9) relies on computing a local approximation of the solution close to the source. This is achieved by using a specific asymptotic expansion of the solution, usually referred to as the Babich's expansion [3], which we briefly review here.

To solve (1.1) asymptotically when $\omega \to \infty$, Babich proposed the following Hankel-based ansatz [3] to expand the solution in a neighborhood of the source,

$$u(\mathbf{x}) = u_b(\mathbf{x}, \mathbf{x}_0, \omega) := \sum_{p=0}^{\infty} v_p(\mathbf{x}, \mathbf{x}_0) f_{p-(d-2)/2}(\omega, \phi(\mathbf{x}, \mathbf{x}_0)), \tag{4.15}$$

where d is the dimension,

$$f_q(\omega, \xi) := i\frac{\sqrt{\pi}}{2} e^{iq\pi} \left(\frac{2\xi}{\omega}\right)^q H_q^{(1)}(\omega\xi), \tag{4.16}$$

and ϕ is the phase or travel time function satisfying the eikonal equation,

$$|\nabla\phi(\mathbf{x}, \mathbf{x}_0)| = \frac{1}{c(\mathbf{x})}, \tag{4.17}$$

and $\{v_p\}_{p=0,1,2,\ldots}$ are assumed to be smooth functions satisfying a recursive system of transport equations,

$$\nabla\phi^2(\mathbf{x}) \cdot \nabla v_p(\mathbf{x}) + \left[(2p-d)m(\mathbf{x}) + \frac{1}{2}\Delta\phi^2(\mathbf{x})\right] v_p(\mathbf{x}) = \frac{1}{2}\Delta v_{p-1}(\mathbf{x}) \tag{4.18}$$

with initial conditions

$$v_{-1} \equiv 0, \quad v_0(\mathbf{x}_0) = \frac{m_0^{(d-2)/2}}{2\pi^{(d-1)/2}}, \quad m_0 = m(\mathbf{x}_0). \tag{4.19}$$

The problem is then reduced to solving the PDE system (4.17) and (4.18), which can be computed numerically. By using the high-order Eulerian asymptotic method developed in [103], it is possible to compute them accurately even close to the source. In this work, we only compute the first two terms of the Babich's expansion, namely u_{b_0} and u_{b_1}, where $u_{b_p} = v_p f_{p-(d-2)/2}$, $p = 0, 1$. Firstly, the phase ϕ is computed using a fifth-order Lax-Friedrichs weighted non-oscillatory (LxF-WENO) scheme [68, 127, 131] with the sixth-order factorization [1] [43, 76, 78] around the source. Then, the first amplitude coefficient v_0 is computed using the third-order LxF-WENO scheme with the third-order factorization around the source. The second amplitude coefficient v_1 is computed by the third-order LxF-WENO scheme with the first-order factorization around the source. Finally, the solution is approximated by replacing the numerically computed phase and amplitude coefficients into $u_{b_0} + u_{b_1}$. Below is a summary of the algorithm to approximate the symptotic Babich's expansion u_b and its gradient ∇u_b in the disk $D_{2\epsilon} := \{\mathbf{x} \in \Omega : |\mathbf{x} - \mathbf{x}_0| \leq 2\epsilon\}$ with mesh size h, and we denote by $u_b^h, \nabla u_b^h, u_{b_0}^h, u_{b_1}^h, \phi_h, v_0^h, v_1^h$ the numerically computed quantities of $u_b, \nabla u_b, u_{b_0}, u_{b_1}, \phi, v_0, v_1$ respectively. For further details, we refer the reader to [103].

---

[1] The solution is represented as a product or sum of the known solution to a homogeneous medium and an unkown factor or perturbation, which is smooth.

Algorithm 4 Babich's Expansion

```
function $[u_b^h, \nabla u_b^h, \{\boldsymbol{d}_b^h\}_{D_{2\epsilon}}] = \mathit{Babich}(\mathbf{x}_0, c, \omega, h)$
    $[\phi_h, \nabla\phi_h, v_0^h, \nabla v_0^h, v_1^h, \nabla v_1^h] = \mathit{Eikonal\text{-}Transport}(\mathbf{x}_0, c, h)$
    $\boldsymbol{d}_b^h = \frac{\nabla\phi_n(\mathbf{x})}{|\nabla\phi_n(\mathbf{x})|}$    ▷ Computing ray directions
    $\mathit{coef}_0 = i\frac{\sqrt{\pi}}{2},\ \mathit{coef}_1 = i\frac{\sqrt{\pi}}{\omega}\exp(i\pi)$    ▷ Coefficients of $f_q$ in (4.16)
    $\tilde{f}_0^h = H_0^{(1)}(\omega\phi_h),\ \tilde{f}_1^h = \phi_h H_1^{(1)}(\omega\phi_h)$    ▷ Hankel based terms of $f_q$ in (4.16)
    $u_{b_0}^h = \mathit{coef}_0 v_0^h \tilde{f}_0^h,\ u_{b_1}^h = \mathit{coef}_1 v_1^h \tilde{f}_1^h$    ▷ The first two terms in (4.15)
    $u_b^h = u_{b_0}^h + u_{b_1}^h$    ▷ Approximating the Babich's expansion
    $\nabla\tilde{f}_0^h = -\omega H_1^{(1)}(\omega\phi_h)\nabla\phi_h$    ▷ Computing gradients
    $\nabla\tilde{f}_1^h = 2H_1^{(1)}(\omega\phi_h)\nabla\phi_h - \omega\phi_h H_2^{(1)}(\omega\phi_h)\nabla\phi_h$
    $\nabla u_{b_0}^h = \mathit{coef}_0(\nabla v_0^h \tilde{f}_0^h + v_0^h \nabla\tilde{f}_0^h),\ \nabla u_{b_1}^h = \mathit{coef}_1(\nabla v_1^h \tilde{f}_1^h + v_1^h \nabla\tilde{f}_1^h)$
    $\nabla u_b^h = \nabla u_{b_0}^h + \nabla u_{b_1}^h$    ▷ Approximating the gradient of Babich's expansion
end function
```

Algorithm 5 Eikonal/Transport Solver

```
function $[\phi_h, \nabla\phi_h, v_0^h, \nabla v_0^h, v_1^h, \nabla v_1^h] = \mathit{Eikonal\text{-}Transport}(\mathbf{x}_0, c, h)$
    $\phi_h = \mathit{LxF\text{-}WENO\text{-}Fac}(5, 5, \mathbf{x}_0, c, h)$    ▷ Computing the phase in (4.17)
    $\nabla\phi_h^2 = \mathit{WENO}(3, \phi_h^2, h),\ \Delta\phi_h^2 = \mathit{FD}(4, \phi_h^2, h),\ \nabla\phi_h = \nabla\phi_h^2/2\phi_h$
    $v_0^h = \mathit{LxF\text{-}WENO\text{-}Fac}(3, 3, \nabla\phi_h^2, \Delta\phi_h^2, \mathbf{x}_0, c, h)$    ▷ Computing the first amplitude coefficient in (4.18)
    $\nabla v_0^h = \mathit{FD}(4, v_0^h, h),\ \Delta v_0^h = \mathit{FD}(4, v_0^h, h)$
    $v_1^h = \mathit{LxF\text{-}WENO\text{-}Fac}(3, 1, \nabla\phi_h^2, \Delta\phi_h^2, \Delta v_0^h, \mathbf{x}_0, c, h)$    ▷ Computing the second amplitude coefficient in (4.18)
    $\nabla v_1^h = \mathit{FD}(4, v_1^h, h)$
end function
```

Remark 3. *In Algorithm 4, we compute* u_b^h *and* ∇u_b^h *only in the annulus* $\epsilon \leq |\mathbf{x} - \mathbf{x}_0| \leq 2\epsilon$ *to build the right-hand side of equation* (4.9) *and* $\{\boldsymbol{d}_b^h\}_{D_{2\epsilon}}$ *to be used in the ray-FEM. In*

Algorithm 5, we denote by $\text{LxF-WENO-Fac}(p, q, \cdot)$ *the p-th order LxF-WENO scheme with q-th order factorization around the source,* $\text{WENO}(p, \cdot)$ *the p-th order WENO scheme and* $\text{FD}(p, \cdot)$ *the p-th order finite difference scheme.* $\nabla \phi_h^2$*,* $\nabla \phi_h$ *and* $\Delta \phi_h^2$ *are computed except for the points around the source.*

4.3 Error analysis

In this section, we provide an asymptotic error estimate of the high-frequency solution u to (1.1) by decomposing it into two parts: near field u_{near} computed using Babich's expansion [103] and far field u_{far} computed using the ray-FEM [36]. We remind the reader that we only focus on the 2D case with mesh size that scales as $\omega h = \mathcal{O}(1)$ in the high-frequency regime. We define notations $D_r := \{\mathbf{x} \in \Omega : |\mathbf{x} - \mathbf{x}_0| \leq r\}$, $D_{r_2 - r_1} := D_{r_2} \backslash D_{r_1} = \{\mathbf{x} \in \Omega : r_1 < |\mathbf{x} - \mathbf{x}_0| \leq r_2\}$.

4.3.1 Near field solution: Babich's expansion

We recall the basic properties of the first kind Hankel functions [66, 124]

$$\frac{d}{dz} H_q^1(z) = q \frac{H_q^{(1)}(z)}{z} - H_{q+1}^{(1)}(z), \tag{4.20}$$

$$H_q^{(1)}(z) = \begin{cases} \mathcal{O}(z^{-1/2}), & \text{if } |z| \to \infty, \\ \mathcal{O}(\ln z), & \text{if } |z| \to 0 \text{ and } q = 0, \\ \mathcal{O}(z^{-q}), & \text{if } |z| \to 0 \text{ and } q \geq 1. \end{cases} \tag{4.21}$$

In the disk $D_{2\epsilon}$, $\phi(\mathbf{x}) \leq \mathcal{O}(\epsilon) \leq C_1 =$ constant, the Hankel based terms $f_q(\omega, \xi)$ have the following asymptotic form [3] for large ω,

$$f_q(\omega,\xi) = \begin{cases} \mathcal{O}\left(\left(\frac{\xi}{\omega}\right)^q (\omega\xi)^{-1/2}\right) = \mathcal{O}(\omega^{-q-1/2}\xi^{q-1/2}), & \text{if } \omega\xi \geq C_2 = \text{constant}, \\ \mathcal{O}\left(\ln(\omega\xi)\right), & \text{if } \omega\xi \leq C_2 \text{ and } q = 0, \\ \mathcal{O}\left(\left(\frac{\xi}{\omega}\right)^q (\omega\xi)^{-q}\right) = \mathcal{O}(\omega^{-2q}), & \text{if } \omega\xi \leq C_2 \text{ and } q \geq 1. \end{cases} \tag{4.22}$$

Since the Babich's expansion (4.15) is approximated by the first two terms in Algorithm 4, i.e. $u_b \approx u_{b_0} + u_{b_1}$, where $u_{b_q} = v_q f_q$, $q = 0, 1$. We have the truncation error, asymptotically in ω,

$$\|u_b - (u_{b_0} + u_{b_1})\|_{L^\infty(D_{2\epsilon})} = \mathcal{O}(\omega^{-5/2}). \tag{4.23}$$

On the other hand, the phase ϕ and amplitude coefficients v_0, v_1 are numerically computed by Algorithm 5. According to Theorem 5.1 in [103] and Remark 3 in [75], the p-th order LxF-WENO scheme combines with q-th order factorization for equations (4.17) and (4.18) yield $min(p,q)$-th order accuracy for smooth ϕ and v's. Thus, we have

$$\|\phi - \phi_h\|_{L^\infty(D_{2\epsilon})} = \mathcal{O}(h^5), \quad \|v_0 - v_0^h\|_{L^\infty(D_{2\epsilon})} = \mathcal{O}(h^3), \quad \|v_1 - v_1^h\|_{L^\infty(D_{2\epsilon})} = \mathcal{O}(h). \tag{4.24}$$

Excluding a small neighborhood of the singular source point, i.e. $\mathbf{x} \in D_{2\epsilon-\eta}$, $\omega\phi(\mathbf{x}) \geq \mathcal{O}(\omega\eta) \geq C_2$ for a small positve number $\eta < \epsilon$, by mean value theorem there exists $\varphi \geq \min\{\phi(\mathbf{x}), \phi^h(\mathbf{x})\} \geq \mathcal{O}(\eta)$ such that

$$\begin{aligned} |H_0^{(1)}(\omega\phi(\mathbf{x})) - H_0^{(1)}(\omega\phi^h(\mathbf{x}))| &= |-H_1^{(1)}(\omega\varphi)(\omega\phi(\mathbf{x}) - \omega\phi^h(\mathbf{x}))| \\ &\lesssim \mathcal{O}((\omega\varphi)^{-1/2}\omega h^5) \lesssim \mathcal{O}(\omega^{1/2}\eta^{-1/2}h^5), \end{aligned} \tag{4.25}$$

the constants for $\lesssim$ and $\mathcal{O}(\cdot)$ only depend on constants C_1 and C_2. Thus, we have

$$\|f_0 - f_0^h\|_{L^\infty(D_{2\epsilon-\eta})} \lesssim \|H_0^{(1)}(\omega\phi) - H_0^{(1)}(\omega\phi^h)\|_{L^\infty(D_{2\epsilon-\eta})} = \mathcal{O}(\omega^{1/2}\eta^{-1/2}h^5)\ , \tag{4.26}$$

similarly, $\|f_1 - f_1^h\|_{L^\infty(D_{2\epsilon-\eta})} = \mathcal{O}(\omega^{-1/2}h^5 + \omega^{-3/2}\eta^{-1/2}h^5)$.

Hence,

$$\begin{aligned} \|u_{b_0} - u_{b_0}^h\|_{L^\infty(D_{2\epsilon-\eta})} &= \|v_0 f_0 - v_0^h f_0^h\|_{L^\infty(D_{2\epsilon-\eta})} \\ &= \|(v_0 f_0 - v_0^h f_0) + (v_0^h f_0 - v_0^h f_0^h)\|_{L^\infty(D_{2\epsilon-\eta})} \\ &\leq \|v_0 - v_0^h\|_{L^\infty(D_{2\epsilon-\eta})}\|f_0\|_{L^\infty(D_{2\epsilon-\eta})} \\ &\quad + \|v_0^h\|_{L^\infty(D_{2\epsilon-\eta})}\|f_0 - f_0^h\|_{L^\infty(D_{2\epsilon-\eta})} \\ &= \mathcal{O}(\omega^{-1/2}\eta^{-1/2}h^3 + \omega^{1/2}\eta^{-1/2}h^5) \end{aligned} \tag{4.27}$$

and analogously,

$$\|u_{b_1} - u_{b_1}^h\|_{L^\infty(D_{2\epsilon-\eta})} = \mathcal{O}(\omega^{-3/2}h + \omega^{-1/2}h^5 + \omega^{-3/2}\eta^{-1/2}h^5) \tag{4.28}$$

Therefore, under the assumption of $h = \mathcal{O}(\omega^{-1})$ and $\frac{C_2}{\omega} \leq \mathcal{O}(\eta) \leq \phi \leq \mathcal{O}(\epsilon) \leq C_1$, the asymptotic error with respect to ω of Babich's expansion is

$$\begin{aligned} \|u_b - u_b^h\|_{L^\infty(D_{2\epsilon-\eta})} &= \|u_b - u_{b_0}^h - u_{b_1}^h\|_{L^\infty(D_{2\epsilon-\eta})} \\ &= \|(u_b - u_{b_0} - u_{b_1}) + (u_{b_0} - u_{b_0}^h) + (u_{b_1} - u_{b_1}^h)\|_{L^\infty(D_{2\epsilon-\eta})} \\ &\leq \|u_b - u_{b_0} - u_{b_1}\|_{L^\infty(D_{2\epsilon-\eta})} \\ &\quad + \|u_{b_0} - u_{b_0}^h\|_{L^\infty(D_{2\epsilon-\eta})} + \|u_{b_1} - u_{b_1}^h\|_{L^\infty(D_{2\epsilon-\eta})} \\ &= \mathcal{O}(\omega^{-5/2}) + \mathcal{O}(\omega^{-3}) + \mathcal{O}(\omega^{-5/2}) \\ &= \mathcal{O}(\omega^{-5/2}). \end{aligned} \tag{4.29}$$

4.3.2 Right-hand side for the far field equation

Given that the Babich's expansion u_b is computed accurately and the cut-off function χ_ϵ is know analytically, we can construct the near field solution $u_{near} = u_b\chi_\epsilon$. On the other hand, in order to obtain the far field solution u_{far}, we need to solve the equation (4.9). Most stability and error analysis for finite element methods [85, 88, 126] rely on the norms of the right-hand side (RHS). Moreover, numerical experiments show that the error of numerical solution is tightly bounded by the norm of RHS in this case, i.e. if the norm of the RHS is ω dependent, the error will grow as ω grows. Thus, it is crucial to have asymptotic orders of the norms of the RHS in (4.9) with respect to ω and ϵ. We use the analytical expression of the cut-off function and Babich's expansion to obtain such scalings in L^∞ and L^2 norm.

We define the smooth cut-off function

$$\chi_\epsilon(\mathbf{x},\mathbf{x}_0) = \begin{cases} 1, & \text{if } |\mathbf{x}-\mathbf{x}_0| \le \epsilon, \\ \exp\left(\frac{2e^{-1/t}}{t-1}\right), & \text{if } \epsilon < |\mathbf{x}-\mathbf{x}_0| < 2\epsilon, t = \frac{|\mathbf{x}-\mathbf{x}_0|}{\epsilon} - 1, \\ 0, & \text{if } |\mathbf{x}-\mathbf{x}_0| \ge 2\epsilon, \end{cases} \tag{4.30}$$

and we choose ϵ small enough such that $\chi_\epsilon(\mathbf{x},\mathbf{x}_0)$ is compactly supported within the computational domain Ω, i.e. $D_{2\epsilon} \subseteq \Omega$ and no caustics or multi-pathing has occured. We can easily verify that $\chi_\epsilon \in \mathcal{C}^\infty(\mathbb{R})$, $\nabla\chi_\epsilon$ and $\Delta\chi_\epsilon$ vanishes in $D^c_{2\epsilon-\epsilon} := \{\mathbf{x} \in \Omega : |\mathbf{x}-\mathbf{x}_0| > 2\epsilon \text{ or } |\mathbf{x}-\mathbf{x}_0| < \epsilon\}$. Moreover, based on the derivatives of the first kind Hankel functions (4.20) and its asymptotic expansions (4.21), we have the asymptotic orders of the right hand side as displayed in Table 4.1. The scalings imply that when $\omega\epsilon \gg 1$, the first term $2\nabla u_b \cdot \nabla\chi_\epsilon$ dominates the right-hand side. In the high frequency regime, we pick small but fixed ϵ. Hence the right-hand side scales as $\mathcal{O}(\omega^{\frac{1}{2}})$ as $\omega \to \infty$.

$\Omega \subseteq \mathbb{R}^2$	$\nabla \chi_\epsilon$	$\Delta \chi_\epsilon$	$2\nabla u_b \cdot \nabla \chi_\epsilon$	$u_b \Delta \chi_\epsilon$	$2\nabla u_b \cdot \nabla \chi_\epsilon + u_b \Delta \chi_\epsilon$
$\lVert \cdot \rVert_{L^\infty(\Omega)}$	$\mathcal{O}(\epsilon^{-1})$	$\mathcal{O}(\epsilon^{-2})$	$\mathcal{O}(\omega^{\frac{1}{2}}\epsilon^{-\frac{3}{2}})$	$\mathcal{O}(\omega^{-\frac{1}{2}}\epsilon^{-\frac{5}{2}})$	$\mathcal{O}(\omega^{\frac{1}{2}}\epsilon^{-\frac{3}{2}}) + \mathcal{O}(\omega^{-\frac{1}{2}}\epsilon^{-\frac{5}{2}})$
$\lVert \cdot \rVert_{L^2(\Omega)}$	$\mathcal{O}(\epsilon^{0})$	$\mathcal{O}(\epsilon^{-1})$	$\mathcal{O}(\omega^{\frac{1}{2}}\epsilon^{-\frac{1}{2}})$	$\mathcal{O}(\omega^{-\frac{1}{2}}\epsilon^{-\frac{3}{2}})$	$\mathcal{O}(\omega^{\frac{1}{2}}\epsilon^{-\frac{1}{2}}) + \mathcal{O}(\omega^{-\frac{1}{2}}\epsilon^{-\frac{3}{2}})$

Table 4.1: Asymptotic orders of the right-hand side with respect to ω and ϵ.

4.3.3 Far field solution: ray-FEM

After constructing the ω-dependent right hand side of (4.9), we use ray-FEM to solve the equation with ray directions extracted numerically by NMLA from computed low frequency wave field. Now we provide an upper bound of the approximation error

$$\inf_{u_h \in V^h_{Ray}(\mathcal{T}_h)} \frac{\lVert u_{far} - u^h_{far} \rVert_{L^2(\Omega)}}{\lVert u_{far} \rVert_{L^2(\Omega)}}, \tag{4.31}$$

where the ray-FEM space, $V^h_{Ray}(\mathcal{T}_h)$, incorporates the estimated ray directions $\{\widehat{\mathbf{d}}^h_j\}$. From section 3.3 the error for estimation by NMLA is $|\widehat{\mathbf{d}}_j - \widehat{\mathbf{d}}^h_j| \sim \mathcal{O}(\omega^{-1/2})$.

For the simplicity of error analysis, we assume that there is no ray crossing in the domain Ω, no reflections from the boundary $\partial\Omega$, and the Babich's expansion (4.15) is the exact solution of equation (1.1). Then the far field solution to equation (4.9) is

$$u_{far} = u - u_{near} = u_b - u_b \chi_\epsilon = (1 - \chi_\epsilon) u_b. \tag{4.32}$$

Note that $(1-\chi_\epsilon)u_b$ vanishes in the disk D_ϵ, using the first term u_{b_0} to approximate Babich's expansion outside disk D_ϵ we have truncation error $\mathcal{O}(\omega^{-3/2})$ similar to (4.23),

$$u_{far} = (1 - \chi_\epsilon) u_b = (1 - \chi_\epsilon) u_{b_0} + \mathcal{O}(\omega^{-3/2}) = \omega^{-1/2} A(\mathbf{x}) e^{i\omega\phi(\mathbf{x})} + \mathcal{O}(\omega^{-3/2}), \tag{4.33}$$

where $A(x) = i\frac{\sqrt{\pi\omega}}{2}(1-\chi_\epsilon) H_0^{(1)}\left(\omega\phi(\mathbf{x})\right) e^{i\omega\phi(\mathbf{x})}$ is a smooth amplitude function with a support outside disk D_ϵ. Thus, asymptotically we have

$$\|u_{far}\|_{L^2(\Omega)} = \mathcal{O}(\omega^{-1/2}). \tag{4.34}$$

Moreover, we denote by

$$\begin{aligned} u_I &= \textstyle\sum_{j=1}^{N_h} \omega^{-1/2} A(\mathbf{x}_j)\varphi_j(\mathbf{x}) e^{i\omega[\phi(\mathbf{x}_j)+1/c(\mathbf{x}_j)\widehat{\mathbf{d}}_j\cdot(\mathbf{x}-\mathbf{x}_j)]}, \\ u_I^h &= \textstyle\sum_{j=1}^{N_h} \omega^{-1/2} A(\mathbf{x}_j)\varphi_j(\mathbf{x}) e^{i\omega[\phi(\mathbf{x}_j)+1/c(\mathbf{x}_j)\widehat{\mathbf{d}}_j^h\cdot(\mathbf{x}-\mathbf{x}_j)]} \end{aligned} \tag{4.35}$$

the nodal interpolations of the solution in $V_{Ray}(\mathcal{T}_h)$ and $V_{Ray}^h(\mathcal{T}_h)$ with exact and numerical ray direction, respectively. For smooth A and ϕ, from [36] we have

$$||u_{far} - u_I||_{L^2(\Omega)} \lesssim \omega^{-1/2}h^2|A|_{H^2(\Omega)} + \omega^{1/2}h^2\|A\|_{L^\infty(\Omega)}\|\nabla^2\phi\|_{L^\infty(\Omega)} + \mathcal{O}(\omega^{-3/2}), \tag{4.36}$$

and

$$||u_I - u_I^h||_{L^2(\Omega)} \lesssim \omega^{1/2}h\|A\|_{L^\infty(\Omega)}\|c^{-1}\|_{L^\infty(\Omega)}\|\widehat{\mathbf{d}}_j - \widehat{\mathbf{d}}_j^h\|_{L^\infty(\Omega)} \lesssim h\|A\|_{L^\infty(\Omega)}\|c^{-1}\|_{L^\infty(\Omega)}, \tag{4.37}$$

the constants in $\lesssim$ only depend on the domain Ω. Hence, we have the error estimate, more compactly with respect to ω on the mesh with $h = \mathcal{O}(\omega^{-1})$,

$$\begin{aligned} \textstyle\inf_{u_{far}^h \in V_{Ray}^h(\mathcal{T}_h)} \|u_{far} - u_{far}^h\|_{L^2(\Omega)} &\le \|u_{far} - u_I^h\|_{L^2(\Omega)} \\ &\le \|u_{far} - u_I\|_{L^2(\Omega)} + \|u_I - u_I^h\|_{L^2(\Omega)} \\ &= \mathcal{O}(\omega^{-1/2}h^2 + \omega^{1/2}h^2 + h + \omega^{-3/2}) \\ &= \mathcal{O}(\omega^{-1}). \end{aligned} \tag{4.38}$$

Therefore,

$$\inf_{u_h \in V_{Ray}^h(\mathcal{T}_h)} \frac{\|u_{far} - u_{far}^h\|_{L^2(\Omega)}}{\|u_{far}\|_{L^2(\Omega)}} = \mathcal{O}(\omega^{-1/2}). \tag{4.39}$$

We point out that the desirable relative convergence rate in this case is $\mathcal{O}(\omega^{-1})$. However, the error in the estimation of dominant wave directions using NMLA, which is $\mathcal{O}(\omega^{-1/2})$, dominates the total error and becomes the bottleneck to improve the overall convergence order. This error is due to the deviation of a general wave front from a plane wave form which is one of the underpinnings of assumptions for micro local analysis.

4.3.4 Adding near field solution and far field solution

Adding the near field solution u_{near} with the far field solution u_{far} and considering the error excluding a small disk D_η, we can obtain the error estimate for the numerical solution to (1.1). Indeed,

$$\begin{aligned} \|u - u_h\|_{L^2(\Omega\setminus D_\eta)} &= \|(u_{near} + u_{far}) - (u^h_{near} + u^h_{far})\|_{L^2(\Omega\setminus D_\eta)} \\ &\le \|(u - u^h_b)\chi_\epsilon\|_{L^2(\Omega\setminus D_\eta)} + \|u_{far} - u^h_{far}\|_{L^2(\Omega\setminus D_\eta)} \\ &\le \|u - u^h_b\|_{L^2(D_{2\epsilon-\eta})} + \|u_{far} - u^h_{far}\|_{L^2(\Omega)}, \end{aligned} \tag{4.40}$$

from (4.29) and (3.21), we have

$$\inf_{u^h_{far}\in V^h_{Ray}(\mathcal{T}_h)} \|u - (u^h_b\chi_\epsilon + u^h_{smooth})\|_{L^2(\Omega\setminus D_\eta)} = \mathcal{O}(\omega^{-1}). \tag{4.41}$$

Moreover, based on asymptotic forms in (4.21) and (4.22), we have

$$\|u\|_{L^2(\Omega\setminus D_\eta)} = \mathcal{O}(\eta^{-1/2}\omega^{-1/2}), \tag{4.42}$$

and finally we obtain

$$\inf_{u^h_{far}\in V^h_{Ray}(\mathcal{T}_h)} \frac{\|u - (u^h_b\chi_\epsilon + u^h_{far})\|_{L^2(\Omega\setminus D_\eta)}}{\|u\|_{L^2(\Omega\setminus D_\eta)}} = \mathcal{O}(\eta^{1/2}\omega^{-1/2}), \tag{4.43}$$

where the constant in $\mathcal{O}(\cdot)$ only depends on constants C_1 and C_2.

Chapter 5

Algorithms

In this chapter we provide the full algorithm for solving the high frequency Helmholtz equation (1.1), including, a hybrid solver combines Babich's asymptotic expansion close to the point source and the ray-FEM to compute the smooth far field; and a fast iterative solver based on a modification of the method of polarized traces [129] for the resulting linear systems. In order to streamline the presentation and to make the algorithm easier to understand, we introduce several subroutines.

More specifically, we separate the full algorithm into three conceptual stages:

1. probing the medium by solving a relatively low-frequency Helmholtz equation with the standard FEM;
2. learning the dominant ray directions from the low-frequency probed wave field by NMLA;
3. solving the high-frequency Helmholtz equation in the ray-FEM space.

If necessary the second stage can be iteratively applied to the high-frequency wave field computed in stage 3 to improve the estimation of dominant ray directions and then repeat stage 3 to obtain more accurate high-frequency wave field.

We remind the reader that the ultimate objective of the algorithm presented in this thesis (i.e., Algorithm 9 and 10) is to solve the Helmholtz equation (1.1) at frequency ω with a total $\mathcal{O}(\omega^d)$ (up to poly-logarithmic factors) computational complexity. In order to achieve this objective, we discretize the PDE with a mesh size $h = \mathcal{O}(\omega^{-1})$, which leads to a total of $\mathcal{O}(\omega^d)$ number of degrees of freedom and a sparse linear system with $\mathcal{O}(\omega^d)$ number of non-zeros. Then we develop a fast iterative solver with quasi-linear complexity to solve the resulting linear system after discretization. Below is a more detailed description of the three stages. Finally, following the notation defined in the prequel, we denote the triangular mesh by $\mathcal{T}_h$.

5.1 Probing

We first solve the low-frequency Helmholtz equation (1.4) with $\widetilde{\omega} \sim \sqrt{\omega}$ in the same medium and with the same source on $\mathcal{T}_h$. The low-frequency problem is solved using the standard finite element method (S-FEM) with linear elements as prescribed by Algorithm 6.

Algorithm 6 Standard FEM Helmholtz Solver

```
function $\mathbf{u}_{\omega,h}$ = S-FEM($\omega, h, c, f, g$)
    for $i, j = 1 : N_h$ do
        $\mathbf{H}_{i,j} = \mathcal{B}(\varphi_i, \varphi_j)$          ▷ Assemble Helmholtz matrix
        $\mathbf{b}_j = \mathcal{F}(\varphi_j)$          ▷ Assemble right-hand side
    end for
    $\mathbf{u}_{\omega,h} = \mathbf{H}^{-1}\mathbf{b}$          ▷ Solve linear system
end function
```

Let $\mathbf{u}_{\widetilde{\omega},h} = \text{S-FEM}\ (\widetilde{\omega}, h, c, f, g)$ denote the S-FEM solution of the low-frequency Helmholtz equation on $\mathcal{T}_h$. Since $\tilde{\omega}^2 h = \mathcal{O}(1)$, S-FEM is quasi-optimal in the norm $\|\cdot\|_{\mathcal{H}} := \|\nabla \cdot\|_{L^2} + k\|\cdot\|_{L^2}$ [86], and it has an optimal L^2 error estimate [126].

5.2 Learning

Once the low-frequency problem has been solved, we extract the dominant ray directions from $\mathbf{u}_{\widetilde{\omega},h}$ using NMLA as described in section 3.1 around each mesh node. We utilize the smoothness of the phase functions, and hence the smoothness of the ray directions field to reduce the computational cost. The reduction is achieved by restricting the learning of the dominant ray directions to vertices of a coarse mesh down-sampled from $\mathcal{T}_h$. Such re-meshed coarse mesh is denoted by $\mathcal{T}_{h_c} = \{K^c\}$, where $h_c = \mathcal{O}(\sqrt{h})$. The resulting dominant ray directions are then linearly interpolated onto the fine mesh $\mathcal{T}_h$.

Note that at each vertex of $\mathcal{T}_{h_c}$, the wave field $\mathbf{u}_{\widetilde{\omega},h}$ on the fine mesh $\mathcal{T}_h$ is used by NMLA to estimate the dominant ray directions. There are three sources of errors in the learning stage:

- numerical errors of $\mathbf{u}_{\widetilde{\omega},h}$;
- model errors in the geometric-optics ansatz;
- interpolation errors.

The numerical error for $\mathbf{u}_{\widetilde{\omega},h}$ by Algorithm 6 in the L^2 norm [126] is $\mathcal{O}(\widetilde{\omega}h^2 + \widetilde{\omega}^2 h^2) = \mathcal{O}(\omega^{-1})$, which is negligible with respect to the model error in the geometric optics ansatz. The error introduced by the geometric optics approximation and NMLA is $\mathcal{O}(\widetilde{\omega}^{-\frac{1}{2}})$ as shown in section 3.1 and 3.3. The error due to the linear interpolation on $\mathcal{T}_{h_c}$ to obtain the ray direction estimations at every vertex on $\mathcal{T}_h$ is $\mathcal{O}(h_c^2) = \mathcal{O}(h) = \mathcal{O}(\omega^{-1})$, which is much smaller than the model error in the geometric-optics ansatz. Hence the overall error in the ray direction estimation based on NMLA on $\mathbf{u}_{\widetilde{\omega},h}$ and interpolation is $\mathcal{O}(\widetilde{\omega}^{-\frac{1}{2}})$. The dominant ray direction estimation algorithm is summarized in Algorithm 7. For each node $\mathbf{x}_j$ on mesh $\mathcal{T}_h$ the number of dominant ray directions is denoted by n_j, $\boldsymbol{d}^j_{\omega,h} = \{\mathbf{d}^{j,l}_{\omega,h}\}_{l=1}^{n_j}$.

Algorithm 7 Ray Learning

```
function $\{\boldsymbol{d}^j_{\omega,h}\}_{j=1}^{N_h} = \textsc{RayLearning}(\omega, h, h_c, c, \mathbf{u}_{\omega,h})$
    for $j = 1 : N_{h_c}$ do
        $\boldsymbol{d}^j_{\omega,h_c} = NMLA(\mathbf{x}^c_j, \mathcal{T}_h, \omega, h, c, \mathbf{u}_{\omega,h})$
    end for
    $\{\boldsymbol{d}^j_{\omega,h}\}_{j=1}^{N_h} = LinearInterpolation(\mathcal{T}_{h_c}, \mathcal{T}_h, \{\boldsymbol{d}^j_{\omega,h_c}\}_{j=1}^{N_{h_c}})$
end function
```

5.3 High-frequency solver

Once the dominant ray directions on $\mathcal{T}_h$ have been computed, we can construct the ray-FEM space $V_{Ray}(\mathcal{T}_h)$ and solve the high-frequency Helmholtz equations following (2.16), which is implemented in Algorithm 8.

Algorithm 8 Ray-FEM Helmholtz Solver

```
function $\mathbf{u}_{\mathbf{d}_\omega,h} = \textsc{Ray-FEM}(\omega, h, c, f, g, \{\boldsymbol{d}^j_{\omega,h}\}_{j=1}^{N_h})$
    $N_{dof} = 0$
    for $j = 1 : N_h, l = 1 : n_j$ do
        $N_{dof} = N_{dof} + 1$, $m = N_{dof}$
        $\psi_m(\mathbf{x}) = \varphi_j(\mathbf{x}) e^{iw/c(\mathbf{x}_j)\mathbf{d}_{j,l}\cdot\mathbf{x}}$        ▷ Construct ray-FEM basis functions
        $\widehat{\psi} = \psi_m(\mathbf{x}_j)$        ▷ Nodal values of ray-FEM basis functions
    end for
    for $m, n = 1 : N_{dof}$ do
        $\mathbf{H}_{m,n} = \mathcal{B}(\psi_m, \psi_n)$        ▷ Assemble Helmholtz matrix
        $\mathbf{b}_n = \mathcal{F}(\psi_n)$        ▷ Assemble right-hand side
    end for
    $\mathbf{v} = \mathbf{H}^{-1}\mathbf{b}$        ▷ Coefficients of ray-FEM basis functions
    $\mathbf{u}_{\mathbf{d}_\omega,h} = \mathbf{v} \cdot \widehat{\boldsymbol{\psi}}$        ▷ Ray-FEM solution on mesh nodes
end function
```

In general, the accuracy of the solution computed by Algorithm 8, using the ray-FEM method depends on the accuracy of the computed dominant wave directions. From section 5.2, the accuracy order of the learning stage from the low-frequency wave field is $\mathcal{O}(\widetilde{\omega}^{-\frac{1}{2}})$, and following the error analysis of section 3.5, the consequent ray-FEM solution has the same order of accuracy. However, the iterative ray-FEM Helmholtz solver, as presented in Algorithm 9, provides a way to improve approximations for both dominant ray directions and the high-frequency wave field.

Algorithm 9 Iterative Ray-FEM High-Frequency Helmholtz Solver

```
function $\mathbf{u}_{\mathbf{d}_\omega,h}$ = IterRay-FEM$(\omega, c, f, g)$
    $\widetilde{\omega} \sim \sqrt{\omega}$, $h \sim \omega^{-1}$, $h_c \sim \omega^{-\frac{1}{2}}$
    $\mathbf{u}_{\widetilde{\omega},h} = S\text{-}FEM(\widetilde{\omega}, h, c, f, g)$    ▷ Low-frequency waves
    $\{\boldsymbol{d}_{\widetilde{\omega},h}\} = RayLearning(\widetilde{\omega}, h, h_c, c, \mathbf{u}_{\widetilde{\omega},h})$    ▷ Low-frequency ray learning
    $\mathbf{u}_{\mathbf{d}_{\widetilde{\omega}},h} = Ray\text{-}FEM(\omega, h, c, f, g, \{\boldsymbol{d}_{\widetilde{\omega},h}\})$    ▷ High-frequency waves
    $tol = 1$, $niter = 0$, $\mathbf{u}^1_{\omega,h} = \mathbf{u}_{\mathbf{d}_{\widetilde{\omega}},h}$
    while $tol > \epsilon$ or $niter > max\_iter$ do
        $\{\mathbf{d}_{\omega,h}\} = RayLearning(\omega, h, h_c, c, \mathbf{u}^1_{\omega,h})$    ▷ High-frequency ray learning
        $\mathbf{u}_{\mathbf{d}_\omega,h} = Ray\text{-}FEM(\omega, h, c, f, g, \{\mathbf{d}_{\omega,h}\})$, $\mathbf{u}^2_{\omega,h} = \mathbf{u}_{\mathbf{d}_\omega,h}$
        $tol = \|\mathbf{u}^1_{\omega,h} - \mathbf{u}^2_{\omega,h}\|_{L^2(\Omega)} / \|\mathbf{u}^2_{\omega,h}\|_{L^2(\Omega)}$
        $niter = niter + 1$, $\mathbf{u}^1_{\omega,h} = \mathbf{u}^2_{\omega,h}$
    end while
end function
```

Remark 4. *Extensive numerical experiments and section 3.2 indicate that the NMLA process in learning dominant ray directions stage is remarkably stable even for noisy plane wave data. Hence, the iterative process in Algorithm 9 usually needs very few iterations to reach the desired accuracy. Typically, we only need one or two iterations in our numerical tests.*

Remark 5. *Since NMLA can not be used to estimate ray directions near the point source, the hybrid solver is introduced in next section to handle source singularity. Moreover, a slight modification of Algorithm 9 also could be used for solving a point source inside domain problem. First, we approximate the right hand side with the associated column of the mass matrix (normalized by mesh size h). Moreover, we use a standard finite element basis function at the source point. For vertices near the source, we apply the radial directions (exact ray directions in homogeneous medium) in the construction of the approximation space for the ray-FEM method. Meanwhile, for vertices away from the source, we find the dominant ray directions by NMLA. Under this modification, ray-FEM can capture the phase accurately* *and it will be demonstrated numerically in section 7.2.*

5.4 Hybrid solver

In this section we provide Algorithm 10 to implement the hybrid method for solving the high-frequency problem (1.1) with point source terms. The full algorithm starts by computing low frequency wave field and ray directions in the near field using Babich's expansion in line 3. Then it solves a relative low-frequency Helmholtz equation (1.4) with the standard FEM to probe the medium and to learn the dominant ray directions in the far field within line 5-8. Afterwards, the high-frequency wave field near the source is computed using the Babich's expansion in line 9. Moreover, the far field solution of the high-frequency equation (4.9) is computed using the ray-FEM which incorporates those learned local dominant ray directions in line 11. Lastly, the ray estimation is improved by iteratively applying NMLA to high-frequency waves in the far field and then the resulting rays are incorporated into the ray-FEM space to obtain more accurate high-frequency waves in the while loop from line 14 to line 21.

Algorithm 10 Hybrid High-Frequency Helmholtz Solver

```
function $\mathbf{u}_{\omega,h} = \textsc{Hybrid-Solver}(\mathbf{x}_0, c, \omega)$
    $\widetilde{\omega} \sim \sqrt{\omega}$, $h \sim \omega^{-1}$, $h_c \sim \omega^{-\frac{1}{2}}$    ▷ Low frequency and mesh sizes
    $[u^h_{\widetilde{\omega},b}, \nabla u^h_{\widetilde{\omega},b}, \{\boldsymbol{d}^h_b\}_{D_{2\epsilon}}] = \mathit{Babich}(\mathbf{x}_0, c, \widetilde{\omega}, h)$    ▷ Babich's expansion in disk $D_{2\epsilon}$
    $f_{\widetilde{\omega}} = 2\nabla u^h_{\widetilde{\omega},b} \cdot \nabla \chi_\epsilon + u^h_{\widetilde{\omega},b} \Delta \chi_\epsilon$    ▷ Right hand side in (4.9)
    $\mathbf{u}^{far}_{\widetilde{\omega},h} = \mathit{S\text{-}FEM}(\widetilde{\omega}, h, c, f_{\widetilde{\omega}}, g_{\mathbf{u}^{far}_{\widetilde{\omega}}})$    ▷ Low frequency solution to (1.4)
    $\mathbf{u}_{\widetilde{\omega},h} = \mathbf{u}^{far}_{\widetilde{\omega},h} + u^h_{\widetilde{\omega},b} \chi_\epsilon$    ▷ Low-frequency waves
    $\{\boldsymbol{d}^h_{\widetilde{\omega}}\}_{\Omega \backslash D_{2\epsilon}} = \mathit{RayLearning}(\widetilde{\omega}, h, h_c, c, \mathbf{u}_{\widetilde{\omega},h})$    ▷ Ray learning in far field
    $\{\boldsymbol{d}^h_{\widetilde{\omega}}\}_{\Omega} = \{\boldsymbol{d}^h_{\widetilde{\omega}}\}_{\Omega \backslash D_{2\epsilon}} \cup \{\boldsymbol{d}^h_b\}_{D_{2\epsilon}}$    ▷ Low-frequency rays
    $[u^h_{\omega,b}, \nabla u^h_{\omega,b}] = \mathit{Babich}(\mathbf{x}_0, c, \omega, h)$
    $f_\omega = 2\nabla u^h_{\omega,b} \cdot \nabla \chi_\epsilon + u^h_{\omega,b} \Delta \chi_\epsilon$
    $\mathbf{u}^{far}_{\mathbf{d}_{\widetilde{\omega}},h} = \mathit{Ray\text{-}FEM}(\omega, h, c, f_\omega, g_{u^{far}_\omega}, \{\boldsymbol{d}^h_{\widetilde{\omega}}\}_\Omega)$    ▷ High-frequency solution to (4.9)
    $\mathbf{u}^1_{\omega,h} = \mathbf{u}^{far}_{\mathbf{d}_{\widetilde{\omega}},h} + u^h_{\omega,b} \chi_\epsilon$    ▷ High-frequency waves
    $\mathit{tol} = 1$, $\mathit{niter} = 0$,
    while $\mathit{tol} > \epsilon$ and $\mathit{niter} < \mathit{max\_iter}$ do
        $\{\mathbf{d}^h_\omega\}_{\Omega \backslash D_{2\epsilon}} = \mathit{RayLearning}(\omega, h, h_c, c, \mathbf{u}^1_{\omega,h})$
        $\{\boldsymbol{d}^h_\omega\}_\Omega = \{\boldsymbol{d}^h_\omega\}_{\Omega \backslash D_{2\epsilon}} \cup \{\boldsymbol{d}^h_b\}_{D_{2\epsilon}}$    ▷ High-frequency rays
        $\mathbf{u}^{far}_{\mathbf{d}_\omega,h} = \mathit{Ray\text{-}FEM}(\omega, h, c, f_\omega, g_{u^{far}_\omega}, \{\mathbf{d}^h_\omega\}_\Omega)$
        $\mathbf{u}^2_{\omega,h} = \mathbf{u}^{far}_{\mathbf{d}_\omega,h} + u^h_{\omega,b} \chi_\epsilon$
        $\mathit{tol} = \|\mathbf{u}^1_{\omega,h} - \mathbf{u}^2_{\omega,h}\|_{L^2(\Omega)} / \|\mathbf{u}^2_{\omega,h}\|_{L^2(\Omega)}$
        $\mathit{niter} = \mathit{niter} + 1$, $\mathbf{u}^1_{\omega,h} = \mathbf{u}^2_{\omega,h}$
    end while
    $\mathbf{u}_{\omega,h} = \mathbf{u}^1_{\omega,h}$
end function
```

5.5 Fast linear solver

To achieve the quasi-linear overall complexity mentioned in the introduction, it is necessary to solve the linear system resulting from both standard and ray-based FEMs, which we write in a generic form as

$$\mathbf{H}\mathbf{u} = \mathbf{f}, \tag{5.1}$$

in a linear complexity (up to poly-logarithmic factors). This solver is, in fact, the computational bottleneck of Algorithms 6 and 8.

For a smooth medium, this can be achieved by modifying the method of polarized traces [129], of which we provide a brief review here. For further details we refer the interested readers to [129]. The method of polarized traces is a domain decomposition method that encompasses the following aspects:

- layered domain decompositions;
- absorbing boundary conditions between subdomains implemented via PML [15];
- transmission conditions issued from a discrete Green's representation formula;
- efficient pre-conditioners arising from localization of the waves via an incomplete Green's formula.

The first two aspects can be effortlessly implemented. Consider a layered partition of Ω into L slabs, or layers $\{\Omega^\ell\}_{\ell=1}^{L}$. Define f^ℓ as the restriction of f to Ω^ℓ, i.e., $f^\ell = f\chi_{\Omega^\ell}$; and define the local Helmholtz operators as

$$\mathcal{H}^\ell u := \left(-\Delta - \omega^2/c^2\right) u \qquad \text{in } \Omega^\ell, \tag{5.2}$$

with absorbing boundary conditions implemented via PML around the slabs.

The method of polarized traces aims at solving the global linear system in (5.1) by solving the local systems $\mathbf{H}^{\ell}$, which are the discrete version of (5.2). In order to solve the global system, or in this case, to find a good approximate solution, we need to "glue" the subdomains together. This is achieved via a discrete Green's integral formula deduced by imposing discontinuous solutions.

In the original formulation of the method of polarized traces [129], the Green's representation formula was used to build a global surface integral equation (SIE) at the interfaces between slabs. The SIE was solved using an efficient preconditioner coupled with a multilevel compression of the discrete kernels to accelerate the on-line stage of the algorithm. The original algorithm had an embarrassingly parallel superlinear off-line complexity which was amortized among a large number of right-hand sides, which represents a typical situation in exploration geophysics.

In the context of this thesis, the linear systems issued from the ray-based FEM depend on the source distribution, making it impossible to amortize a super-linear off-line cost. In order to reduce the off-line cost we use a matrix-free formulation (see chapter 2 in [128]) with a domain decomposition in thin layers.

In general, the number of iterations for convergence will depend on the quality of the absorbing boundary conditions, and the wave speed. In the best case, the number of iterations will depend on the number of physical reflections across subdomains. For a smooth and fixed wave speed, several numerical experiments indicate that the number of iterations to convergence is weakly dependent on the frequency; i.e., the number of iterations scales as $\mathcal{O}(\log \omega)$, meaning that the cost is dominated by the factorization and solve of each local linear system.

If we suppose that Ω is discretized into $N = \mathcal{O}(n^2)$ elements, and that each slab is only $\mathcal{O}(1)$

elements thick, then we have that factorizing all the local problems using a multifrontal method [29, 48] (in this case UMFPACK [28]) will have an asymptotic cost of $\mathcal{O}(n)$, which has to be performed $\mathcal{O}(n)$ times, leading to an off-line cost of $\mathcal{O}(N)$.

For the preconditioning, we need to solve $\mathcal{O}(n)$ quasi 1-D linear systems, which can be performed in $\mathcal{O}(n)$ time, leading to a linear complexity for each iteration. This, however, depends on the eventual growth of the auxiliary degrees of freedom corresponding to the PMLs. As it will be shown below, for the low-frequency problem, we need to increase the number of PML points as $\mathcal{O}(\log \omega)$, to maintain the same convergence rate, which is normally achieved in $\mathcal{O}(\log \omega)$ iterations. Thus, the overall complexity is linear up to poly-log factors.

Chapter 6

Complexity

In this section we provide an overall complexity analysis of our algorithm for the high-frequency Helmholtz equation (1.1) in terms of ω, and it is summarized in Table 6.1. The overall complexity includes:

- the complexity to compute the Babich's expansion,
- the complexity of learning ray directions by NMLA (shown in Table 6.2), and
- the complexity of the linear solver for the discretized systems from both the standard FEMs (in the low-frequency case), and the ray-FEMs (for high-frequency problem) Helmholtz equations.

Methods	Babich	S-FEM	Learning	Ray-FEM	Iter Ray-FEM	Hybrid
Frequency	$\sqrt{\omega}$ or ω	$\sqrt{\omega}$	$\sqrt{\omega}$ or ω	ω	ω	ω
Complexity	$\mathcal{O}(\omega^d \log \omega)$	$\mathcal{O}(\omega^d \log^3 \omega)$	$\mathcal{O}(\omega^d)$	$\mathcal{O}(\omega^d \log \omega)$	$\mathcal{O}(\omega^d \log^3 \omega)$	$\mathcal{O}(\omega^d \log^3 \omega)$

Table 6.1: Overall computational complexities with respect to ω given that the mesh size scaled as $h = \mathcal{O}(\omega^{-1})$.

According to [75, 101], by using the high-order LxF-WENO schemes to compute the Babich ingredients in Algorithm 5, the computational complexity is $\mathcal{O}(N \log N)$, when those asymptotic ingredients are applied in Algorithm 4 to construct the Babich's expansion with linear complexity $\mathcal{O}(N)$, where $N = \mathcal{O}(\omega^d)$ is the total number of grid points in the uniformly discretized mesh with $h = \mathcal{O}(\omega^{-1})$. Consequently, the overall complexity for computing Babich's expansion is $\mathcal{O}(\omega^d \log \omega)$. Moreover, the complexity of ray learning stage and fast solvers for the linear systems are analyzed thoroughly below.

6.1 Ray learning

As described in section 5.2, Algorithm 7 applies NMLA to computed wave fields with low-frequency $\widetilde{\omega} \sim \sqrt{\omega}$ or high-frequency ω. It first estimates ray directions at vertices on a down-sampled coarse mesh $\mathcal{T}_{h_c}$, and then interpolates the ray directions to the vertices on a fine mesh $\mathcal{T}_h$. We remind the reader the following scalings: $h = \mathcal{O}(\omega^{-1})$, $h_c = \mathcal{O}(\sqrt{h}) = \mathcal{O}(\omega^{-\frac{1}{2}})$. These scalings allow us to strike a balance among the number of observation points at which NMLA is used to estimate ray directions, the radius of the sampling circle, and the corresponding number of sampling points on the circle so as to resolve the wave field to reach the optimal accuracy of NMLA with desired total computational complexity.

The dominant computational cost of the ray learning is coming from the application of NMLA to the high-frequency wave field. Here we analyze its complexity in 2-D case. As shown in section 3.3, the least error that can be achieved by NMLA is $\mathcal{O}(\omega^{-\frac{1}{2}})$ when the radius r of the sampling circle centered at an observation point is $\mathcal{O}(\omega^{-\frac{1}{2}})$. Hence the number of points sampled on the circle to resolve the wave field with frequency ω is $M_\omega = \mathcal{O}(\omega r) = \mathcal{O}(\omega^{\frac{1}{2}})$. Since NMLA is a linear filter based on the Fourier transform in the angle space, the corresponding computational complexity is $\mathcal{O}(M_\omega \log M_\omega)$ [14]. The number of observation points that we need to perform NMLA is the number of vertices on the coarse mesh which is $\mathcal{O}(h_c^{-2}) = \mathcal{O}(\omega)$. Hence the computational cost to obtain the ray directions at the vertices on the coarse mesh by NMLA is $\mathcal{O}(\omega^{\frac{3}{2}} \log \omega)$. Finally, the ray directions estimated at the vertices on the coarse mesh by NMLA are linearly interpolated onto the fine mesh $\mathcal{T}_h$. Interpolation is a linear operation and hence its computational complexity is $\mathcal{O}(\omega^2)$.

Table 6.2 provides the complexity of ray learning stage for both high-frequency and low-frequency wave fields, where d is the dimension and C_{NMLA}, C_{ray,h_c}, C_{Int}, and $C_{ray,h}$ are the computation complexity of NMLA at a single vertex, NMLA on the under-sampled coarse mesh, interpolation of local ray directions to the fine mesh, and the full algorithm for learning local ray directions at frequency ω on the fine mesh $\mathcal{T}_h$, respectively.

Frequency	r	M_ω	C_{NMLA}	C_{ray,h_c}	C_{Int}	$C_{ray,h}$
ω	$\omega^{-\frac{1}{2}}$	$\omega^{\frac{d-1}{2}}$	$\omega^{\frac{d-1}{2}}\log\omega$	$\omega^{d-\frac{1}{2}}\log\omega$	ω^d	ω^d
$\widetilde{\omega}\sim\sqrt{\omega}$	$\widetilde{\omega}^{-\frac{1}{2}}$	$\widetilde{\omega}^{\frac{d-1}{2}}$	$\widetilde{\omega}^{\frac{d-1}{2}}\log\widetilde{\omega}$	$\widetilde{\omega}^{d-\frac{1}{2}}\log\widetilde{\omega}$	ω^d	ω^d

Table 6.2: Computational complexities of estimating ray directions on a coarse mesh $\mathcal{T}_{h_c}$ with $h_c = \mathcal{O}(\omega^{-\frac{1}{2}})$ and a fine mesh $\mathcal{T}_h$ with $h = \mathcal{O}(\omega^{-1})$.

6.2 Helmholtz Solver

The most computationally intensive component in the whole ray-FEM algorithm is solving the linear systems after discretization of the Helmholtz equation. Algorithm 9 and 10 solve both $\mathbf{u}_{\widetilde{\omega},h} = \textit{S-FEM}(\widetilde{\omega}, h, c, f, g)$ and $\mathbf{u}_{\mathbf{d}_\omega,h} = \textit{Ray-FEM}(\omega, h, c, f, g, \{\boldsymbol{d}^j_{\omega,h}\}_{j=1}^{N_h})$ on the same mesh $\mathcal{T}_h$. Each solver is composed of three steps: the assembling step, the setup step, and the iterative solve step.

Since the basis functions are locally supported, the resulting matrix is sparse. The complexity of the assembling step is of the same order as the degrees of freedom $N_h = \mathcal{O}(\omega^d)$.

In the setup stage, the computational domain is decomposed into subdomains of thin layers whose width is comparable to the characteristic wavelength. The local problems in each subdomain are factorized[1] using a multifrontal method [29] coupled with a nested dissection ordering [48] in $\mathcal{O}(\sqrt{N_h})$ time for the high-frequency problem (or $\mathcal{O}(\sqrt{N_h}\log^3 N_h)$ time for the low-frequency problem, depending on the width of the auxiliary PML for each subdomain in terms of the wavelength). Given that the layers are $\mathcal{O}(1)$ elements thick, we have to factorize $\mathcal{O}(\sqrt{N_h})$ subsystems, which results in a total $\mathcal{O}(N_h)$ (or $\mathcal{O}(N_h \log^3 N_h)$ for the low frequency problem) asymptotic complexity for the setup step.

Finally, for the iterative solve step, each application of the preconditioner involves 6 local solves per layer, each one performed with $\mathcal{O}(\sqrt{N_h})$ (or $\mathcal{O}(\sqrt{N_h}\log^2 N_h)$) complexity. Given that we have $\mathcal{O}(\sqrt{N_h})$ layers, we have an overall $\mathcal{O}(N_h)$ (or $\mathcal{O}(N_h \log N_h)$ for the low frequency problem) complexity per iteration. Extensive numerical experiments suggest that the number of iterations to converge is $\mathcal{O}(\log N_h)$ for both high- and low-frequency solves for smooth media. Hence, the empirical overall complexity is $\mathcal{O}(N_h \log N_h)$ for the high-frequency solve and $\mathcal{O}(N_h \log^3 N_h)$ for the low-frequency one, which as stated before in Table 6.1.

---

[1] The solver was implemented in MATLAB, thus the underlying sparse solver is UMFPACK [28].

Chapter 7

Numerical Experiments

In this chapter we provide several numerical experiments to test the proposed ray-FEM (Algorithm 9 and 10) and corroborate our claims. For all cases, the domain of interest Ω is discretized using a standard triangular mesh with absorbing boundary conditions implemented via IBC (2.1) or PML (4.11) while varying the wave speed profile and the source term. Except for Marmousi model with a rectangular domain $\Omega = (-1.5, 1.5) \times (-0.5, 0.5)$, all other cases have a unit square domain $\Omega = (-0.5, 0.5)^2$. The mesh size h is chosen such that the number of grid points per wavelength (NPW) is fixed, i.e., $\omega h = \mathcal{O}(1)$. Moreover, we fix $\epsilon = \frac{1}{2\pi}$ for frequencies $\omega \geq 100\pi$ so that the L^2 norm of the right-hand side of (4.9) is scaled asymptotically as $\mathcal{O}(\omega^{\frac{1}{2}})$ in this frequency regime (see the explanation at the end of section 4.3.2).

We use a high-order Gaussian quadrature rule [30] [1] to compute the integrals required to assemble the mass and stiffness matrices in (2.11) and (4.13), the right hand side in (2.12) and (4.14), and the relative L^2 errors of the ray-FEM solutions. The algorithms are implemented in MATLAB 2015b based on iFEM package [25] and the numerical experiments are executed

---

[1] Given the expression of the mass and stiffness matrices, which are polynomials times a plane wave, it is possible to compute the integral analytically [96]. However, the right hand side of the linear system and the L^2 error of the ray-FEM solution can only be computed numerically for a general source term $f(\mathbf{x})$.

in a dual socket server with 2 Intel Xeon E5-2670 and 384 GB of RAM.

7.1 Convergence tests

In the first test, the exact solution to the Helmholtz equation with the Robin boundary condition (2.1) is the wave field (normalized by the frequency ω) corresponding to a point source outside the domain. It is given by

$$u_{ex}(x, y) = \sqrt{\omega} H_0^{(1)}(\omega \sqrt{(x-2)^2 + (y-2)^2}). \tag{7.1}$$

Numerically we choose a mesh size to solve the Helmholtz equation (1.1) with wave speed $c(\mathbf{x}) \equiv 1$, source $f(\mathbf{x}) \equiv 0$ and exact impedance boundary data such that the number of points per wave length (NPW) is 6 for different ω's. We test convergence for both the ray direction estimation by NMLA and the final numerical solution by the ray-FEM.

First, a probing wave with low-frequency $\widetilde{\omega} = \sqrt{\omega}$ is solved by the standard FEM. Then NMLA is applied to the low-frequency probing wave to get an estimation of the local dominant ray directions $\mathbf{d}_{\widetilde{\omega}}$. Instead of using the regular NMLA for the plane wave decomposition, we use NMLA with curvature correction (see details in Algorithm 3 and section 3.4) to estimate the ray information of a circular wave front. The estimated local ray directions are then used in the ray-FEM to produce the first numerical solution $u_{\mathbf{d}_{\widetilde{\omega}}}$ to the high-frequency Helmholtz equation.

We employ one more iteration in the framework of the iterative ray-FEMs by applying NMLA to $u_{\mathbf{d}_{\widetilde{\omega}}}$ to get an improved local ray direction estimation $\mathbf{d}_w$ and then use it again in the ray-FEM to get a more accurate numerical solution $u_{\mathbf{d}_w}$ to the high-frequency Helmholtz equation.

Table 7.1 and the left column of Figure 7.1 show that the NMLA and ray-FEM algorithm are stable, and the error for both the ray estimation and the numerical solution by the ray-FEM with fixed NPW, i.e., $\omega h = \mathcal{O}(1)$, asymptotically decreases as the frequency increases. Moreover, they show that one more iteration using the iterative ray-FEM can improve the accuracy of final numerical solution to the order of $\mathcal{O}(\omega^{-1})$, which is of the same order when the exact ray direction $\mathbf{d}_{ex}$ is used in the ray-FEM, due to the asymptotic error of the geometric-optics ansatz.

NMLA with curvature correction plays an important role to achieve the above optimal convergence orders. As discussed in section 3.4, it can improve the angle estimation for a perfect point source solution from $\mathcal{O}(\omega^{-1/2})$ to a much higher convergence order $\mathcal{O}(\omega^{-3})$. However, the noise level coming from low-frequency problem solved by S-FEM, together with the interpolation error, which are all $\mathcal{O}(\omega^{-1})$, dominate the overall error. As a consequence, the low-frequency ray estimation error $\|\mathbf{d}_{\widetilde{w}} - \mathbf{d}_{ex}\|$ is $\mathcal{O}(\omega^{-1})$. Using similar estimate in section 3.5, one can show that the approximation error for the high-frequency numerical ray-FEM space is at least $\mathcal{O}(\omega^{-1})$ if $\mathbf{d}_{\widetilde{w}}$ is incorporated into the high-frequency basis functions. Again we apply NMLA with curvature correction to the numerically computed high frequency ray-FEM solution to get ray estimation $\mathbf{d}_w$ with $\|\mathbf{d}_w - \mathbf{d}_{ex}\| = \mathcal{O}(\omega^{-1})$ and further get the final ray-FEM solution $u_{\mathbf{d}_w}$ with $\|u - u_h\|_{L^2(\Omega)} = \mathcal{O}(\omega^{-1})$.

Next we show that our method can handle multiple wave fronts by probing the whole domain and extracting dominant ray directions locally. The setup is exactly as above except that there are four point sources. The exact solution is given by

$$\begin{aligned} u_{ex}(x,y) \; &= \sqrt{\omega} H_0^{(1)}(\omega\sqrt{(x+20)^2+(y+20)^2}) + 2\sqrt{\omega} H_0^{(1)}(\omega\sqrt{(x-20)^2+(y-20)^2}) \\ &+0.5\sqrt{\omega} H_0^{(1)}(\omega\sqrt{(x+20)^2+(y-20)^2}) - \sqrt{\omega} H_0^{(1)}(\omega\sqrt{(x-20)^2+(y+20)^2}). \end{aligned} \tag{7.2}$$

The main difficulty of this example compared to the single point source case is that the

$\omega/2\pi$	20	40	80	160
$1/h$	120	240	480	960
$\|\theta(\mathbf{d}_{\tilde{\omega}}) - \theta_{ex}\|_{L^2}$	7.50e-04	4.26e-04	1.96e-04	1.07e-04
$\|\theta(\mathbf{d}_{\omega}) - \theta_{ex}\|_{L^2}$	1.82e-04	7.99e-05	4.43e-05	2.10e-05
$\|u_{\mathbf{d}_{\tilde{\omega}}} - u_{ex}\|_{L^2}$	4.36e-05	1.92e-05	9.03e-06	4.69e-06
$\|u_{\mathbf{d}_{\omega}} - u_{ex}\|_{L^2}$	3.15e-05	1.47e-05	7.57e-06	3.73e-06
$\|u_{\mathbf{d}_{ex}} - u_{ex}\|_{L^2}$	2.97e-05	1.49e-05	7.47e-06	3.74e-06

Table 7.1: Errors of one point source problem for fixed NPW $= 6$. θ_{ex} is the exact ray angle, $\theta(\mathbf{d}_{\tilde{\omega}})$ and $\theta(\mathbf{d}_{\omega})$ are ray angle estimations using low and high-frequency waves, respectively; $u_{\mathbf{d}_{\tilde{\omega}}}$, $u_{\mathbf{d}_{\omega}}$ and $u_{\mathbf{d}_{ex}}$ are ray-FEM solutions using low-frequency ray estimation $\mathbf{d}_{\tilde{\omega}}$, high-frequency ray estimation $\mathbf{d}_{\omega}$, and exact ray $\mathbf{d}_{ex}$, respectively.

low-frequency wave solution by the standard FEM contains multiple wave fronts at each point due to the interference of multiple sources. The numerical results are shown in the right column of Figure 7.1. In this case, the NMLA with curvature correction does not apply so that we have to use the the standard NMLA for the plane wave decomposition as described in section 3.1 to estimate local dominant ray directions. As analyzed in section 3.5 and section 3.3, the expected error for ray direction estimation and numerical solution is of order $\mathcal{O}(\omega^{-1/2})$ due to the curved wave fronts. The numerical results show that the ray-FEM meets the expected asymptotic error as the frequency increases.

7.2 Phase errors

Here we show that the ray-FEM method can capture the phase and satisfy the dispersion relation more accurately. We test our algorithm with a point source inside the domain, given its importance in many practical applications, in particular, in exploration geophysics, in which the sources are often modeled as point sources. Moreover, in applications oriented towards inverse and imaging problems, having a numerical method that produces the correct phase in the far field is of great importance in order to properly locate features in the image.

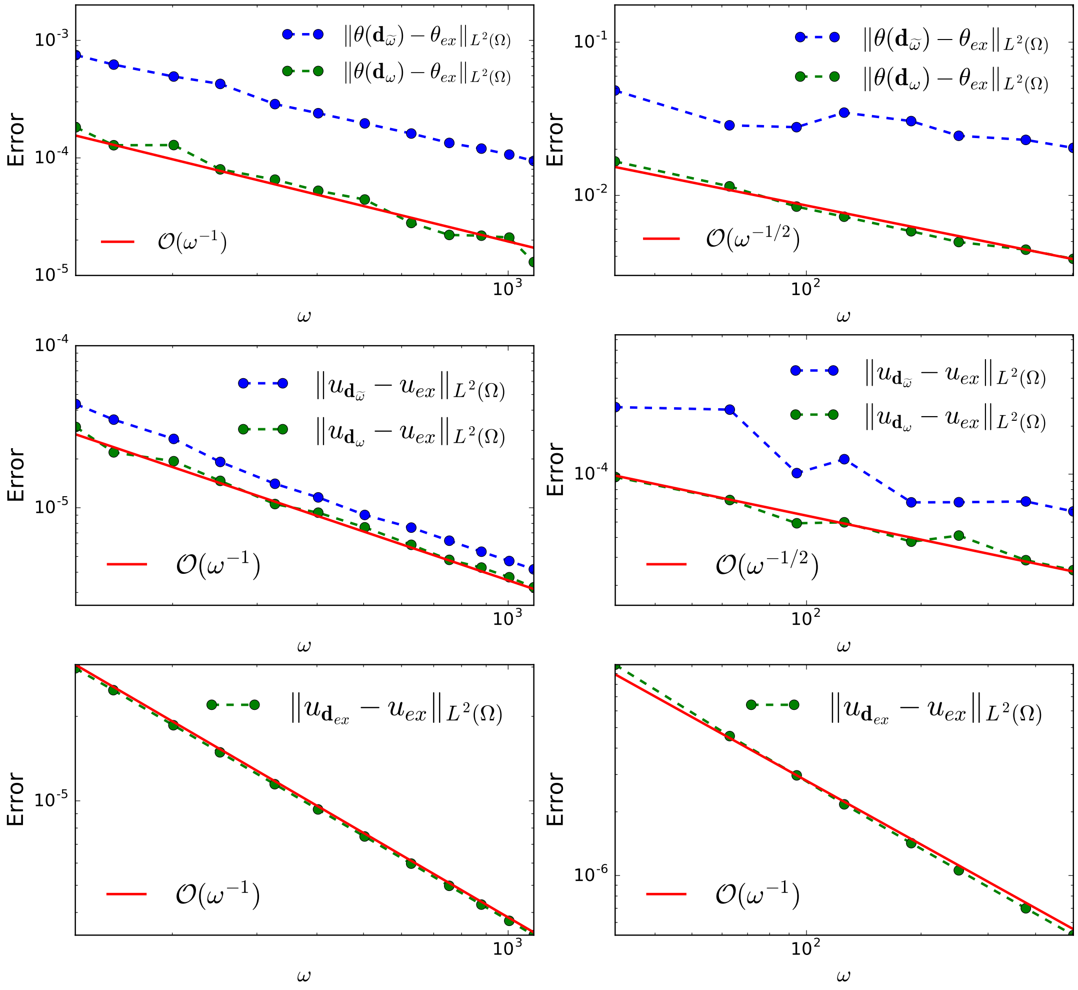

Figure 7.1: Tests with point source/sources outside the domain, NPW = 6. Left: one point source; Right: four point sources. Top: ray direction errors; Middle: errors of ray-FEM solutions with ray directions estimated by NMLA; Bottom: errors of ray-FEM solutions with exact ray directions.

In this experiment we focus our attention on the far-field since the default ray-FEM (Algorithm 9) can not deal with singularities in amplitude and phase at source points. We test a point source located at $\mathbf{x}_0 = (-0.4, -0.4)$ with frequency $\omega = 80\pi$ in a homogeneous medium. Following Remark 5, we use radial directions (exact directions in homogeneous medium) for vertices $\mathbf{x}$ near the source with $|\mathbf{x} - \mathbf{x}_0| \leq 0.1$ and estimate ray directions for other vertices; see the left part of Figure 7.2 for the ray-direction field.

To demonstrate the accurate phase of the numerical solutions, we plot the real part of computed wave field on a 90 degree part of an annulus [111], with the radial coordinate varying on an interval of about two wavelengths. The location where the real part is maximal or minimal, according to the exact solution, is indicated by a straight line; see the right part of Figure 7.2.

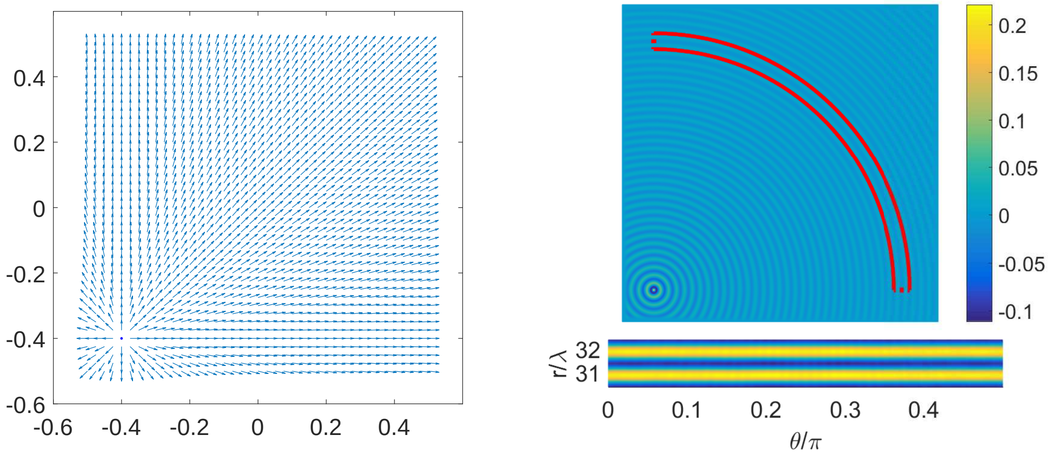

Figure 7.2: One point source inside a homogeneous medium, $\omega = 80\pi$, NPW $= 6$. Left: ray directions captured by NMLA; Right: polar plot of the ray-FEM solution, r/λ: the number of wavelengths away from the source.

Next we fix the frequency $\omega = 250\pi$ and use radial directions as ray directions in the source neighborhood $\{\mathbf{x} : |\mathbf{x} - \mathbf{x}_0| \leq 0.064\}$. When the number of grid points per wavelength is increased, Figure 7.3 depicts the behavior of both the ray-FEM solution and the standard FEM solution. From the figure we can easily observe the superiority of the ray-FEM on minimizing the phase error, even using relatively coarse meshes.

In a heterogeneous medium, a ray-FEM solution is given by Figure 7.4 with the source located inside. We also provide an experiment where we show the ability of Algorithm 9 introduced in section 5.3 to handle wave fields with caustics; see Figure 7.5. Again radial directions are used for local ray directions near the source point within $\{\mathbf{x} : |\mathbf{x} - \mathbf{x}_0| \leq 0.1\}$.

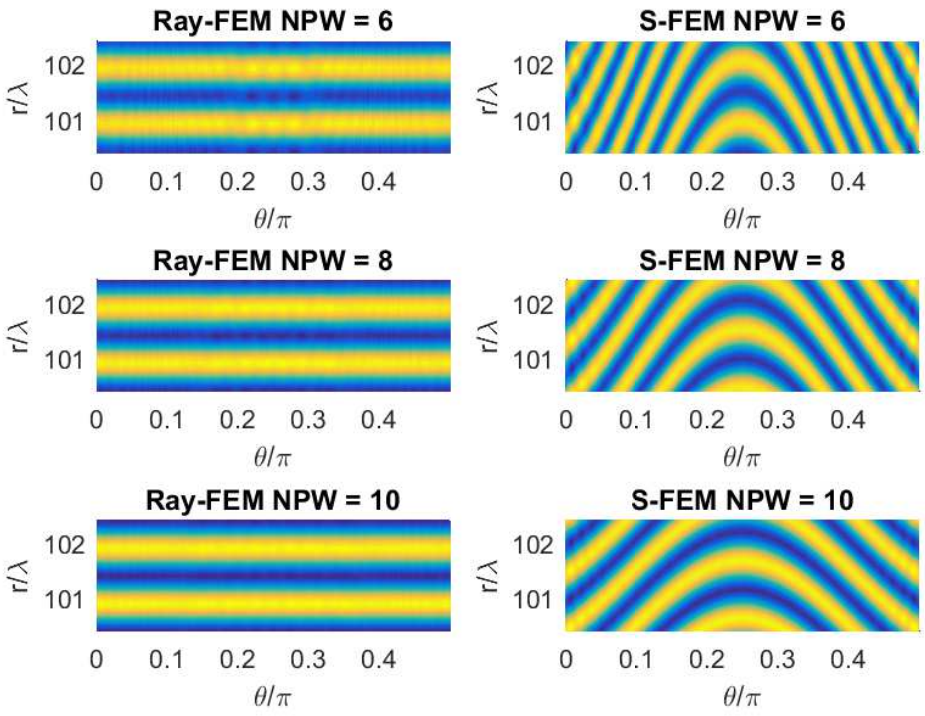

Figure 7.3: Polar plots of the ray-FEM solution and the s-FEM solution with $\omega = 250\pi$. r/λ: the number of wavelengths away from the source.

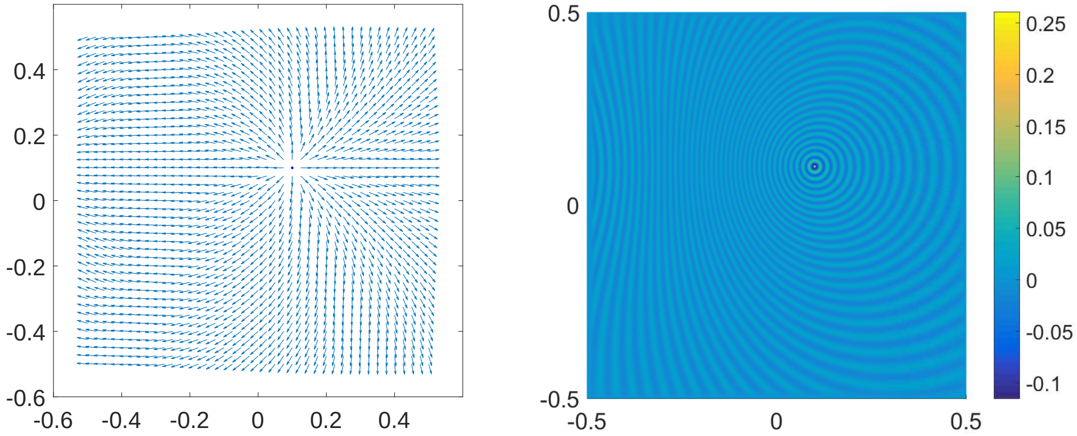

Figure 7.4: One point source inside a heterogeneous medium with the Gaussian wave speed $c(x, y) = 3 - 2.5e^{-((x+0.125)^2+(y-0.1)^2)/0.8^2}$, $\omega = 80\pi$, NPW $= 10$. Left: ray directions captured by NMLA; Right: wave field computed by ray-FEM.

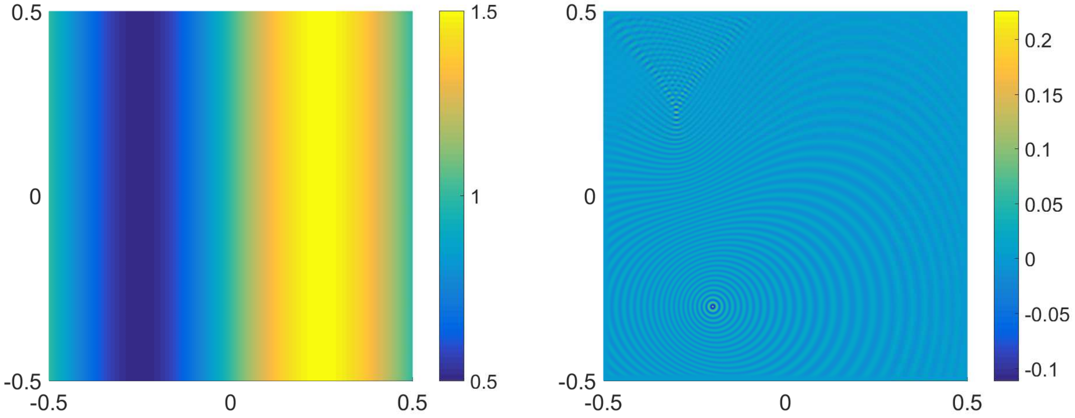

Figure 7.5: One point source inside a heterogeneous medium with the sinusoidal wave speed $c(x, y) = 1 + 0.5 \sin(2\pi x)$, $\omega = 80\pi$, NPW $= 10$. Left: wave speed; Right: wave field computed by ray-FEM.

7.3 Complexity tests

In this section we test the computational complexity for the ray-FEM. A key step of the algorithms presented is solving the sparse linear systems generated by the ray-FEM using iterative methods with a performant preconditioner, e.g., domain decomposition techniques coupled with high-quality absorbing/transmission boundary conditions. In our tests, we use a modification of the method of polarized traces to solve the linear systems resulting from both the standard FEM and ray-FEM as described in section 5.5.

We solve the Helmholtz equation with a point source in both a homogeneous and heterogeneous medium. We compute for many different frequencies, using Algorithm 9 with only one iteration of the ray-FEM, the solution to the Helmholtz equation posed on Ω with absorbing boundary conditions implemented via PML. For each frequency we report the execution time of the low and high-frequency problems and the time spent in processing the data using NMLA to extract the dominant ray information.

As explained in section 5, in order to process the data using NMLA we need to solve the low-frequency problem in a slightly larger domain. The size of the larger domain is given by the sampling radius of the NMLA. For the sake of simplicity, we use a low-frequency subdomain, $\Omega_{low} = (-1,1) \times (-1,1)$, i.e., four times bigger than the original domain. The size can be reduced in order to lower the computational cost for the low-frequency problem.

The main issue with the low-frequency solver in our case is related to the PML, since the PML may not be very effective given that each thin slab contains less than one wavelength across. In order to decrease the number of iterations to converge, we increase the number of PML points logarithmically with the frequency. This implies a slightly more expensive setup cost and solve cost as shown in Figures 7.6 left and 7.7 left.

Figure 7.6 shows the runtime for solving the Helmholtz equation with a point source inside a homogeneous medium. We can observe that the overall cost is $\mathcal{O}(N)$ up to poly-logarithmic factors as shown in our complexity study. The low-frequency solver has a slightly higher asymptotic cost in this case, given the ratio between the width of the PML and the characteristic wavelength inside the domain.

Figure 7.7 shows the runtime for solving the Helmholtz equation with a point source inside a heterogenous medium. We can observe the same scaling as before, albeit with slightly larger constants.

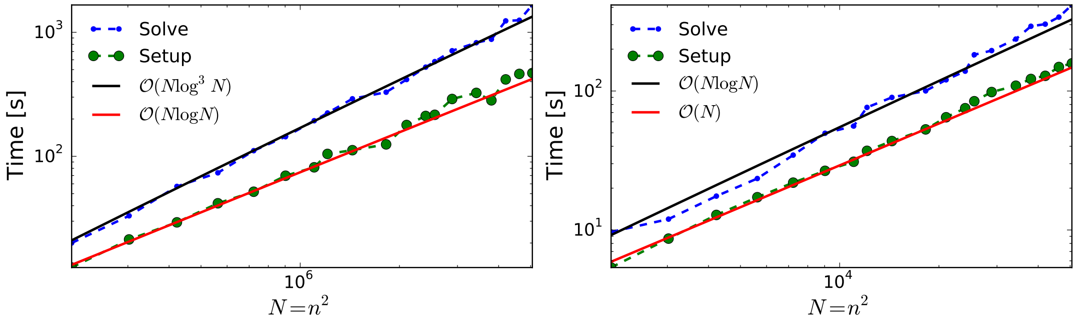

Figure 7.6: Runtime for solving the Helmholtz equation with a homogeneous wave-speed using GMRES preconditioned with the method of polarized traces. The tolerance was set up to 10^{-7}. Left: runtime for solving the low-frequency problem. Right: Runtime for solving the high-frequency problem with the adaptive basis.

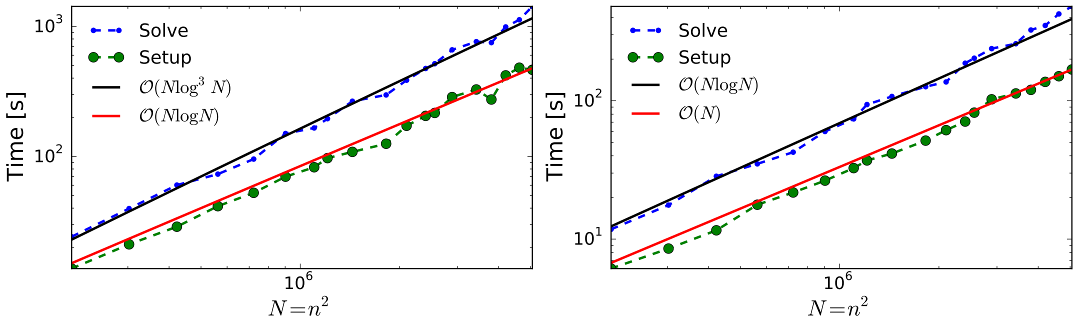

Figure 7.7: Runtime for solving the Helmholtz equation with a heterogeneous wave-speed using GMRES preconditioned with the method of polarized traces. The tolerance was set up to 10^{-7}. Left: runtime for solving the low-frequency problem. Right: runtime for solving the high-frequency problem with the adaptive basis.

7.4 Hybrid Solver

All of the above tests are implemented by applying Algorithm 9 without singularity removal. In this section we test the proposed hybrid approach to validate our convergence and complexity claims.

7.4.1 Homogeneous medium with exact and numerical rays

We compute the numerical solution to the Helmholtz equation (1.1) in a homogeneous medium, $c(\mathbf{x}) \equiv 1$, with the exact solution given by

$$u_{ex}(x, y) = \frac{i}{4} H_0^{(1)}(\omega\sqrt{x^2 + y^2}). \tag{7.3}$$

Convergence

Since the Babich's expansion in a homogeneous medium is exactly the first Hankel function, we use the analytical u_b and ∇u_b to construct the right-hand side of (4.9), and we check the convergence rate for the far field solution u_{far} with both exact and numerically computed (by NMLA) ray directions.

From section 4.3.3, if the ray information is known exactly and $h = \mathcal{O}(\omega^{-1})$, then the relative L^2 error in the ray-FEM approximation space is $\mathcal{O}(\omega^{-1})$. Figure 7.8 left shows that the ray-FEM is stable and it achieves the desired convergence order with fixed NPW.

On the other hand, if the ray information is numerically estimated by NMLA with accuracy order $\mathcal{O}(\omega^{-1/2})$, the optimal approximation error by the ray-FEM is also $\mathcal{O}(\omega^{-1/2})$ [36]. In fact, we use exact radial ray directions in the disk $D_{2\epsilon}$ and numerically learn the ray directions outside this disk. Figure 7.8 right indicates the ray-FEM solution with the learned ray information is of the same order $\mathcal{O}(\omega^{-1/2})$.

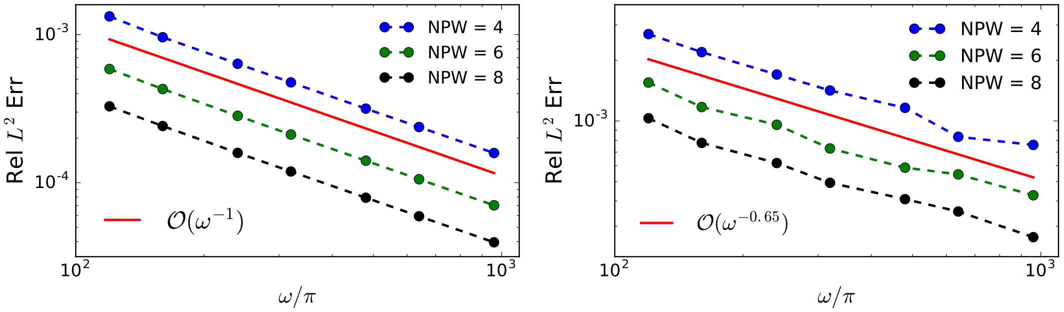

Figure 7.8: Relative L^2 error of smooth part solution to equation (4.9) for one point-source problem in homogeneous medium, NPW is fixed. Left: exact rays. Right: numerical rays estimated by NMLA.

Complexity

We use the fast solver introduced in section 5.5 to solve (4.9) thus obtaining the far field component of the wave field. From Figure 7.9 we can observe that the results are qualitatively equal to the ones obtained in section 7.3, the complexity is linear up to poly-log factors. We point out that the complexity is higher for the low-frequency case given that we need to increase the number of PML points as $\mathcal{O}(\log^2 \omega)$ in order to obtain a very mild growth in the number of iterations. We remark that for this case the largest number of waves we have computed is around 500 in each direction.

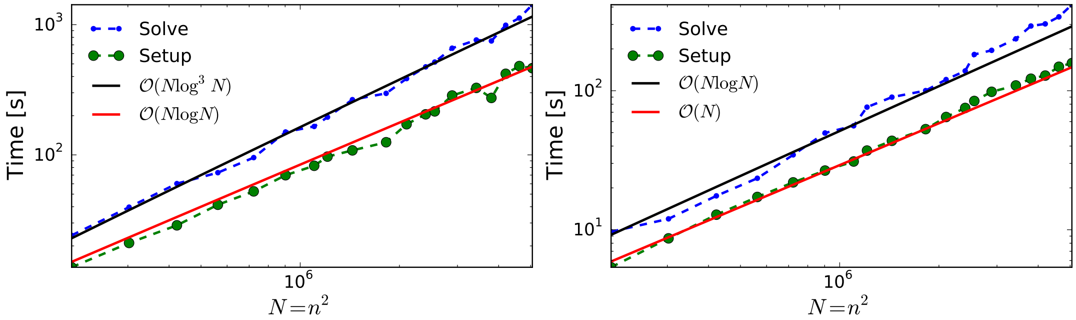

Figure 7.9: Runtime for solving the Helmholtz equation with a homogeneous wave speed using GMRES preconditioned with the method of polarized traces. The tolerance was set up to 10^{-9}. Left: runtime for solving the low-frequency problem. Right: Runtime for solving the high-frequency problem with the adaptive basis.

7.4.2 Lippmann-Schwinger equation

We test our algorithm when the wave speed is constant up to a compactly supported heterogeneity. In this case we compute the reference solution by solving the Lippmann-Schwinger equation discretized using the super-algebraically convergent discretization proposed in [1], which is then solved using the fast solver introduced in [130].

In order to use the Lippmann-Schwinger equation, we suppose that the point-source is located far from the heterogeneity. In particular, we set the point-source to be located at $\mathbf{x}_0 = (-0.2, -0.2)$ and the squared slowness to be

$$m(\mathbf{x}) = 1 + 0.2h(\mathbf{x}, \alpha, \beta)\exp\left(-\frac{r^2(\mathbf{x})}{2\sigma^2}\right), \tag{7.4}$$

where $\alpha = 0.16, \beta = 0.22, \sigma = 0.15$, $\mathbf{x}_1 = (0.2, 0.2)$, $r(\mathbf{x}) = |\mathbf{x} - \mathbf{x}_1|$, $t(\mathbf{x}, \alpha, \beta) = \frac{r(\mathbf{x})-\alpha}{\beta-\alpha}$,

$P(t) = \frac{2e^{-1/t}}{t-1}$ and

$$h(\mathbf{x}) = \begin{cases} 1, & \text{if } r(\mathbf{x}) \leq \alpha, \\ \exp\left(P(t(\mathbf{x}, \alpha, \beta))\right), & \text{if } \alpha < r(\mathbf{x}) < \beta, \\ 0, & \text{if } r(\mathbf{x}) \geq \beta. \end{cases}$$

In this case, in the disk $D_{2\epsilon}$, the medium is homogeneous so that we can build the right-hand side and the rays analytically; outside of this disk, the medium is heterogeneous and we apply NMLA to estimate the ray directions. Besides, we use Algorithm 10 to compute the ray-FEM solution to the far field equation (4.9) and compare it to the reference solution described in [130]. Figure 7.10 shows that the relative error in $L^2(\Omega)$ norm follows the desired convergence rate $\mathcal{O}(\omega^{-1/2})$ with fixed NPW. We mention that for this example the largest number of waves we have computed is around 500 in each direction.

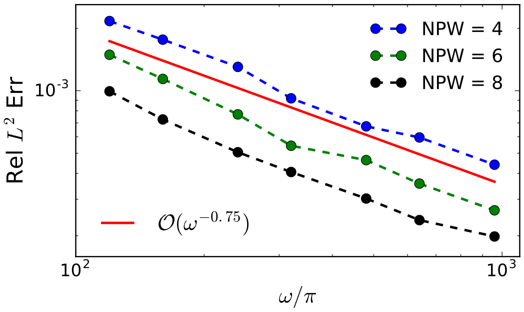

Figure 7.10: Relative L^2 error of smooth part solution to Lippmann-Schwinger equation with squared slowness (7.4), NPW is fixed.

7.4.3 Wave speed of constant gradient

We provide an example in a heterogeneous medium with wave speed of constant gradient: $c(\mathbf{x}) = c_0 + G_0 \cdot (\mathbf{x} - \mathbf{x}_0)$ with parameters $c_0 = 1$, $G_0 = (0.1, -0.2)$ and $\mathbf{x}_0 = (0, 0)$. The phase function is known analytically [43] and there is no ray crossing in the domain $\Omega = (-0.5, 0.5)^2$. Then Algorithm 4 can produce an accurate solution to (1.1) in the whole domain and we treat this solution as the reference solution.

We construct the right-hand side with numerically computed u_b and ∇u_b in the disk $D_{2\epsilon}$ and then apply Algorithm 10 to compute the numerical solution to (1.1). We compute the relative L^2 error with respect to the reference solution. Figure 7.11 left shows that the error scales as $\mathcal{O}(\omega^{-1})$ when we use analytical rays outside the disk $D_{2\epsilon}$; on the other hand, Figure 7.11 right shows that the error scales as $\mathcal{O}(\omega^{-1/2})$ when we use numerically computed rays by NMLA instead.

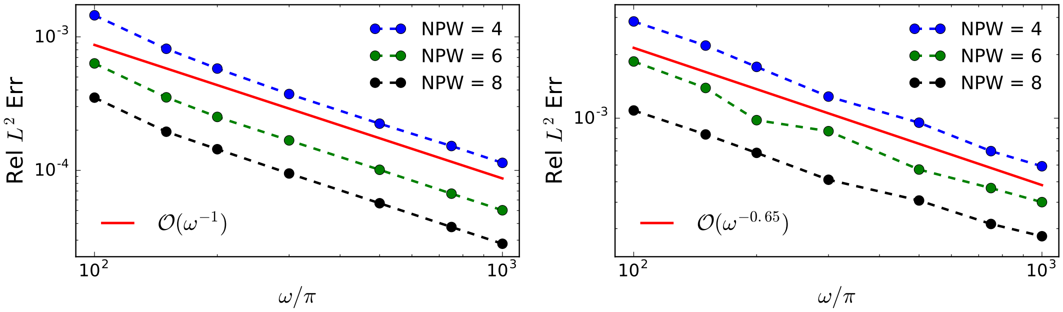

Figure 7.11: Relative L^2 error of numerical solution to Helmholtz equation (1.1) with constant gradient of velocity, NPW is fixed. Left: analytical rays. Right: numerical rays estimated by NMLA.

7.4.4 Marmousi model

Finally, we apply our method to the Marmousi2 model [83]. Figure 7.12 shows the wavespeed, which is smoothed by a convolution with a Gaussian kernel with standard deviation of 100 meters. In this model, we re-scale the computational domain to $\Omega = (-1.5, 1.5) \times (-0.5, 0.5)$ and we locate the point source such that the wave speed is constant in the neighborhood $D_{2\epsilon}$. Within this neighborhood, caustics do not occur so that the Babich's expansion is reduced to the Hankel function, which can compute the wave field and ray directions very accurately. However, in the far field $\Omega \backslash D_{2\epsilon}$, where ray crossing happens and caustics occur, we utilize NMLA to capture only the local dominant ray directions. We select at most four significant ray directions by sorting amplitudes. In addition, we select rays that are well separated with an angle difference at least 15 degrees.

Then we use Algorithm 10 to compute the wave field at 18.75 [Hz] on the mesh with 4 grid points for the smallest wavelength (NPW = 4). The real part of the wave field is shown in Figure 7.13. Furthermore, we regard the solution on the mesh with NPW = 16 as the reference solution u_{ref} and compute numerical solutions u_h on different coarser meshes to show the h convergence rate in Table 7.2. A higher frequency case at 75 [Hz] is shown in Figure 7.14. At the highest frequency the solution has roughly 250 wavelengths in the vertical direction and 750 in the horizontal direction.

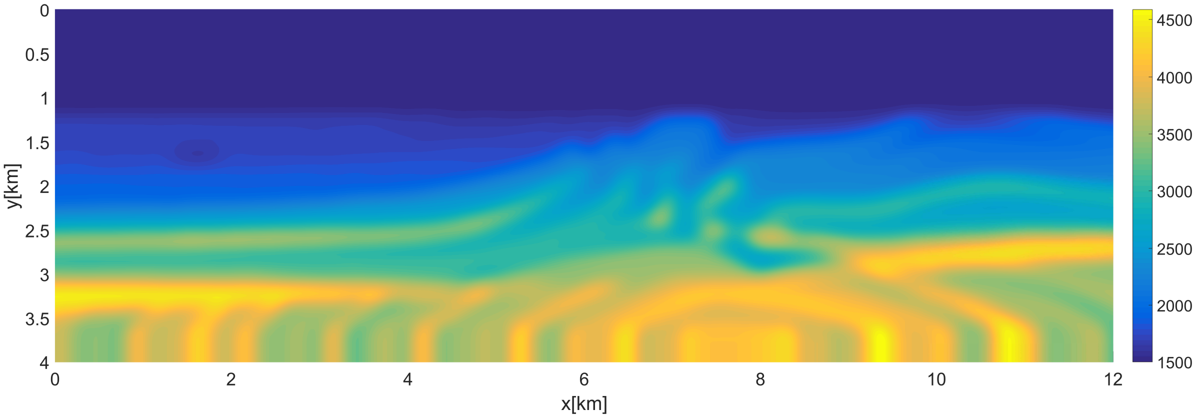

Figure 7.12: Smoothed Marmousi wave speed model.

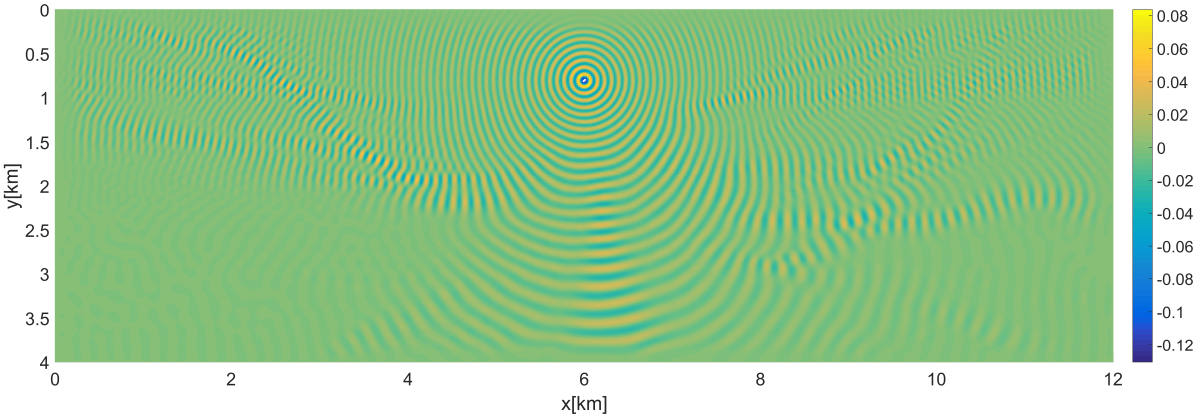

Figure 7.13: Real part of wave field generated by a point-source at 18.75 [Hz] with NPW = 4 for the smoothed Marmousi model.

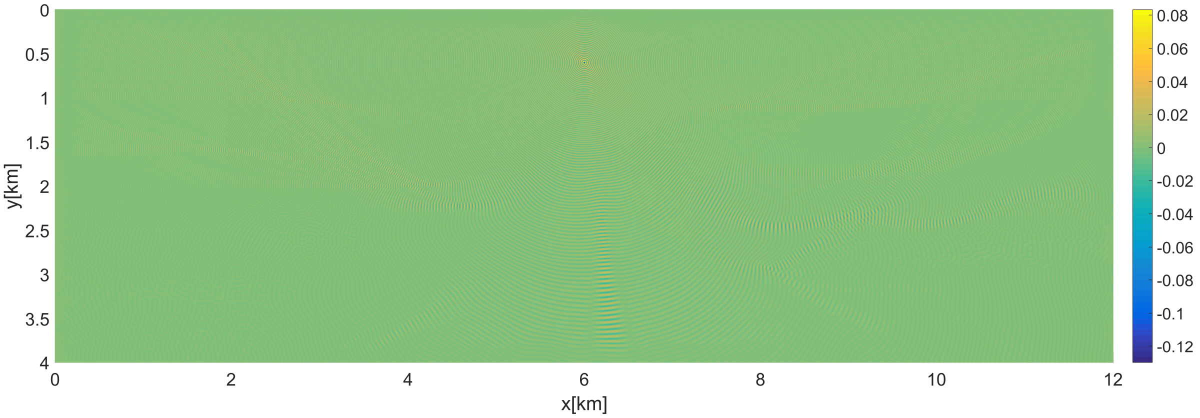

Figure 7.14: Real part of wave field generated by a point-source at 75 [Hz] with NPW = 4 for the smoothed Marmousi model.

NPW	1	2	4	8
$\frac{\|u_h - u_{ref}\|_{L^2(\Omega)}}{\|u_{ref}\|_{L^2(\Omega)}}$	0.9645	0.2846	0.0806	0.0218
Order		1.76	1.82	1.89

Table 7.2: Marmousi model h convergence rate.

Bibliography

[1] S. Ambikasaran, C. Borges, L.-M. Imbert-Gerard, and L. Greengard. Fast, adaptive, high-order accurate discretization of the Lippmann–Schwinger equation in two dimensions. *SIAM Journal on Scientific Computing*, 38(3):A1770–A1787, 2016.

[2] G. S. Avila and J. B. Keller. The high-frequency asymptotic field of a point source in an inhomogeneous medium. *Commun. Pure Appl. Math.*, 16:363–381, 1963.

[3] V. M. Babich. The short wave asymptotic form of the solution for the problem of a point source in an inhomogeneous medium. *USSR Computational Mathematics and Mathematical Physics*, 5(5):247–251, 1965.

[4] V. M. Babich. The short wave asymptotic form of the solution for the problem of a point source in an inhomogeneous medium. *USSR Computational Mathematics and Mathematical Physics*, 5(5):247–251, 1965.

[5] I. Babuska and B. Guo. The h, p and h-p version of the finite element method; basis theory and applications. *Advances in Engineering Software*, 15(3):159 – 174, 1992.

[6] I. Babuska, F. Ihlenburg, E. T. Paik, and S. A. Sauter. A generalized finite element method for solving the Helmholtz equation in two dimensions with minimal pollution. *Computer Methods in Applied Mechanics and Engineering*, 128(3-4):325–359, 1995.

[7] I. Babuska and J. M. Melenk. The partition of unity method. *International Journal for Numerical Methods in Engineering*, 40(4):727–758, 1997.

[8] I. M. Babuska and S. A. Sauter. Is the pollution effect of the FEM avoidable for the Helmholtz equation considering high wave numbers? *SIAM Review*, 42(3):451–484, 2000.

[9] A. H. Barnett and T. Betcke. Stability and convergence of the method of fundamental solutions for Helmholtz problems on analytic domains. *Journal of Computational Physics*, 227(14):7003 – 7026, 2008.

[10] A. H. Barnett and T. Betcke. An exponentially convergent nonpolynomial finite element method for time-harmonic scattering from polygons. *SIAM Journal on Scientific Computing*, 32(3):1417–1441, 2010.

[11] J.-D. Benamou. An introduction to Eulerian Geometrical Optics (1992-2002). *J. Sci. Comput.*, 19(1-3):63–93, 2003.

[12] J.-D. Benamou, F. Collino, and S. Marmorat. Numerical microlocal analysis of 2-D noisy harmonic plane and circular waves. *Research Report, INRIA*, 2011.

[13] J.-D. Benamou, F. Collino, and S. Marmorat. Numerical microlocal analysis revisited. *Research Report, INRIA*, 2011.

[14] J.-D. Benamou, F. Collino, and O. Runborg. Numerical microlocal analysis of harmonic wavefields. *J. Comp. Phys.*, 199:714–741, 2004.

[15] J.-P. Bérenger. A perfectly matched layer for the absorption of electromagnetic waves. *Journal of Computational Physics*, 114(2):185–200, 1994.

[16] T. Betcke and J. Phillips. Approximation by dominant wave directions in plane wave methods. Technical report, 2012.

[17] N. Bleistein. *Mathematical methods for wave phenomena.* Academic Press, 2012.

[18] J. Brokesova. *Asymptotic ray method in seismology: A tutorial.* Publication No.168, Matfyzpress, 2012.

[19] D. L. Brown, D. Gallistl, and D. Peterseim. Multiscale Petrov-Galerkin method for high-frequency heterogeneous Helmholtz equations. *arXiv preprint arXiv:1511.09244*, 2015.

[20] A. Buffa and P. Monk. Error estimates for the ultra weak variational formulation of the Helmholtz equation. *ESAIM: Mathematical Modelling and Numerical Analysis*, 42(6):925–940, 2008.

[21] R. Carriere and R. L. Moses. High resolution radar target modeling using a modified Prony estimator. *IEEE Transactions on Antennas and Propagation*, 40(1):13–18, Jan 1992.

[22] O. Cessenat and B. Després. Application of an ultra weak variational formulation of elliptic PDEs to the two-dimensional Helmholtz problem. *SIAM Journal on Numerical Analysis*, 35(1):255–299, 1998.

[23] O. Cessenat and B. Després. Using plane waves as base functions for solving time harmonic equations with the ultra weak variational formulation. *Journal of Computational Acoustics*, 11(02):227–238, 2003.

[24] C. Chapman. *Fundamentals of seismic wave propagation.* Cambridge university press, 2004.

[25] L. Chen. iFEM: an innovative finite element methods package in MATLAB. *Preprint, University of Maryland*, 2008.

[26] Z. Chen, D. Cheng, and T. Wu. A dispersion minimizing finite difference scheme and preconditioned solver for the 3D Helmholtz equation. *Journal of Computational Physics*, 231(24):8152–8175, 2012.

[27] D. Colton and R. Kress. *Inverse acoustic and electromagnetic scattering theory*, volume 93. Springer Science & Business Media, 2012.

[28] T. A. Davis. Algorithm 832: UMFPACK v4.3—an unsymmetric-pattern multifrontal method. *ACM Transactions on Mathematical Software*, 30(2):196–199, June 2004.

[29] I. S. Duff and J. K. Reid. The multifrontal solution of indefinite sparse symmetric linear. *ACM Trans. Math. Softw.*, 9(3):302–325, Sept. 1983.

[30] D. Dunavant. High degree efficient symmetrical Gaussian quadrature rules for the triangle. *International journal for numerical methods in engineering*, 21(6):1129–1148, 1985.

[31] B. Engquist and O. Runborg. Computational high frequency wave propagation. *Acta Numerica*, 12:181–266, May 2003.

[32] B. Engquist and L. Ying. Sweeping preconditioner for the Helmholtz equation: hierarchical matrix representation. *Communications on Pure and Applied Mathematics*, 64(5):697–735, 2011.

[33] B. Engquist and L. Ying. Sweeping preconditioner for the Helmholtz equation: moving perfectly matched layers. *Multiscale Modeling & Simulation*, 9(2):686–710, 2011.

[34] B. Engquist and H. Zhao. Approximate separability of Green's function for high frequency Helmholtz equations, March 2014.

[35] J. Fang, J. Qian, L. Zepeda-Núñez, and H. Zhao. A hybrid approach to solve the high-frequency Helmholtz equation with source singularity. *Submitted to Journal of Computational Physics*, 2017.

[36] J. Fang, J. Qian, L. Zepeda-Núñez, and H. Zhao. Learning dominant wave directions for plane wave methods for high-frequency Helmholtz equations. *Research in the Mathematical Sciences*, 4(9), May 2017.

[37] C. Farhat, I. Harari, and L. P. Franca. The discontinuous enrichment method. *Computer Methods in Applied Mechanics and Engineering*, 190(48):6455–6479, 2001.

[38] C. Farhat, I. Harari, and U. Hetmaniuk. A discontinuous Galerkin method with Lagrange multipliers for the solution of Helmholtz problems in the mid-frequency regime. *Computer Methods in Applied Mechanics and Engineering*, 192(11–12):1389 – 1419, 2003.

[39] C. Farhat, R. Tezaur, and P. Weidemann-Goiran. Higher-order extensions of a discontinuous Galerkin method for mid-frequency Helmholtz problems. *International Journal for Numerical Methods in Engineering*, 61(11):1938–1956, 2004.

[40] C. Farhat, P. Wiedemann-Goiran, and R. Tezaur. A discontinuous Galerkin method with plane waves and Lagrange multipliers for the solution of short wave exterior Helmholtz problems on unstructured meshes. *Wave Motion*, 39(4):307–317, 2004.

[41] X. Feng and H. Wu. Discontinuous Galerkin methods for the Helmholtz equation with large wave number. *SIAM Journal on Numerical Analysis*, 47(4):2872–2896, 2009.

[42] D. T. Fernandes and A. F. D. Loula. Quasi optimal finite difference method for Helmholtz problem on unstructured grids. *International Journal for Numerical Methods in Engineering*, 82(10):1244–1281, 2010.

[43] S. Fomel, S. Luo, and H. K. Zhao. Fast sweeping method for the factored eikonal equation. *J. Comput. Phys.*, 228:6440–6455, 2009.

[44] G. Gabard. Discontinuous Galerkin methods with plane waves for time-harmonic problems. *Journal of Computational Physics*, 225(2):1961–1984, 2007.

[45] G. Gabard, P. Gamallo, and T. Huttunen. A comparison of wave-based discontinuous Galerkin, ultra-weak and least-square methods for wave problems. *International Journal for Numerical Methods in Engineering*, 85(3):380–402, 2011.

[46] D. Gallistl and D. Peterseim. Stable multiscale Petrov–Galerkin finite element method for high frequency acoustic scattering. *Computer Methods in Applied Mechanics and Engineering*, 295:1–17, 2015.

[47] P. Gamallo and R. Astley. A comparison of two Trefftz-type methods: the ultraweak variational formulation and the least-squares method, for solving shortwave 2-D Helmholtz problems. *International journal for numerical methods in engineering*, 71(4):406–432, 2007.

[48] A. George. Nested dissection of a regular finite element mesh. *SIAM Journal on Numerical Analysis*, 10:345–363, 1973.

[49] E. Giladi and K. J. B. A hybrid numerical asymptotic method for scattering problems. *Journal of Computational Physics*, 174(1):226–247, 2001.

[50] C. J. Gittelson, R. Hiptmair, and I. Perugia. Plane wave discontinuous Galerkin methods: Analysis of the h-version. *ESAIM: Mathematical Modelling and Numerical Analysis*, 43:297–331, 3 2009.

[51] C. I. Goldstein. The weak element method applied to Helmholtz type equations. *Applied Numerical Mathematics*, 2(3):409 – 426, 1986.

[52] D. Gottlieb and S. Orszag. *Numerical Analysis of Spectral Methods.* Society for Industrial and Applied Mathematics, 1977.

[53] I. Harari and E. Turkel. Accurate finite difference methods for time-harmonic wave propagation. *Journal of Computational Physics*, 119(2):252 – 270, 1995.

[54] R. Hiptmair, A. Moiola, and I. Perugia. Plane wave discontinuous Galerkin methods for the 2D Helmholtz equation: Analysis of the p-version. *SIAM Journal on Numerical Analysis*, 49(1):264–284, 2011.

[55] R. Hiptmair, A. Moiola, and I. Perugia. A survey of Trefftz methods for the Helmholtz equation. *ArXiv e-prints*, 2015.

[56] L. Hörmander. Fourier integral operators I. *Acta Math.*, 127:79–183, 1971.

[57] C. Howarth. *New generation finite element methods for forward seismic modelling.* PhD thesis, University of Reading, 2014.

[58] Y. Hua and T. K. Sarkar. Matrix pencil method for estimating parameters of exponentially damped/undamped sinusoids in noise. *IEEE Transactions on Acoustics, Speech, and Signal Processing*, 38(5):814–824, May 1990.

[59] T. Huttunen, P. Gamallo, and R. J. Astley. Comparison of two wave element methods for the Helmholtz problem. *Communications in Numerical Methods in Engineering*, 25(1):35–52, 2009.

[60] F. Ihlenburg. *Finite Element Analysis of Acoustic Scattering.* Springer-Verlag New York, 1998.

[61] F. Ihlenburg and I. Babuska. Finite element solution of the helmholtz equation with high wave number part II: the *hp* version of the FEM. *SIAM Journal on Numerical Analysis*, 34(1):315–358, 1997.

[62] L.-M. Imbert-Gérard. Interpolation properties of generalized plane waves. *Numerische Mathematik*, pages 1–29, 2015.

[63] L.-M. Imbert-Gérard and B. Després. A generalized plane-wave numerical method for smooth nonconstant coefficients. *IMA Journal of Numerical Analysis*, 34(3):1072–1103, 2014.

[64] L.-M. Imbert-Gerard and P. Monk. Numerical simulation of wave propagation in inhomogeneous media using generalized plane waves. *ArXiv e-prints*, 2015.

[65] H. Jeffreys. On certain approximate solutions of linear differential equations of the second order. *Proceedings of the London Mathematical Society*, s2-23(1):428–436, 1925.

[66] U. Jentschura and E. Lötstedt. Numerical calculation of Bessel, Hankel and Airy functions. *Computer Physics Communications*, 183(3):506–519, 2012.

[67] C.-H. Jo, C. Shin, and J. H. Suh. An optimal 9-point, finite-difference, frequency-space, 2-D scalar wave extrapolator. *Geophysics*, 61(2):529–537, 1996.

[68] C. Y. Kao, S. J. Osher, and J. Qian. Lax-Friedrichs sweeping schemes for static Hamilton-Jacobi equations. *J. Comput. Phys.*, 196:367–391, 2004.

[69] J. Keller and R. Lewis. Asymptotic methods for partial differential equations: the reduced wave equation and Maxwell's equations. *Surv. in Appl. Math.*, 1:1–82, 1995.

[70] S. Kim, C.-S. Shin, and J. B. Keller. High-frequency asymptotics for the numerical solution of the Helmholtz equation. *Applied Mathematics Letters*, 18(7):797 – 804, 2005.

[71] M. Kline and I. W. Kay. *Electromagnetic Theory and Geometrical Optics.* Interscience, New York, 1965.

[72] P. Lax. Asymptotic solutions of oscillatory initial value problems. *Duke Math. J.*, 24:627–645, 1957.

[73] R. LeVeque. *Finite Difference Methods for Ordinary and Partial Differential Equations.* Society for Industrial and Applied Mathematics, 2007.

[74] A. Lieu, G. Gabard, and H. Bériot. A comparison of high-order polynomial and wave-based methods for Helmholtz problems. *Journal of Computational Physics*, 321:105–125, Sept. 2016.

[75] W. Lu, J. Qian, and R. Burridge. Babich's expansion and the fast Huygens sweeping method for the Helmholtz wave equation at high frequencies. *J. Comput. Phys.*, 313:478–510, 2016.

[76] S. Luo and J. Qian. Factored singularities and high-order Lax-Friedrichs sweeping schemes for point-source traveltimes and amplitudes. *J. Comput. Phys.*, 230:4742–4755, 2011.

[77] S. Luo, J. Qian, and R. Burridge. Fast Huygens sweeping methods for Helmholtz equations in inhomogeneous media in the high frequency regime. *J. Comput. Phys.*, 270:378–401, 2014.

[78] S. Luo, J. Qian, and R. Burridge. High-order factorization based high-order fast sweeping methods for point-source eikonal equations. *SIAM J. Numer. Analy.*, 52:23–44, 2014.

[79] S. Luo, J. Qian, and R. Burridge. High-order factorization based high-order hybrid fast sweeping methods for point-source eikonal equations. *SIAM J. Numer. Analy.*, 52:23–44, 2014.

[80] S. Luo, J. Qian, and H.-K. Zhao. Higher-order schemes for 3-D traveltimes and amplitudes. *Geophysics*, 77:T47–T56, 2012.

[81] T. Luostari, T. Huttunen, and P. Monk. The ultra weak variational formulation using Bessel basis functions. *Communications in Computational Physics*, 11(2):400, 2012.

[82] T. Luostari, T. Huttunen, and P. Monk. Improvements for the ultra weak variational formulation. *International Journal for Numerical Methods in Engineering*, 94(6):598–624, 2013.

[83] G. Martin, R. Wiley, and K. Marfurt. An elastic upgrade for Marmousi. *The Leading Edge, Society for Exploration Geophysics*, 25, 2006.

[84] P. Mayer and J. Mandel. *The finite ray element method for the Helmholtz equation of scattering: first numerical experiments.* University of Colorado at Denver, Center for Computational Mathematics, 1997.

[85] J. Melenk and S. Sauter. Convergence analysis for finite element discretizations of the Helmholtz equation with Dirichlet-to-Neumann boundary conditions. *Mathematics of Computation*, 79(272):1871–1914, 2010.

[86] J. M. Melenk. *On Generalized Finite Element Methods.* PhD thesis, University of Maryland, 1995.

[87] J. M. Melenk, A. Parsania, and S. Sauter. General DG-methods for highly indefinite Helmholtz problems. *J Sci Comput*, 57(3):536–581, 2013.

[88] J. M. Melenk and S. Sauter. Wavenumber explicit convergence analysis for Galerkin discretizations of the Helmholtz equation. *SIAM Journal on Numerical Analysis*, 49(3):1210–1243, 2011.

[89] A. Moiola, R. Hiptmair, and I. Perugia. Plane wave approximation of homogeneous Helmholtz solutions. *Zeitschrift für angewandte Mathematik und Physik*, 62(5):809–837, 2011.

[90] A. Moiola and E. Spence. Is the Helmholtz equation really sign-indefinite? *SIAM Review*, 56(2):274–312, 2014.

[91] P. Monk and D.-Q. Wang. A least-squares method for the Helmholtz equation. *Computer Methods in Applied Mechanics and Engineering*, 175(1–2):121–136, 1999.

[92] J. W. Nehrbass, J. O. Jevtic, and R. Lee. Reducing the phase error for finite-difference methods without increasing the order. *IEEE Transactions on Antennas and Propagation*, 46(8):1194–1201, Aug 1998.

[93] N. C. Nguyen, J. Peraire, F. Reitich, and B. Cockburn. A phase-based hybridizable discontinuous Galerkin method for the numerical solution of the Helmholtz equation. *J. Comput. Physics*, 290:318–335, 2015.

[94] S. Olver and A. Townsend. A fast and well-conditioned spectral method. *SIAM Review*, 55(3):462–489, 2013.

[95] S. Operto, J. Virieux, P. Amestoy, J.-Y. L'Excellent, L. Giraud, and H. B. H. Ali. 3D finite-difference frequency-domain modeling of visco-acoustic wave propagation using a massively parallel direct solver: A feasibility study. *Geophysics*, 72(5):SM195–SM211, 2007.

[96] I. Perugia, P. Pietra, and A. Russo. A plane wave virtual element method for the Helmholtz problem. *ESAIM: Mathematical Modelling and Numerical Analysis*, 50(3):783–808, 2016.

[97] D. Peterseim. Eliminating the pollution effect in Helmholtz problems by local subscale correction. *Math. Comp.*, 2016. Also available as INS Preprint No. 1411.

[98] S. Petersen, D. Dreyer, and O. von Estorff. Assessment of finite and spectral element shape functions for efficient iterative simulations of interior acoustics. *Computer Methods in Applied Mechanics and Engineering*, 195(44–47):6463 – 6478, 2006.

[99] V. F. Pisarenko. The retrieval of harmonics from a covariance function. *Geophysical Journal International*, 33(3):347–366, 1973.

[100] J. Qian, S. Luo, and R. Burridge. Fast Huygens sweeping methods for multi-arrival Green's functions of Helmholtz equations in the high frequency regime. *Geophysics*, 80:T91–T100, 2015.

[101] J. Qian, S. Luo, and R. Burridge. Fast Huygens' sweeping methods for multiarrival Green's functions of Helmholtz equations in the high-frequency regime. *Geophysics*, 80(2):T91–T100, 2015.

[102] J. Qian and W. W. Symes. An adaptive finite difference method for traveltime and amplitude. *Geophysics*, 67:167–176, 2002.

[103] J. Qian, L. Yuan, Y. Liu, S. Luo, and R. Burridge. Babich's expansion and high-order Eulerian asymptotics for point-source Helmholtz equations. *J. Sci. Comput.*, 67(3):883–908, June 2016.

[104] J. Qian, L. Yuan, Y. Liu, S. Luo, and R. Burridge. Babich's expansion and high-order eulerian asymptotics for point-source Helmholtz equations. *Journal of Scientific Computing*, 67:883–908, 2016.

[105] L. Rayleigh. On the propagation of waves through a stratified medium, with special reference to the question of reflection. *Proceedings of the Royal Society of London Series A*, 86:207–226, Feb. 1912.

[106] Y. Saad and M. H. Schultz. GMRES: A generalized minimal residual algorithm for solving nonsymmetric linear systems. *SIAM J. Sci. Stat. Comput.*, 7(3):856–869, July 1986.

[107] R. Schmidt. Multiple emitter location and signal parameter estimation. *IEEE Transactions on Antennas and Propagation*, 34(3):276–280, Mar 1986.

[108] C. E. Shannon. Communication in the presence of noise. *Proceedings of the IEEE*, 86(2):447–457, Feb 1998.

[109] C. C. Stolk. A rapidly converging domain decomposition method for the Helmholtz equation. *Journal of Computational Physics*, 241(0):240–252, 2013.

[110] C. C. Stolk. An improved sweeping domain decomposition preconditioner for the Helmholtz equation. *ArXiv e-prints*, 2015.

[111] C. C. Stolk. A dispersion minimizing scheme for the 3-D Helmholtz equation based on ray theory. *Journal of Computational Physics*, 314:618–646, 2016.

[112] C. C. Stolk, M. Ahmed, and S. K. Bhowmik. A multigrid method for the Helmholtz equation with optimized coarse grid corrections. *SIAM Journal on Scientific Computing*, 36(6):A2819–A2841, 2014.

[113] E. Süli. *Finite element methods for partial differential equations.* Oxford University Computing Laboratory, 2002.

[114] M. Taus, L. Demanet, and L. Zepeda-Núñez. A short note on a fast and high-order hybridizable discontinuous Galerkin solver for the 2D high-frequency Helmholtz equation. In *SEG Technical Program Expanded Abstracts 2016*, pages 3835–3840, 2016.

[115] R. Tezaur and C. Farhat. Three-dimensional discontinuous Galerkin elements with plane waves and Lagrange multipliers for the solution of mid-frequency Helmholtz problems. *International journal for numerical methods in engineering*, 66(5):796–815, 2006.

[116] L. L. Thompson. A review of finite-element methods for time-harmonic acoustics. *The Journal of the Acoustical Society of America*, 119(3), 2006.

[117] L. L. Thompson and P. M. Pinsky. A Galerkin least-squares finite element method for the two-dimensional Helmholtz equation. *International Journal for Numerical Methods in Engineering*, 38(3):371–397, 1995.

[118] A. Townsend and S. Olver. The automatic solution of partial differential equations using a global spectral method. *Journal of Computational Physics*, 299:106 – 123, 2015.

[119] L. Trefethen. *Spectral Methods in MATLAB*. Society for Industrial and Applied Mathematics, 2000.

[120] E. Turkel, D. Gordon, R. Gordon, and S. Tsynkov. Compact 2D and 3D sixth order schemes for the Helmholtz equation with variable wave number. *Journal of Computational Physics*, 232(1):272 – 287, 2013.

[121] J. E. Vidale and H. Houston. Rapid calculation of seismic amplitudes. *Geophysics*, 55:1504–1507, 1990.

[122] V. Vinje, E. Iversen, and H. Gjoystdal. Traveltime and amplitude estimation using wavefront construction. *Geophysics*, 58(8):1157–1166, 1993.

[123] A. Vion and C. Geuzaine. Double sweep preconditioner for optimized Schwarz methods applied to the Helmholtz problem. *Journal of Computational Physics*, 266(0):171–190, 2014.

[124] G. N. Watson. *A treatise on the theory of Bessel functions*. Cambridge university press, 1995.

[125] B. S. White. The stochastic caustic. *SIAM J. Appl. Math.*, 44:127–149, 1984.

[126] H. Wu. Pre-asymptotic error analysis of CIP-FEM and FEM for the Helmholtz equation with high wave number. part I: linear version. *IMA Journal of Numerical Analysis*, 34:1266–1288, 2014.

[127] T. Xiong, M. Zhang, Y. T. Zhang, and C.-W. Shu. Fast sweeping fifth order weno scheme for static hamilton-jacobi equations with accurate boundary treatment. *J. Sci. Comput.*, 45:514–536, 2010.

[128] L. Zepeda-Núñez. *Fast and scalable solvers for the Helmholtz equation.* PhD thesis, Massachusetts Institute of Technology, Cambridge MA, USA, 2015.

[129] L. Zepeda-Núñez and L. Demanet. The method of polarized traces for the 2D Helmholtz equation. *Journal of Computational Physics*, 308:347–388, 2016.

[130] L. Zepeda-Núñez and H. Zhao. Fast alternating bidirectional preconditioner for the 2D high-frequency Lippmann–Schwinger equation. *SIAM Journal on Scientific Computing*, 38(5):B866–B888, 2016.

[131] Y. T. Zhang, H. K. Zhao, and J. Qian. High order fast sweeping methods for static Hamilton-Jacobi equations. *J. Sci. Comp.*, 29:25–56, 2006.

[132] L. Zhu and H. Wu. Pre-asymptotic error analysis of CIP-FEM and FEM for Helmholtz equation with high wave number. part II: *hp* version. *SIAM Journal of Numerical Analysis*, 51:1828–1852, 2013.